



UNIVERSIDADE ESTADUAL DE CAMPINAS

Faculdade de Engenharia Elétrica e de Computação

Seyed Saman Mahjour

**Linewidth and phase noise characterization of few kHz laser using self-homodyne  
reception**

**Caracterização de largura de linha e ruído de fase de lasers de poucos kHz usando  
recepção auto-homódina**

Campinas  
2023

Seyed Saman Mahjour

**Linewidth and Phase Noise Characterization of Few kHz Lasers Using Self-Homodyne Reception**

**Caracterização de largura de linha e ruído de fase de lasers de poucos kHz usando recepção auto-homódina**

Thesis presented to the School of Electrical and Computer Engineering of the University of Campinas in partial fulfillment of the requirements for the degree of Doctor in Electrical Engineering, in the area of Telecommunications and Telematics.

Tese apresentada à Faculdade de Engenharia Elétrica e de Computação da Universidade Estadual de Campinas como parte dos requisitos exigidos para a obtenção do título de Doutor em Engenharia Elétrica, na área de Telecomunicações e Telemática.

Advisor: Prof. Dr. Evandro Conforti

This copy corresponds to the final version of the thesis defended by Seyed Saman Mahjour and supervised by Prof. Dr. Evandro Conforti.

Campinas  
2023

Ficha catalográfica  
Universidade Estadual de Campinas  
Biblioteca da Área de Engenharia e Arquitetura  
Rose Meire da Silva - CRB 8/5974

M279L Mahjour, Seyed Saman, 1982-  
Linewidth and phase noise characterization of few kHz laser using self-homodyne reception / Seyed Saman Mahjour. – Campinas, SP : [s.n.], 2023.

Orientador: Evandro Conforti.

Tese (doutorado) – Universidade Estadual de Campinas, Faculdade de Engenharia Elétrica e de Computação.

1. Análise espectral. 2. Parâmetro espectral. 3. Espectro de frequência. 4. Interferômetro de Mach-Zehnder. 5. Comunicações ópticas. I. Conforti, Evandro, 1947-. II. Universidade Estadual de Campinas. Faculdade de Engenharia Elétrica e de Computação. III. Título.

Informações Complementares

**Título em outro idioma:** Caracterização da largura de linha e ruído de fase da lasers de poucos kHz usado recepção auto-homódina

**Palavras-chave em inglês:**

Spectral analysis

Spectral parameter

Frequency spectrum

Mach-Zehnder Interferometer

Optical communications

**Área de concentração:** Energia Elétrica

**Titulação:** Doutor em Engenharia Elétrica

**Banca examinadora:**

Evandro Conforti [Orientador]

Arismar Cerqueira Sodré Junior

Cristiano de Mello Gallep

Tiago Sutili

Ernesto Martin Mari

**Data de defesa:** 14-04-2023

**Programa de Pós-Graduação:** Engenharia Elétrica

**Identificação e informações acadêmicas do(a) aluno(a)**

- ORCID do autor: <https://orcid.org/0000-0002-6161-0182>

- Currículo Lattes do autor: <http://lattes.cnpq.br/2024223589213539>

## COMISSÃO JULGADORA – TESE DE DOUTORADO

Candidato: Seyed Saman Mahjour RA: 229996

Data da defesa: 14 de Abril de 2023

Título da Tese: “Caracterização de largura de linha e ruído de fase de lasers de poucos kHz usando recepção auto-homódina”

Prof. Dr. Evandro Conforti (Presidente)

Prof. Dr. Arismar Cerqueira Sodré Junior

Prof. Dr. Cristiano de Mello Gallep

Prof. Dr. Tiago Sutili

Prof. Dr. Ernesto Martin Mari Barrientos

A Ata de Defesa, com as respectivas assinaturas dos membros da Comissão Julgadora, encontra-se no SIGA (Sistema de Fluxo de Dissertação/Tese) e na Secretaria de Pós-Graduação da Faculdade de Engenharia Elétrica e de Computação.

## Acknowledgements

I should indeed express my very profound gratitude to my parents my mother and father and my brothers Sina and Kourosh for providing me with unwavering support and continuous encouragement throughout my years of study. This accomplishment would not have been possible without them.

I am extremely grateful to my supervisor, Prof. Dr. Evandro Conforti for his invaluable advice, continuous support, and patience during my PhD study. His immense knowledge and plentiful experience have encouraged me in all the time of my academic research and daily life. He inspired me to tackle the challenges on my own, but he always presents for advice and assistance when I need it. Working under Prof. Evandro Conforti's supervision has been a great experience and I have learned and grown a lot.

I would like to express my gratitude and appreciation for Prof. Dr Cristiano de Mello Gallep for his technical support and invaluable feedback that greatly influenced my dissertation and publications. I am grateful for our friendly chats at the end of our meetings and his personal support in my academic endeavors.

I would like to say a special thank you to my colleague Mareli for all of her assistance. She has been incredibly helpful and has kindly offered invaluable help from the moment I started my doctorate program. Every time I was struggling with a concept or feeling lost in the technical aspects of my studies, Mareli provided explanation and guidance.

I would like to thank all the professors Fabiano Fruett, Aldário Chrestani Bordonalli, Yuzo Iano and Darli Augusto de Arruda Mello for the incredible knowledge and guidance they provided me with during my studies.

I'd also like to thank all of my colleagues and friends in the lab, Leonid, Alexander, and Danierik, who have shared their expertise and insights with me over the years and who have made it possible for me to push the boundaries of my field.

O presente trabalho foi realizado com apoio do CNPq, Conselho Nacional de Desenvolvimento Científico e Tecnológico – Brasil.

Finally, many thanks to Brazil for giving me the opportunity to access such valuable resources and for fostering an environment in which innovative research can be conducted.

## **Abstract**

An optical fiber unbalanced Mach-Zehnder interferometer (MZI) with a delayed self-homodyne reception is used to characterize kHz linewidth lasers. Experimental results of noise curves of power spectral density (PSD) reaching a high spectral resolution, from mHz up to 100 kHz. The low frequency noise (LFN) spectrum and linewidth of two distinct lasers including external cavity lasers (ECLs) and integrated external cavity lasers (IECLs) were investigated for various fiber reel delay lengths subjected to environment sound and thermal influences. Ability of photodiodes to convert laser noise to radio frequency noise is examined and the low frequency  $1/f$  and flicker noises are characterized for laser powers up to 10 dBm. Moreover, the high frequency excess noise (in relation to the ideal Lorentzian linewidth) is analyzed for lower than 10 kHz linewidth lasers such as IECLs. The results made it possible to estimate the laser linewidth and obtain an extensive understanding of how coherence events behave.

In summary, a novel noise characterization procedure for highly coherent kHz linewidth lasers is given. Furthermore, the sampling data and estimating the linewidth of lasers used to evaluate reliability and stabilization of the laser diode (LD) are presented.

**Key words:** Laser linewidth, Low-frequency phase noise, Mach-Zehnder interferometer, Optical communications, Power spectral density.

## **Resumo**

Um interferômetro Mach-Zehnder não balanceado de fibra óptica (MZI) com uma recepção auto-homódina atrasada é usado para caracterizar lasers de largura de linha kHz. Resultados experimentais de curvas de ruído de densidade espectral de potência (PSD) atingindo uma alta resolução espectral, de mHz até 100 kHz. O espectro de ruído de baixa frequência (LFN) e a largura de linha de dois lasers distintos, incluindo lasers de cavidade externa (ECLs) e lasers de cavidade externa integrados (IECLs), foram investigados para vários comprimentos de atraso de carretel de fibra sujeitos a influências térmicas e sonoras do ambiente. A capacidade dos fotodiodos de converter o ruído do laser em ruído de radiofrequência é examinada e os ruídos de oscilação e  $1/f$  de baixa frequência são caracterizados para potências de laser de até 10 dBm. Além disso, o excesso de ruído de alta frequência (em relação à largura de linha Lorentziana ideal) é analisado para lasers com largura de linha menor que 10 kHz, como IECLs. Os resultados possibilitaram estimar a largura de linha do laser e obter um amplo entendimento de como os eventos de coerência se comportam.

Em resumo, é apresentado um novo procedimento de caracterização de ruído para lasers de largura de linha kHz altamente coerentes. Além disso, são apresentados os dados de amostragem e estimativa da largura de linha dos lasers usados para avaliar a confiabilidade e estabilização do diodo laser (LD).

**Palavras-chave:** Largura de linha do laser, Ruído de fase de baixa frequência, Interferômetro de Mach-Zehnder, Comunicações ópticas, Densidade espectral de potência.

## List of figures

Figure 2-1 The rate equations Diagram for a semiconductor laser. Adapted from [23] .....	20
Figure 2-2 Amplitude and phase noise: $V_0$ is in volts, $\alpha(t)$ is non-dimensional, $\phi(t)$ is in radians, and $x(t)$ is in seconds. Adapted from [31]. .....	29
Figure 2-3 Power distribution of a real signal source Adapted from [31].....	30
Figure 2-4 The relations between phase noise or fluctuations $\phi(t)$ , frequency fluctuation $\omega(t)$ , fractional-frequency fluctuation $y(t)$ and the phase-time fluctuation $x(t)$ . .....	34
Figure 2-5 Numerical resolution of the optical carrier power spectrum emitted by a semiconductor laser for two output optical signal powers. The phenomenon of spectral broadening due to distortions in its phase is perceived (adapted from [21]). .....	38
Figure 2-6 Line width as a function of the experimentally characterized optical output power for three lasers with different heterojunction architectures. Two designed with multiple quantum wells (with 400 $\mu\text{m}$ and 800 $\mu\text{m}$ cavities) and one bulk (with 400 $\mu\text{m}$ cavity) (adapted from [21]). .....	40
Figure 2-7 An inhomogeneously broadened atomic transition, with individual atomic responses, or "spectral packet". Adapted from [27]......	44
Figure 2-8 An atom traveling across an electromagnetic wave experiences a Doppler shift. Adapted from [27]. .....	46
Figure 2-9 Lineshapes with the same half-power linewidth and total area are compared between gaussian and Lorentzian. Adapted from [27]. .....	47
Figure 2-10 Gaussian and Voigt features with the same half-power values were compared to the carbon monoxide absorption profile (circles) through measurement. Adapted from [27].....	48
Figure 3-1 A typical power spectral density .....	50
Figure 3-2 The Michelson interferometer, including the point source $S$ , the lenses $L1$ and $L2$ , moveable mirrors $M1$ , fixed mirror $M$ , beam splitter $BS$ , compensator $C$ , and detector $D$ . $h$ is the mirror displacement of $M1$ . Adapted from [44]......	52
Figure 3-3 bright fringe in the coherent regime (interferogram pattern). Adapted from [44]......	52
Figure 3-4 Intensity incident on the detector $D$ versus normalized mirror displacement $h/\lambda$ , where $\lambda$ is the mean wavelength. The envelope of the fringe pattern is drawn dotted. Adapted from [44]. .....	52
Figure 3-5 Schematic diagram of the interferometer: Laser (semiconductor); $A1$ and $A2$ directional couplers; $\tau a$ the delay linewidth fiber optic coil; $FD$ photodetector. ....	56
Figure 3-6 Experimental setup shows the interferometer in vacuum chamber. Adapted from [9]. .....	59
Figure 3-7 The optical beat note principle. Adapted from [20] .....	61
Figure 3-8 Typical experimental set-up for linewidth measurement using self-homodyne method. ....	62
Figure 3-9 Experimental curves in $\text{mV}/\text{Hz}$ (left image) and $\text{dBV}/\text{Hz}$ (right image). .....	66
Figure 3-10 Details about the discrete integration process. And Experimental curves $\text{dBV}/\sqrt{\text{Hz}}$ (right image)......	68
Figure 4-1 Self-Homodyne linewidth measurement setup, shows the optical power at each point. ....	69

Figure 4-2 The different effects of polarization control adjustment on the PSD results in terms of the obtaining beat signals. <b>a)</b> The worst adjustment: The polarization of the signals in two arms are almost perpendicular to each other therefore they cancel out each other. <b>b)</b> The worst result: a minimum power is obtained in the PSD and there is a big surge (point G) in the curve. <b>c)</b> Bad adjustment: Beat frequency signals are poorly obtained since the polarization control is not adjusted properly. <b>d)</b> Bad result: Because the polarization control has not been appropriately tuned, the noise power spectrum density is poor and it does not contain the maximum power, however the X point decreases dramatically. <b>e)</b> Without adjustment: the beat signal is not Sharpley observable due to no PC adjustment. <b>f)</b> There are many oscillations in the spectrum. <b>g)</b> The best adjustment: the beating signal is sharply obtained since the PC is well adjusted. <b>h)</b> The best result: noise power spectrum density is obtained as a result of proper OPC adjustment.....	71
Figure 4-3 The PSD result from some other experiment that reveals the peak G. (Adapted from [6])	72
Figure 4-4 <b>a)</b> The PSD in relation to laser power for the RIO1 laser with a fiber length of 55 km. It demonstrates that the G point resonance increases as the laser power decreases and gives some details on excess noise at high frequencies for different emission powers. <b>b)</b> shows that excess noise at high frequencies tends to be greater at lower powers.....	73
Figure 4-5 It compares laser powers of 8 dBm and -8 dBm (RIO 1) and illustrates that the lower the laser power, the bigger the Gaussian noise. It can be seen that X-point resonance increases as laser power decreases.....	74
Figure 4-6 PSD comparison for various fiber lengths and 10 dBm laser power (RIO1 laser).....	74
Figure 4-7 Example of curve adjustment, RIO1 setup with 30km of fiber and 10dBm power.....	76
Figure 4-8 Example of curve adjustment, RIO2 setup with 30km of fiber and 5dBm power.....	76
Figure 4-9 Example of curve adjustment, RIO1 setup with 45km of fiber and 0dBm power.....	76
Figure 4-10 Example of curve fitting, RIO2 setup with 45km of fiber and -10dBm power.....	76
Figure 4-11 The Laser linewidth (Hz) according to optical power (dBm), for RIO 1 .....	78
Figure 4-12 The Laser linewidth (Hz) according to optical power (dBm), for RIO 2 .....	78
Figure 5-1 Frequency fluctuation includes White Noise and Flicker (1/f) Noise. Adapted from [60]	82
Figure 5-2 Schematic diagram of BH (a) and a band diagram (b). Adapted from [68]. .....	84
Figure 5-3 The key functions of the created algorithm.....	88
Figure 5-4 The experimental spectrum highlighting points of interest. ....	91
Figure 5-5 Experimental result evaluating the relationship between the parts of the spectrum.....	91
Figure 5-6 Using the fitting curve for each part of the spectrum. ....	92
Figure 5-7 PSD with three different areas for 55 km fiber length and 10 dBm laser power.....	94
Figure 5-8 PSD with three different areas for 55 km fiber length and 10 dBm laser power.....	94
Figure 5-9 Laser relative excess noise (REN) in terms of power (RIO1). ....	95
Figure 5-10 Laser relative excess noise (REN) in terms of power (RIO2). ....	95
Figure 6-1 Agilent HP 3561A Dynamic Signal Analyzer.....	104

Figure 6-2 RIO PLANEX™ Series 1550nm Low Phase Noise Narrow Linewidth External Cavity Laser.....	104
Figure 6-3 The 7470.EXE software .....	106
Figure 6-4 Five measurements with varying spans were used to construct each graph with its associated output power (10 Hz, 100 Hz, 1 kHz, 10 kHz, 100kHz), The graph below is the overall graph from the above one.....	107

## List of table

Table 3-1 The lasers used in this experiment .....	63
Table 4-1 laser linewidth and the coefficient in terms of power.....	77
Table 5-1 The three main parts of PSD and the quality Q of laser.....	92
Table 6-1 Specifications of Electrical Spectrum Analyzer HP3561A (ESA) .....	103
Table 6-2 key features and applications of RIO PLANEX™ Series .....	104
Table 6-3 Optical and Electrical Specifications of RIO PLANEX™ Series.....	105
Table 6-4 Linewidth and Phase Noise Specifications of RIO PLANEX™ Series .....	105

## Contents

<b>Introduction .....</b>	<b>14</b>
1.1 Motivation.....	15
1.2 Objectives .....	17
1.3 Chapters Description.....	17
<b>2 Theoretical Background.....</b>	<b>19</b>
2.1 Rate equations.....	19
2.1.1 Amplitude rate equations.....	20
2.1.2 Optical carrier phase variations .....	22
2.1.3 Variations in the number of carriers.....	23
2.1.4 Langevin Forces .....	24
2.2 Noise .....	27
2.2.1 Main noise sources .....	28
2.2.2 Basic concept of oscillator.....	28
2.3 Relative Intensity Noise (RIN) .....	30
2.4 Phase noise and linewidth.....	31
2.5 Linewidth Function.....	40
2.5.1 Natural Linewidth with homogeneous broadening .....	41
2.5.2 Natural Linewidth with inhomogeneous broadening .....	43
2.5.3 Definition of spectral packets, strongly inhomogeneous and strongly homogeneous.....	44
2.5.4 Causes of inhomogeneous broadening.....	45
<b>3 Self-Homodyne Detection for Laser Noise Characterization .....</b>	<b>49</b>
3.1 Power spectrum measurement .....	49
3.2 Coherence function .....	51
3.2.1 The Michelson interferometer .....	51
3.3 Self-Homodyne configuration .....	55
3.3.1 Analysis of the Self-Homodyne technique.....	57
3.4 The effect of external factors when using the self-homodyne technique .....	58
3.4.1 Influence of exterior acoustic noise on linewidth laser measurements .....	59
3.5 Measurement Method for Narrow-Linewidth Lasers .....	60
3.6 Experimental methodology for UMZI.....	61

3.6.1	Experimental setup .....	63
3.6.2	Linewidth measurement .....	65
<b>4</b>	<b>Results and discussions.....</b>	<b>69</b>
4.1	The effects of polarization control adjustment, laser power and the optical fiber length on the PSD measurement .....	69
4.1.1	The effect of Optical Polarization Control on PSD data .....	69
4.1.2	The effect of laser power on the laser PSD .....	72
4.1.3	The effect of fiber length on the laser PSD .....	74
4.2	Linewidth measurement by using Lorentzian and Gaussian curve fits .....	75
4.3	Conclusion .....	79
<b>5</b>	<b>kHz Linewidth Laser Characterization using Low Frequency and Excess Noise Measurements .....</b>	<b>81</b>
5.1.1	Origin of 1/f noise.....	82
5.1.2	Model origin of 1/f noise in BH lasers .....	83
5.1.3	Low Frequency Noise (LFN) analysis.....	86
5.2	Methodology .....	87
5.3	Results and discussion .....	89
5.4	Conclusion .....	95
5.5	Future works .....	96
<b>6</b>	<b>References .....</b>	<b>98</b>
<b>7</b>	<b>Appendix .....</b>	<b>103</b>
7.1	Software .....	105
7.2	Designing the graphs with Corel Draw.....	106

## Introduction

---

The semiconductor laser diodes (LDs) meet the stringent demands in optical communication [1]. The LD achievements include long lifetime, compact and small size, convenient integration, and selectable wavelength by electronic command [2, 3]. The LD improvements have been supported by physical modeling including sophisticated numerical analyses [4]. The experimental device advancements include double heterojunction LDs [1], quantum well LDs [2], quantum dot LDs [5], external cavity lasers (ECL) [6], integrated external cavity lasers [6, 7], and below kHz linewidth lasers [6]. Those improvements enhanced the LD output power, decreased the threshold currents [1], achieved high photoelectric conversion efficiency [2], and attained stable wavelength operation [8]. Nowadays, research efforts are focused on the reliability of high-power semiconductor LDs, their lifetime, power enhancement, and energy-efficient lasers. Specifically for optical communications, narrower linewidth, possibly below kHz, are desired in such a way to allow optical phase modulation, reducing the necessity of post detection digital signal processing (DSP) correction circuits, specifically in short distance optical fiber systems (1 km- 2 km) like data center. The integration of various photonic components onto a single chip offers numerous advantages and opens up new possibilities for improving the performance, efficiency, and scalability of lasers and optical transceivers. These developments enhance functionality, enable miniaturization, improve performance, reduce costs, facilitate integration with electronics, and promote technology convergence [6].

Indeed, highly coherent lasers with narrow spectral linewidths are essential for applications such as optical coherent communications [9], linewidth measurement techniques, high precision metrology [10], electro-optical devices characterization [9, 11], vibrometry [4, 12] and high resolution sensing [13, 14]. One of the key factors affecting system performance in these applications is the phase and frequency noises. The characterization and measurement of phase and frequency noises are critical for several applications and they are research topics in the laser and photonics fields [15]. Such lasers' phase and frequency noise can be effectively characterized in terms of linewidth or power spectral density (PSD). The spectral linewidth gives a fundamental and succinct metric for describing the degree of coherence, which is related to the spectral purity or monochromaticity of the laser. This measure allows one to calculate the coherence time of the optical signal [6]. However, it lacks precise information on

frequency noise and its Fourier frequency spectrum, which is required for analyzing noise and optimizing laser performance [15]. As a result, measuring frequency noise PSD is a relevant topic in the area, particularly for lasers with extremely high coherence, whose linewidth is difficult to measure. Lasers with narrow linewidth are highly sensitive, any small external perturbations or noise can cause significant changes in the linewidth measurement, and hence the measurement setup needs to be highly sensitive and carefully designed. Environmental factors such as temperature fluctuations, vibrations, and air currents can affect the stability of the laser and the measurement equipment, leading to inaccuracies in the linewidth measurement [6].

## 1.1 Motivation

The precise characterization of laser linewidth and phase noise is crucial in various fields, including optical communications, metrology, spectroscopy, and sensing. Accurate knowledge of these parameters is essential for achieving high-performance optical systems and improving their overall efficiency. As lasers with a few kilohertz (kHz) linewidth have gained significant interest due to their potential applications in emerging technologies, such as coherent optical communication systems and precision sensing, it becomes imperative to develop effective methods for their characterization.

The conventional techniques used to measure the linewidth and phase noise of lasers often face challenges when dealing with lasers with linewidths in the few kHz range. These techniques typically rely on expensive and complex equipment, making them impractical for widespread use. Furthermore, they may require large measurement setups and involve external references, which can introduce additional uncertainties into the measurements.

In recent years, self-homodyne reception has emerged as a promising alternative for linewidth and phase noise characterization, particularly for lasers operating in the few kHz regime. Self-homodyne reception involves the direct beating of the laser under test with a delayed replica of itself, enabling the measurement of the laser's frequency fluctuations and phase noise with high precision.

The motivation behind this thesis is to explore and develop robust methodologies for linewidth and phase noise characterization of few kHz lasers using self-homodyne reception.

By addressing the limitations of existing techniques and leveraging the advantages of self-homodyne reception, this research aims to provide a comprehensive and practical framework for accurately characterizing the performance of lasers operating at these frequencies.

The outcomes of this thesis will have significant implications for a wide range of applications. In the field of optical communications, the precise characterization of linewidth and phase noise in few kHz lasers will enable the design of more efficient coherent communication systems with enhanced spectral efficiency and increased capacity. Moreover, this research will contribute to advancements in precision sensing, where lasers with narrow linewidths are crucial for achieving high-resolution measurements.

By developing robust methodologies for linewidth and phase noise characterization using self-homodyne reception, this thesis will contribute to the advancement of laser technology and facilitate the adoption of few kHz lasers in various applications. The findings of this research will help bridge the gap between theory and practical implementation, paving the way for improved performance and expanded applications of lasers in the future.

The most common technique to characterize the optical phase and frequency laser noises are Heterodyne Detection (HD) [10], delayed self-heterodyne interferometer (DSH) [16], recirculating delayed self-heterodyne (RDSH) [17], Polarization-Insensitive Recirculating Delayed Self-Heterodyne PI-RDSH [18] and Delayed Self-Homodyne interferometer (DSHI) [6, 19]. These techniques can produce accurate measurements, but their experimental setups are more complex except in the latter case (DSHI). The Heterodyne Detection (HD) requires two laser sources, one of which must be tunable and have a stabilized narrow linewidth as a reference laser source [10, 20]. The RDSH interferometers with a  $2 \times 2$  coupler require active feedback techniques and precise calibration to regulate the quadrature point [15]. The PI-RDSH requires many components and is difficult to set up. So, due to its capacity for large bandwidth analysis and the equipment available for this Thesis, the DSHI was employed here.

The Delayed Self-Homodyne interferometer (DSHI) mounted with unbalanced fiber optic Mach-Zehnder interferometer (UMZI) is simple and easy to build. The UMZI working

in a non-coherent regime was employed. To have both UMZI arms optical signal decorrelation, the relative arms time-delay must be equal to or greater than the laser coherence time ( $\tau_c$ ). The relative delay in UMZI is accomplished here via several fiber optic reels, allowing for adjustable arm length. The delay must be in the order of tens of microseconds for kHz range linewidth; therefore, the length must have hundreds of kilometers of optical fiber. However, we show that the effect of signal correlation is also influenced by thermal and acoustical effects.

Lasers are subject to random fluctuations, which are receiving increasing attention. In this thesis, a comprehensive investigation for a low-frequency optical noise with delayed self-homodyne optical fiber unbalanced Mach-Zehnder interferometer (DSHI) is performed. The achieved results allow a thoughtful insight on the coherence events behavior, in addition to the estimation of lasers linewidth and the reliability and the performance of the laser diode.

## 1.2 Objectives

The thesis main goal is measuring the low frequency noise using an Unbalanced Mach-Zehnder interferometer (UMZI) and analyze their effects on the laser linewidth. The apparent laser linewidth was obtained by analyzing the noise power spectral density (PSD) including comparison with theoretical models. So, the high frequency excess noise (in relation to the ideal Lorentzian linewidth) is analyzed here for lower than 10 kHz linewidth lasers (such as IECLs). The acquired results provide for a full comprehension of coherence event behavior as well as laser linewidth estimate.

## 1.3 Chapters Description

Chapter 2 presents a review of the state of the art. The linewidth in the optical spectrum of the laser oscillator is discussed, including the spectral linewidth with the natural line broadening due to quantum fluctuations, the effects of collisions, and Doppler. Then, the fundamental concepts of noise analysis and effect of output laser power on laser linewidth are discussed.

Chapter 3 presents the analysis of the self-homodyne method using an optical fiber unbalanced Mach-Zehnder interferometer to measure the spectral linewidth of the laser. Models for spectrum measurement are analyzed including the influence of the phase

fluctuations of the laser in non-coherent regimes. The FM-noise spectrum and the linewidth of four distinct lasers including external cavity lasers (ECLs) and integrated external cavity lasers (IECLs) were investigated for various fiber reel delay lengths subjected to environment sound and thermal influences.

In Chapter 4 the effects of polarization control adjustment, laser power and the optical fiber length on the PSD measurement are investigated. The experimental spectrum graphs are shown and a method for approximating the linewidth measurement by using Lorentzian and Gaussian curve fits is presented.

In Chapter 5 the graphs show the different parts of LFN. The three main components of LFN are theoretically and experimentally evaluated, and the non-destructive method is presented to determine the quality of laser for two lasers with different fiber length. The methodology proposed the investigation of phase fluctuations and excess noise in a coherent optical field. By analyzing the phase fluctuation and excess noise of a coherent optical field, it is possible to measure the laser quality with higher accuracy.

## 2 Theoretical Background

---

The objective of this chapter is to provide a comprehensive understanding of the rate equations governing the dynamics of lasers, the mechanisms of phase noise generation, and the relationship between linewidth and frequency noise. By accomplishing these objectives, this chapter will equip readers with a solid understanding of the rate equations governing laser dynamics, the origins of phase noise, and the relationship between linewidth and frequency noise. This knowledge will lay the foundation for further exploration of advanced laser technologies, noise mitigation techniques, and the design of high-performance optical systems in various applications.

### 2.1 Rate equations

The interaction of matter and light in an emitter is described in depth by Maxwell's equations and quantum theory. The rate equations describe and equate the number of electron-hole pairs and the number of photons with the pump energy as well as laser construction and material qualities [21]. Such formulas enable the classical formulation for the amplitude and phase of the laser's signal, as well as fluctuations in its carrier density, which is critical for understanding the spectrum broadening induced by Langevin's forces [21].

Figure 2-1 illustrates the dynamic behavior of the laser diode. An electric current density ( $J$ ) injects charge carriers into the narrow active region. These carriers spontaneously recombine or produce optical gain by stimulated emission. In any semiconductor, electrons and holes can also recombine by non-radiative mechanisms, which include recombination in traps or defects and surface recombination [22], as a consequence there is a photon density in the active region. Part of these photons is emitted by the laser, giving rise to the output power, and another part remains in the cavity and feeds back the stimulated decays [23].

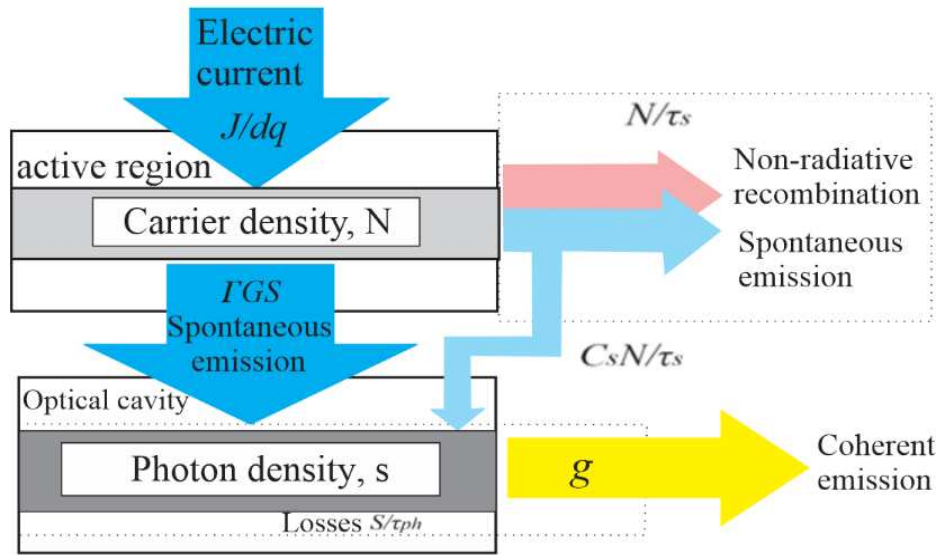


Figure 2-1 The rate equations Diagram for a semiconductor laser. Adapted from [23]

Low threshold current, relatively narrow width, and quick response are just some favored laser properties. The fraction of spontaneous emission that couples into the lasing mode determines the sharpness of the laser threshold current. The longitudinal-mode spectrum is also regulated by the same portion. The line width linked to a single longitudinal mode is caused, in general and especially, by phase noise. [21].

In contrast to the photon life - time and carrier recombination time, the rate equations apply a response of the material driven by inter - band scattering processes with a fast (0.1 ps) transformation. Furthermore, as is common for commercial lasers, the architecture of the laser's semiconductor structure is supposed to have only one propagation mode. As a result, the electromagnetic carrier emitted by the laser,  $E$ , is assumed in equation (2.1) [21].

$$E = Ae^{-j\phi} \quad 2.1$$

Where  $A$  is the optical carrier amplitude and  $\phi$  is the phase of the optical carrier.

### 2.1.1 Amplitude rate equations

The variations in optical carrier amplitude can be calculated using Maxwell's equations, has the advantage of clearly identifying the numerous approximations made throughout its first time derivative,  $\dot{A}$ , as shown in Equation (2.2) [21].

$$\dot{A} = \frac{1}{2} v_g [\Gamma g - (\alpha_{int} + \alpha_m)] A \quad 2.2$$

where  $v_g = c/\mu_g$  is the group velocity,  $\Gamma$  is the confinement factor of the electromagnetic carrier in the active region,  $g$  is the semiconductor optical gain,  $\alpha_{int}$  indicates the attenuation coefficient of the laser's active region, which includes phenomena such as absorption by free carriers and scattering by refraction at the heterojunction interface, whereas  $\alpha_m$  is related to losses on the semiconductor crystal faces [21].

In more detail, the group refractive index,  $\mu_g$ , depends on the fluctuation of refractive index,  $\mu$ , as a function of the different frequencies,  $f$ , which makes up the group of the propagation mode of the optical carrier in the laser cavity, given by Equation (2.3) [21].

$$\mu_g = \mu + f \frac{\partial \mu}{\partial f} \quad 2.3$$

More specifically, the absorption coefficient of the single propagation mode,  $\bar{\alpha}$ , can be expressed by the losses resulting from electromagnetic wave propagation in the active laser region,  $\alpha_{int}$ , and in the semi-mirrors at its ends,  $\alpha_m$ . Given to the confinement factor (filling factor) of the electromagnetic carrier in the active region,  $\Gamma$ , and semiconductor optical gain,  $g$ , this relation is obtained by equation (2.4) [21].

$$\bar{\alpha} = -\Gamma g + \alpha_{int} + \alpha_m \quad 2.4$$

In this expression [21],

$$\alpha_m = \frac{1}{2L} \ln \left( \frac{1}{R_1 R_2} \right) \quad 2.5$$

$L$  is a semiconductor laser of length  $L$ ,  $R_1$  and  $R_2$  are the facet reflectivity at two ends.

and the semiconductor gain,  $g$ , is determined by equation (2.6) [21].

$$g = -\frac{k_0}{\mu_b} \text{Im} (\chi_0 + \chi_p) \quad 2.6$$

where  $k_0 = \omega/c = 2\pi/\lambda$  is the vacuum wave number,  $\mu_b = \sqrt{\epsilon_b}$  is the background refractive index of the unpumped material; Without exterior pumping, medium susceptibility is indicated by  $\chi_0$ , and the additional susceptibility caused by pumping power is indicated by  $\chi_p$ .

Equation 2.2 therefore suggests that the rate of magnitude growth is equal to gains subtracted loss.

The magnitude in equation 2.2 is more easily expressed as a function of the photon number,  $P$ , which is defined by [21].

$$P = \frac{\epsilon_0 \bar{\mu} \mu_g}{2h\omega} \int |\mathcal{E}|^2 dV \quad 2.7$$

where  $\bar{\mu}$  is the refractive index of the propagation mode supported by the laser waveguide,  $h$  is Planck's constant,  $h\omega$  is the photon energy, and  $\epsilon_0$  is the vacuum permittivity. It contains the integration of the modulus of the electric field vector,  $E$ , as a function of the volume of the laser's active region where  $V = Lwd$ , for a laser of length  $L$ , width  $w$ , and thickness  $d$ .

Considering the number of photons proportional to the area of the active region squared ( $P \propto A^2$ ), we have [21].

$$\dot{P} = (G - \gamma)P + R_{sp} \quad 2.8$$

where  $G$  is the total stimulated emission rate of the laser active region, and  $\gamma$  is the photon decay rate in this region.  $R_{sp}$ , indicates the number of photons that are added to the resonant optical signal in the laser cavity, through the spontaneous emission process, which is fundamental for the quantification of the amplitude noise impact on the emitted optical carrier. In more detail [21].

$$G = \Gamma v_g g \quad 2.9$$

And

$$\gamma = v_g(\alpha_{int} + \alpha_m) = \tau_p^{-1} \quad 2.10$$

Where  $\tau_p$  is the photon lifetime in the laser.

The optical strength  $|E|^2$  is only measured using the non - dimensional photon number,  $P$ . It is not meant to imply that photons are particles in any way. This distinction is critical for discussing the intensity noise.

### 2.1.2 Optical carrier phase variations

The phase rate equation that describes the time variations in the phase of the optical carrier,  $\dot{\phi}$ , is given by [21].

$$\dot{\phi} = -\frac{\bar{\mu}}{\mu_g}(\omega - \Omega) - \frac{\omega}{\mu_g}\Gamma\Delta\mu_p \quad 2.11$$

Where  $\omega$  is the lasing-mode frequency (optical carrier frequency) and  $\Omega$  is the resonant frequency of the laser cavity. These quantities are close, but not necessarily the same. This difference is due to the variation in the refractive index of the laser active region which is caused by insertion of new electric carriers into its structure. It is called the carrier-induced index change,  $\Delta\mu_p$ , which is caused by the electrical carrier density,  $\bar{\mu}$  is the effective mode index, and  $\mu_g$  is the group refractive index.

The phase rate equation (2.11) can be written as a function of the stimulated emission rate or gain,  $G$ , and the photon decay rate,  $\gamma$ . To realize is matter, the parameter  $\beta_c$  is used, which is defined as the ratio between the real and imaginary part of the susceptibility  $\chi_p$  (that is,  $\beta_c = Re(\chi_p)/Im(\chi_p)$ ), resulting in the expression presented in (2.12) [21].

$$\Delta\mu_p = -\frac{\beta_c}{2k_0}\Delta g \quad 2.12$$

Using equations (2.9) and (2.12) and replacing  $\Delta G = \Gamma v_g \Delta g$  by  $G - \gamma$ , Eq. (2.11) becomes

$$\dot{\phi} = -(\omega - \omega_{th}) + \frac{1}{2}\beta_c(G - \gamma) \quad 2.13$$

$\omega_{th}$  is the signal's emission's longitudinal-mode frequency that is when the laser operates at its threshold current, and it is equivalent to the mode index's threshold level. Equation (2.13) demonstrates how the phase also shifts when the gain varies out of its threshold value. This occurrence will always cause fluctuations in the semiconductor crystal's index of refraction, denoted by the symbol  $\Delta\mu_p$ , which will alter the longitudinal-mode frequency of the laser, indicated by  $\omega_{th}$ . By expanding  $\Omega(\omega)$  in the vicinity of  $\omega_{th}$ , we can show that  $[\bar{\mu}/\mu_g][\omega - \Omega(\omega)] = \omega - \omega_{th}$  [21].

### 2.1.3 Variations in the number of carriers

In order to obtain the rate equation for the number of electric carriers,  $\dot{N}$ , We must first specify how many carriers are present inside the active material layer. [21] :

$$N = \int n dV = nV \quad 2.14$$

Suppose that  $n$  is almost constant and  $V$  is the active region volume for a laser of length  $L$ , width  $w$ , and thickness  $d$  and given by  $V = Lwd$ .

Considering the laser bias current,  $I$ , is given by  $I = wLJ$  and  $J$  represents the current intensity in the active area then the carrier rate equation,  $\dot{N}$ , is determined by [21]:

$$\dot{N} = \frac{I}{q} - \gamma_e N - GP \quad 2.15$$

$q$  is the electron charge. To put it simply, this expression can be interpreted as the subtraction of the amount of electrons injected in the active region, which is given by the current,  $I$ , divided by the charge of each electron. Also, it has the fraction of carriers that recombine spontaneously, defined by the parameter,  $\gamma_e$ , and by the amount that results in the emission of new photons in a coherent way, given by the multiplication between the rate of stimulated emission by the amount of photons. A non-linear connection seen between the amount of photons and electrons is produced by this final phrase,  $GP$ , in more detail. the intensity of electrical carriers recombining,  $\gamma_e$ , is defined in [21]:

$$\gamma_e = A_{nr} + Bn + Cn^2 = \tau_e^{-1} \quad 2.16$$

It is possible to use the carrier-recombination rate,  $\gamma_e$ , to calculate the spontaneous carrier lifetime  $\tau_e^{-1}$ . Also,  $\gamma_e$ , is produced by both radiative and nonradiative recombination processes. The recombination rate, abbreviated  $A_{nr}$ , is brought on by procedures like surface or trap recombination (due to failures in the semiconductor structure).  $B$  referring to the radiative recombination coefficient (that is, resulting in the emission of photons) and  $C$  to the process of Auger recombination [21].

#### 2.1.4 Langevin Forces

From the rate equations, defined in (2.8), (2.13) and (2.15), random fluctuations arising from the spontaneous emission process (ASE) and the carrier-generation-recombination process are added to these equations, which are referred as Langevin noise sources,  $P$ ,  $N$ , and  $\phi$  become spontaneous in the existence of Langevin noise sources, and the probability rate formulas provided by govern their dynamics. [21]:

$$\dot{P} = (G - \gamma)P + R_{sp} + F_P(t) \quad 2.17$$

$$\dot{\phi} = -(\omega - \omega_{th}) + \frac{1}{2}\beta_c(G - \gamma) + F_\phi(t) \quad 2.18$$

$$\dot{N} = \frac{I}{q} - \gamma_e N - GP + F_N(t) \quad 2.19$$

In practice, the Langevin force, which is associated to changes in the number of electrical carriers,  $F_N(t)$ , is resulting from the discrete nature of the carrier generation and recombination processes (ballistic or shot noise). On the other hand the Langevin forces related to variations in the amount of emitted photons,  $P$ , and in the phase of the optical carrier,  $\phi$ , arise from the spontaneous recombination which are shown by  $F_P(t)$  and  $F_\phi(t)$  respectively [21].

We adopt the Markovian assumption to simplify the analysis of these stochastic rate equations. We assume that the optical lifetimes,  $\tau_p$ , ( and electrical carrier lifetimes,  $\tau_e$ , are much longer than the correlation time between the three Langevin noise sources,  $F_P(t)$ ,  $F_\phi(t)$  and  $F_N(t)$  [21].

According to the Markovian presumption, the Langevin forces fulfill the broader relationships.

$$\langle F_i(t) \rangle = 0 \quad 2.20$$

$$\langle F_i(t)F_j(t') \rangle = 2D_{ij}\delta(t - t') \quad 2.21$$

where  $i$  and  $j$  are variables within the set  $P, \phi, N$ . The parameter  $\delta(t - t')$  is an infinitesimal increment in time and  $D_{ij}$  is the diffusion coefficient associated with the respective Langevin forces, represented by  $i$  and  $j$ , respectively.

The diffusion coefficients  $D_{ij}$  can be determined by calculating the second moments of the dynamic variables using equations (2.17), (2.18) and (2.19). They can also be obtained by physical arguments [24, 25].

By both approaches, such factors will result in equations (2.22) and (2.23) [21]:

$$D_{PP} = R_{sp}P \quad D_{\phi\phi} = R_{sp}/4P \quad D_{P\phi} = 0 \quad 2.22$$

$$D_{NN} = R_{sp}P + \gamma_e N \quad D_{PN} = -R_{sp}P \quad D_{N\phi} = 0 \quad 2.23$$

Where  $N$  is the average value of carrier and photon populations under the steady-state laser condition, respectively.

To evaluate the noise characteristics, the steady-state values of the number of emitted photons,  $P$ , the phase of the emitted wave,  $\phi$ , and the number of electric carriers,  $N$ , are perturbed by small amounts  $\delta P$ ,  $\delta\phi$  and  $\delta N$ , respectively. The stochastic rate equations (2.17), (2.18) and (2.19) are linearized in the analysis of small signals, resulting in [21],

$$\delta\dot{P} = -\Gamma_P\delta P + \left(G_N P + \frac{\partial R_{sp}}{\partial N}\right)\delta N + F_P(t) \quad 2.24$$

$$\delta\dot{N} = -\Gamma_N\delta N - (G + G_P P)\delta P + F_N(t) \quad 2.25$$

$$\delta\dot{\phi} = \frac{1}{2}\beta_c G_N\delta N + F_\phi(t) \quad 2.26$$

Where the fluctuation rates (the small-signal decay rates) in the populations of photons and electrons,  $\Gamma_P$  and  $\Gamma_N$  respectively, are defined by equations (2.27) and (2.28) [5]:

$$\Gamma_P = \frac{R_{sp}}{P} - G_P P \quad 2.27$$

$$\Gamma_N = \gamma_e + N \left(\frac{\partial \gamma_e}{\partial N}\right) + G_N P \quad 2.28$$

On the other hand,  $G_N$  and  $G_P$  are parameters that represent the variations in the rate of stimulated laser emission (gain),  $G$ , as a function of fluctuations in the amounts of electrons and photons in the laser active region, respectively. These parameters are defined by the expressions in (2.29) [21]:

$$G_N = \frac{\partial G}{\partial N} \text{ and } G_P = \frac{\partial G}{\partial P} \quad 2.29$$

It's worth mentioning that the gain derivative,  $G_P$ , includes fluctuations in gain caused by nonlinear processes such as spectral hole burning as one of its contributing factors. However, because the index change associated with such nonlinear processes is assumed to be much smaller than the carrier-induced index change, its contribution to the phase is ignored in equation (2.26) [21].

Finally, to analyze the linear set of  $\delta P$ ,  $\delta\phi$  and  $\delta N$ , in the frequency domain,  $\omega$ , it is possible to apply the Fourier transform to equations (2.24), (2.25) and (2.26) [21],

The following is the definition of the Fourier transform of any function  $f(t)$ : [21],

$$\tilde{f}(\omega) = \int_{-\infty}^{\infty} f(t) \exp(-i\omega t) dt \quad 2.30$$

The results are

$$\delta\tilde{P}(\omega) = \frac{(\Gamma_N + j\omega)\tilde{F}_P + (G_N P + \partial R_{sp}/\partial N)\tilde{F}_N}{(\Omega_R + \omega - j\Gamma_R)(\Omega_R - \omega + j\Gamma_R)} \quad 2.31$$

$$\delta\tilde{N}(\omega) = \frac{(\Gamma_P + j\omega)\tilde{F}_N - (G + G_P P)\tilde{F}_P}{(\Omega_R + \omega - j\Gamma_R)(\Omega_R - \omega + j\Gamma_R)} \quad 2.32$$

$$\delta\tilde{\phi}(\omega) = \frac{1}{j\omega} \left( \tilde{F}_\phi + \frac{1}{2} \beta_c G_N \delta\tilde{N} \right) \quad 2.33$$

where  $\tilde{F}_P$ ,  $\tilde{F}_N$  and  $\tilde{F}_\phi$  are the Fourier transforms of the respective Langevin forces added to the laser rate equations.

The inherent resonance generated by the carrier and photon populations is clearly seen in Equations (2.31) to (2.33) showing the noise enhanced in the vicinity of  $\omega = \Omega_R$ . These equations can show how processes like spontaneous emission and carrier recombination influence the amount of light, the optical phase, and the population of carriers.

## 2.2 Noise

Lasers can produce a variety of noises which can have a wide range of effects on applications. The phrase "laser noise" refers to the random fluctuations of various output parameters [26]. This is a common occurrence that has a significant impact on many applications in photonics, particularly precise measurements. Consider, for example, interferometric position measurements, which can be directly influenced by optical phase fluctuations, or spectroscopic transmission measurements, where intensity variations limit the achievable sensitivity [27]. Similarly, noise limits the data rate and transmission distance of fiber-optic systems [24, 28].

### 2.2.1 Main noise sources

There are five main sources of noise in solid-state devices [29]. The first source of noise is electron–hole recombination (shot noise), which is generated by the random emission of electrons or photons or by the random transit of carriers through potential barriers [22]. The second source is thermal noise, which is always present at any finite temperature, due to the random motion and collision of carriers with the diode laser lattice [30]. The third source of noise is the generation-recombination noise (GR noise), which is generated by the random generation and recombination of hole-electron pairs, or by the random generation of carriers from traps, or by the random recombination of carriers with empty traps [21]. The fourth source of noise is due to the spontaneous emission which is dominant in semiconductor lasers. Each spontaneously emitted photon adds a small field component whose phase is random to the coherent field (established by stimulated emission), and thus perturbs both amplitude and phase in a random manner [22]. Finally, flicker noise, also known as  $1/f$  noise (studied in this Thesis), is characterized by a  $1/f^\alpha$  spectrum with  $\alpha \simeq 1$  [29]. The overall consequence of these noise sources is variations in laser intensity, phase, and frequency even when the laser is biased at a constant current with minor current fluctuations. When semiconductor lasers are operated at constant current, intensity fluctuations result in a limited signal-to-noise ratio (SNR), whilst phase variations (studied in this Thesis) result in a finite spectral linewidth. Because such variations can have an impact on the performance of light wave systems, it is essential to determine their magnitude. [22].

### 2.2.2 Basic concept of oscillator

The perfect oscillator (pure sinusoid) generates a signal [31]

$$v(t) = V_0 \cos(\omega_0 t + \varphi) \quad 2.34$$

Where  $V_0 = \sqrt{2}V_{rms}$  is the maximum amplitude,  $\omega_0 = 2\pi\nu_0$  is the angular frequency, and  $\varphi$  is a constant that can be set to zero. However, in the real world, an oscillator signal fluctuates in amplitude and phase. The quasi-perfect sinusoidal signal is presented Figure 2-2 [31].

$$v(t) = V_0[1 + \alpha(t)] \cos[\omega_0 t + \varphi(t)], \quad |\alpha(t)| \ll 1, |\varphi(t)| \ll 1 \quad 2.35$$

If Equation (2.35) has a high signal-to-noise ratio, as a result, the following points are worth noting.

- The maximum amplitude  $V_0$  of Equation (2.34) is replaced by the envelope,  $V_0[1 + \alpha(t)]$ , where  $\alpha(t)$  is the random fractional amplitude. The assumption,  $|\alpha(t)| \ll 1$ , is due to practical oscillators exhibiting minimal amplitude fluctuations. Values  $|\alpha(t)| \in (10^{-3}, 10^{-6})$  are common in electronic oscillators [31].
- The constant phase  $\varphi$  of equation (2.34) is replaced by the random phase,  $\varphi(t)$ , which originates the bit error. In most cases, we can assume that  $|\varphi(t)| \ll 1$ . Drift is a term used to describe a slowly shifting phase. When observing a clock over time, the assumption  $|\varphi(t)| \ll 1$  is no longer valid. However, the carrier frequency can be divided by a sufficiently high rational number; Therefore, the phase scales down similarly, yielding the condition  $|\varphi(t)| \ll 1$  at low frequencies [31].

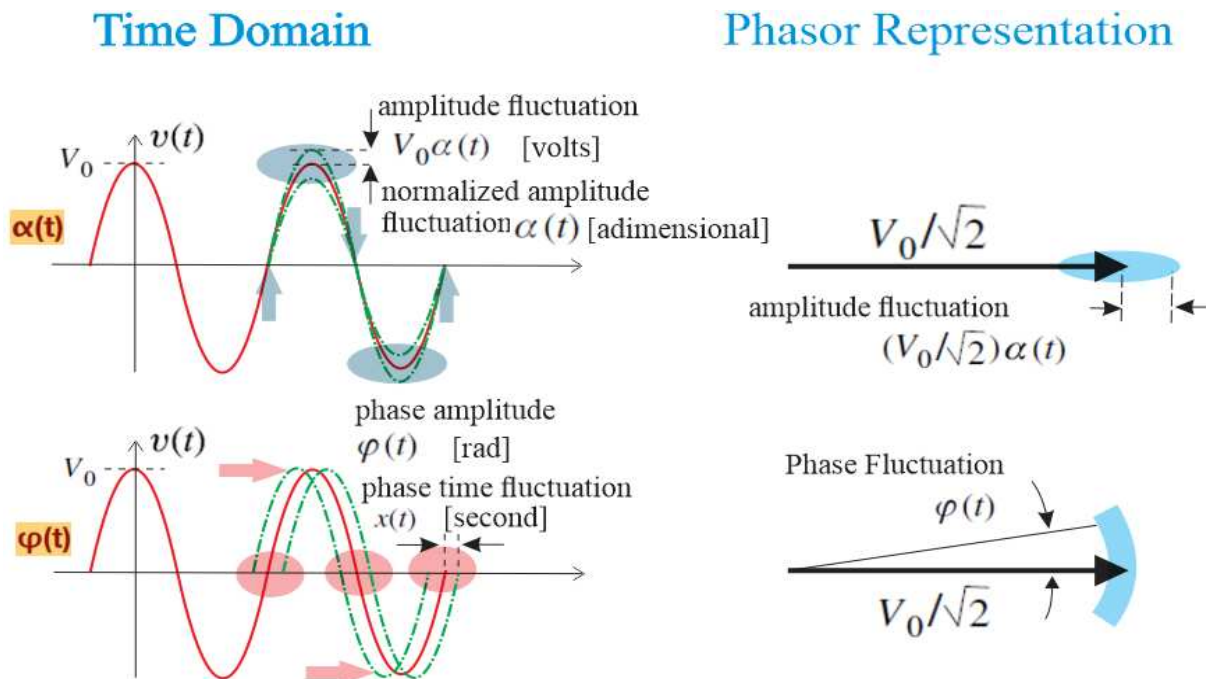


Figure 2-2 Amplitude and phase noise:  $V_0$  is in volts,  $\alpha(t)$  is non-dimensional,  $\phi(t)$  is in radians, and  $x(t)$  is in seconds. Adapted from [31].

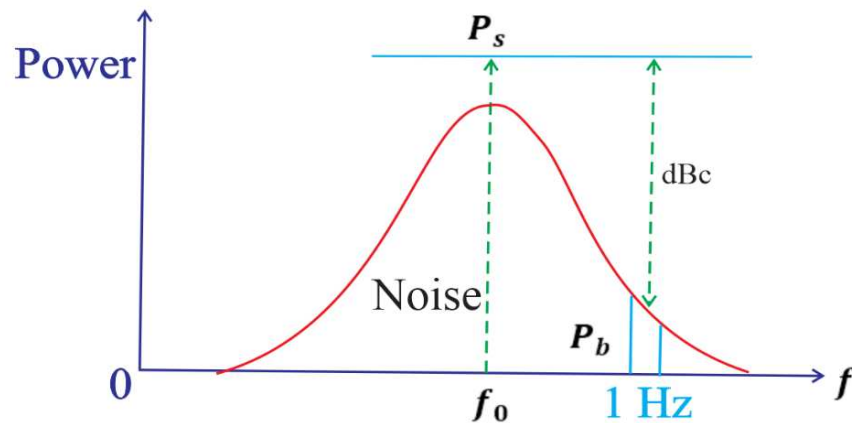


Figure 2-3 depicts the power distribution of a disturbed signal represented by equation 2.35.

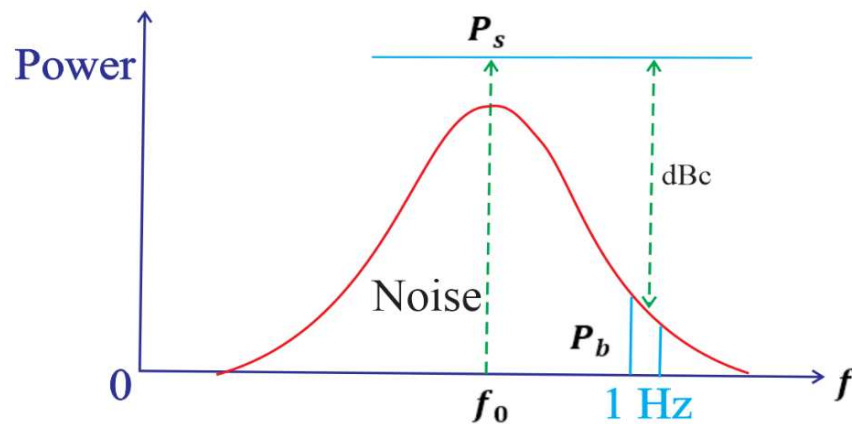


Figure 2-3 Power distribution of a real signal source Adapted from [31].

### 2.3 Relative Intensity Noise (RIN)

In practice, the light produced by any transmitter has power fluctuations. These fluctuations are referred to as intensity noise. The cause of these fluctuations, at the most fundamental level, originates from the quantum nature of the lasing procedure on its own [22]. Laser light intensity noise is one of the limitation factors in the transmission of analog or digital signals through fiber [32]. Power fluctuations are converted into current fluctuations by the optical receiver, which are added to those caused by shot noise and thermal noise and degrade the signal-to-noise ratio (SNR) and lower system performance [22, 32]. The spectral density of the relative intensity noise (RIN) is a typical parameter that indicates laser amplitude noise. This parameter that describes the laser amplitude noise at a given frequency,  $f$ , is determined by [21].

$$RIN = S_p(\omega)/P^2 \quad 2.36$$

where the spectral density

$$S_p(\omega) = \int_{-\infty}^{\infty} \langle \delta P(t + \tau) \delta P(t) \rangle e^{-j\omega\tau} d\tau \quad 2.37$$

The RIN normalized with the total optical intensity and usually measured in units of dB/Hz, is given by [32]

$$RIN(f) = \frac{\Delta P_{Opt}^2(f)}{P_{Opt}^2} \quad 2.38$$

where  $P_{Opt}$  is the laser average optical power and  $\Delta P_{Opt}(f)$  is the spectral density of the laser optical power fluctuations at frequency,  $f$ .

A peak can be seen in the density noise spectrum near the relaxation-oscillation frequency resulting from the laser's inherent resonance. The laser output oscillates for a few nanoseconds until reaching its steady-state CW value. These fluctuations are called relaxation oscillations, and the frequency of these fluctuations is defined by the nonlinear dynamics of photon-carrier interplay. The intensity noise typically peaks near the laser threshold and then quickly decreases as the driver current rises. [21]. The spectrum of intensity-noise fluctuations can be examined by utilizing a wide-bandwidth photodiode and a spectrum analyzer to detect the laser output. The noise spectrum associated with the total power is obtained as a result of such a measurement [26].

## 2.4 Phase noise and linewidth

There are applications for low phase-noise and narrow linewidth LDs, including applications in optical fiber communications, temperature and pressure sensing, medical ultrasound devices, temperature monitoring, wide-band fiber optic systems, monitoring of power grids, fiber optic interferometric sensors, low-phase-noise photonic oscillator fiber sensors, fiber acoustic sensors [33], optical clocks, gravitational wave detection [18], and for LIDAR spectroscopy[6].

Laser has a bandwidth (linewidth) in the width of the power spectral density of a laser's emitted electric field at its characteristic frequency or wavelength due to several physical mechanisms [34]. The most basic is the uncertainty principle, which prevents us from measuring the exact value of two energy levels from which a laser transition occurs. So, a

transition is not infinitely sharp, but rather has an interval proportional to the emission's bandwidth. Many other processes, such as the one induced by the limited lifespan of the carriers in the energy levels, Doppler broadening phonon, collision broadening, a characteristic of the laser gain material and the laser resonator design among others, widen the linewidth of a laser [34, 35]. The fluctuations of the refractive index of the semiconductor material often broaden the laser linewidth in the case of LDs, making this an additional broadening factor inherent to semiconductor lasers [36]. External factors have an impact on laser linewidth, which is influenced by optical phase fluctuations as well as noise induced by mechanical vibrations and temperature fluctuations [9, 34].

As a result, linewidth can be used to characterize the stability of the laser; it is also an important parameter for evaluating the practicality of the laser, and it affects laser performance [34]. The linewidth of a laser is the full width at half-maximum (FWHM) of its PSD. The temporal coherence, which is characterized by the coherence time or coherence length, is one of the most important factors in laser linewidth [10].

The type of the laser plays a major role in laser linewidth. It is also possible to estimate laser coherence degree by measuring the linewidth, when the laser coherence increases and the laser linewidth becomes narrower. Some techniques such as the laser design optimization and the noise suppression (like external noises) can minimize the laser linewidth [10]. Determining the spontaneous emission noise is an important factor that should be considered because the required measures can depend strongly on amplitude spontaneous emission noise. A laser with high intra-cavity power, a long resonator round-trip time, and low resonator losses are less affected by ASE noise. The LD linewidth is typically in the megahertz region; however, it is possible to reduce the linewidth to a few kilohertz, e.g. single frequency fiber lasers and external-cavity laser diode (ECLD), particularly with optical feedback from a high-finesse reference cavity [19].

Phase noise is caused by variations in the optical phase of the output. Due to various influences, even a single frequency laser will not produce a perfectly sinusoidal electric field oscillation at its output (intensity or phase fluctuations) [26]. The observed linewidth is due to the spectral broadening of each longitudinal mode caused by phase variations [21]. The laser linewidth is strongly connected to phase noise, however the laser linewidth conveys far less

information than the entire phase noise spectrum [26]. Quantum fluctuations related to the lasing process affect the optical field's strength and phase. [21].

The electromagnetic field of a laser source, described by Equation (2.39) [37, 38],

$$E(t) = E_0 \exp j[\omega(t) + \phi(t)] \quad 2.39$$

where,  $E(t)$ , is the amplitude fluctuation, and  $\omega$ , represents the angular frequency. However, phase fluctuations,  $\phi(t)$ , caused by spontaneous emission and non-linear quantum effects result in instantaneous frequency oscillations, which is given by the temporal derivative of the phase, as indicated in Equation (2.40). Thus, the frequency of the carrier optics is not a single value and there is a band of values that make up the laser emission spectrum. A change in phase causes a frequency shift. [21, 31].

$$\delta\omega(t) \equiv \delta\dot{\phi}(t) \quad 2.40$$

where  $\phi(t)$  represents the phase noise, (random phase fluctuation),  $\dot{\phi}(t)$  is the temporal derivative of the phase, and  $\delta$  represents infinitesimal variations in the phase,  $\phi$ , and angular frequency,  $\omega$ , of the optical carrier. The with  $\omega$  is in rad/s and  $\omega = 2\pi f$ , where  $f$  is the optical carrier frequency [31].

On the other hand, we can define  $x(t)$  as the phase-time fluctuation, i.e., the random phase fluctuation  $\phi(t)$  converted into time and measured in second [31].

$$x(t) = \frac{\phi(t)}{\omega} = \frac{\phi(t)}{2\pi f_0} \quad 2.41$$

Also, it is possible to determine the fractional-frequency fluctuation,  $y(t)$ , which is normalized to the carrier frequency  $f$  [31],

$$y(t) = \dot{x}(t) = \frac{\dot{\phi}(t)}{\omega_0} = \frac{(\Delta\omega)(t)}{\omega_0} = \frac{(\Delta f)(t)}{f_0} \quad 2.42$$

$\omega_0$  and  $f_0$  are the angular frequency and the oscillator frequency, respectively.

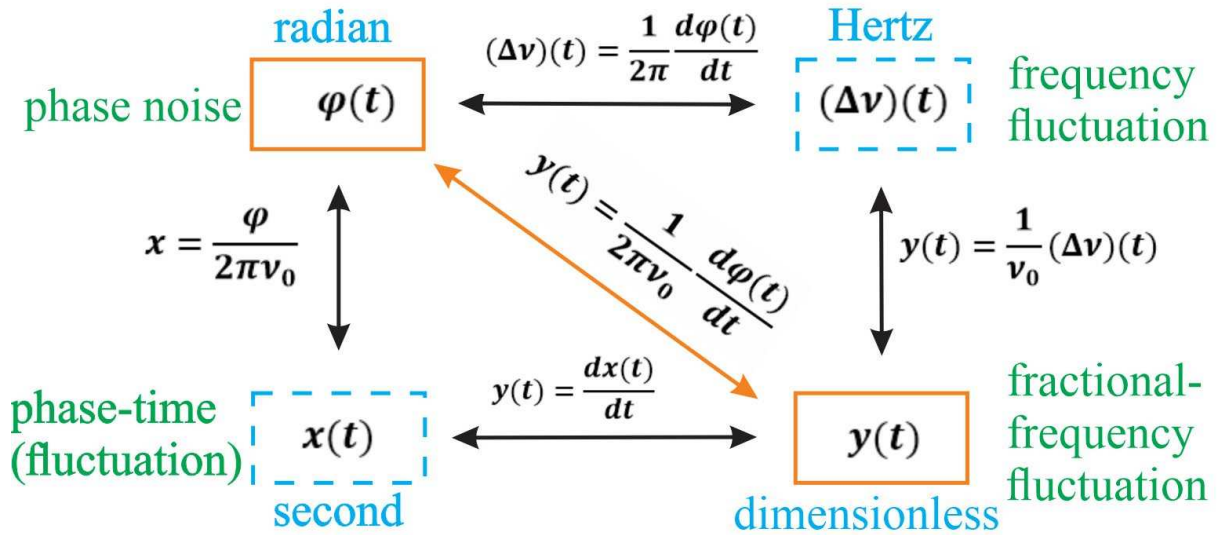


Figure 2-4 The relations between phase noise or fluctuations  $\phi(t)$ , frequency fluctuation  $\omega(t)$ , fractional-frequency fluctuation  $y(t)$  and the phase-time fluctuation  $x(t)$ .

The performance of coherent optical communication systems is affected by frequency or phase noise. The greater the linewidth of the optical source, the greater the susceptibility of the transmitted beam to scattering effects in optical fibers and to other nonlinear effects, such as Brillouin's stimulated scattering [22]. The linewidth of a single longitudinal mode in CW operation is a consequence of phase variations within the laser. The solution of equation (2.33) can be used to calculate the frequency-noise spectrum and linewidth.

Phase variations are caused by two mechanisms. The first one is spontaneous emission that cause stochastic variations in the phase of the emitted signal,  $\tilde{F}_\phi$ , which is shown in the Fourier transform of the Langevin force in equation (2.33). The spontaneous emission of photons is directly related to random alterations in the optical phase of the signal. This process is intrinsic to the operation of the laser itself and, therefore, unavoidable. The second mechanism is the variations in the carrier populations shown in second term of equation (2.33), the term involves the  $\beta_c$  parameter that also causes phase change. Changes in  $N$  have an impact on the phase because they alter optical gain, refractive index, and optical path length. The gain and index change apportionment are set by the factor  $\beta_c$  (see equation 2.12). It is also known as the *line-width enhancement factor* and its contribution in the laser spectral broadening, is close to  $1 + \beta_c^2$  [21].

The spectral intensity of the frequency noise is defined through the expression in [21].

$$S_{\phi}(\omega) = \int_{-\infty}^{+\infty} \langle \delta\phi(t + \tau)\delta\phi(t) \rangle e^{-j\omega\tau} d\tau \quad 2.43$$

This equation can be simplified in cases where the analysis directly involves the Fourier transform of the function under analysis, as presented in (3.42)

$$S_{\phi}(\omega) = \lim_{T \rightarrow \infty} \left( \frac{1}{T} |\delta\tilde{\phi}(\omega)|^2 \right) \quad 2.44$$

Equation (2.43)'s ensemble average was changed to a time average over the duration  $T$  presuming an ergodic random variable, and the result is [21].

$$\lim_{T \rightarrow \infty} \left( \frac{1}{T} [\tilde{\phi}_i^*(\omega)\tilde{\phi}_j(\omega)] \right) = 2D_{ij} \quad 2.45$$

where  $D_{ij}$  are the diffusion factors between the rate equations, presented in (2.22) and (2.23). By applying the Fourier transform of the rate equation for changes in the phase of the optical carrier, under the influence of Langevin forces given in (2.33), to the expression in (2.44), we have equation (2.46): [21].

$$S_{\dot{\phi}}(\omega) \approx \frac{R_{sp}}{2P} \left[ 1 + \frac{\beta_c^2 \Omega_R^4}{(\Omega_R^2 - \omega^2)^2 + (2\omega\Gamma_R)^2} \right] \quad 2.46$$

This expression was simplified by considering that  $\delta\bar{N}$ , in (2.33), varies predominantly due to the term  $(G + G_p P)\tilde{F}_p$  in (2.32). It is interesting to observe that, although Langevin forces have intensity independent of the frequency of the emitted signal, the phase noise will have greater intensity at the relaxation frequency of the laser semiconductor structure,  $\Omega_R$ . This phenomenon results from the appearance of resonances at such frequencies, which end up amplifying the emitted noise, both in phase and in amplitude, in this region.

By measuring the light source spectrum with a high-resolution Mach Zehnder interferometer, one can characterize the exploratory linewidth of a single longitudinal mode. By using the Fourier transform of the field autocorrelation, the power spectrum is calculated and provided by [21].

$$S_E(\omega) = \int_{-\infty}^{\infty} \langle E^*(t + \tau)E(t) \rangle \exp(-i\omega\tau) d\tau \quad 2.47$$

where  $E(t)$  is the optical field and given by [21]

$$E(t) = \sqrt{P + \delta P} e^{-j(\omega_0 + \phi + \delta\phi)} \quad 2.48$$

where  $E(t)$  is the output amplitude, given as a function of photon number  $P$ , emitted in steady state, and the phase, under the same conditions, and  $\omega_0$  is the investigated single longitudinal mode's frequency.

Using the small-signal solution provided by equations (2.31)-(2.33), the power spectrum  $S_E(\omega)$  can be derived. It is made up of a center peak at the mode frequency  $\omega_2$ , and lower intensity lateral components separated at intervals equal to the relaxation frequency,  $\omega_0 \pm n\Omega_R$  ( $n$  being an integer) which these side peaks are caused by relaxation oscillations. To make the analysis simpler, we ignore intensity variations and set  $\delta P$  to 0 in equation (2.48). This generalization only has one effect: side-peak differential is no longer taken into account in the theoretical analysis. In order to focus the analysis only on the phase optical carrier distortions, we have (2.49): [21].

$$S_E(\omega) = P \int_{-\infty}^{+\infty} \langle e^{j\Delta_\tau\phi} \rangle e^{-j(\omega - \omega_0)\tau} d\tau \quad 2.49$$

$$\text{Where } \Delta_\tau\phi = \delta\phi(t + \tau) - \delta\phi(t) \quad 2.50$$

is the difference in phase fluctuations at times  $t$  and  $t + \tau$ . Assuming that  $\Delta_\tau\phi$  has a Gaussian distribution. The average in equation (2.49) is abtained by [21].

$$\langle \exp(i\Delta_\tau\phi) \rangle = \exp \left[ -\frac{1}{2} \langle (\Delta_\tau\phi)^2 \rangle \right] \quad 2.51$$

To calculate the variance  $\langle (\Delta_\tau\phi)^2 \rangle$  related to the stationary random process  $\Delta_\tau\phi$  and we observe Fourier transform of equation (2.50) this relation is obtained [21].

$$\Delta_\tau\phi = \frac{1}{2\pi} \int_{-\infty}^{\infty} \delta\tilde{\phi}(\omega) [e^{i\omega\tau} - 1] e^{i\omega\tau} d\omega \quad 2.52$$

The cross-correlation between the frequency components  $\delta\tilde{\phi}(\omega)$  disappears, therefore it is possible to show [21].

$$\langle (\Delta_\tau\phi)^2 \rangle = \frac{1}{\pi} \int_{-\infty}^{\infty} \langle |\delta\tilde{\phi}(\omega)|^2 \rangle (1 - \cos \omega\tau) d\omega \quad 2.53$$

By applying  $\tilde{\phi}(\omega)$  the equation (2.33) and calculating the average using the equation (2.44), this relation is obtained [21].

$$\langle (\Delta_\tau \phi)^2 \rangle = \frac{R_{sp}}{2P} \left\{ (1 + \beta_c^2 b) \tau + \frac{\beta_c^2 b}{2\Gamma_R \cos \sigma} [\cos 3\sigma - e^{-\Gamma_R \tau} \cos (\Omega_R \tau - 3\sigma)] \right\} \quad 2.54$$

Where

$$b = \frac{\Omega_R}{\sqrt{\Omega_R^2 + \Gamma_R^2}} \quad \text{and} \quad \sigma = \tan^{-1} \left( \frac{\Gamma_R}{\Omega_R} \right) \quad 2.55$$

By inserting equations (2.51) and (2.54) into equation (2.49) and assessing the Fourier transform numerically, the optical spectrum is derived. The laser power spectrum is shown in Figure 2-5. Since the spectrum is symmetric in relation to central frequency,  $\omega_0$ , only half of that is display [21] which is called one-sided PSD while physicists usually employ two-sided PSDs, in which the integration also must include negative frequencies [26]. It is made up of a main central crest at  $\omega_0$  and several side peaks at  $\omega_0 + m\Omega_R$ , where m is an integer. It is worth noting that these amplitude side peaks decrease through the frequency spacing, therefore only the first pair of side peaks positioned at  $\omega = \omega_0 \pm \Omega_R$  is often observed experimentally. When the laser power is increased, the side peaks lose amplitude while the central peak shrinks. As a result, the location and magnitude of side peaks are greatly reliant on the frequency and damping rate of relaxation oscillations, which in turn influenced by the laser power. The central peak dominates the spectrum at a power of a few mW and its width defines the laser linewidth.

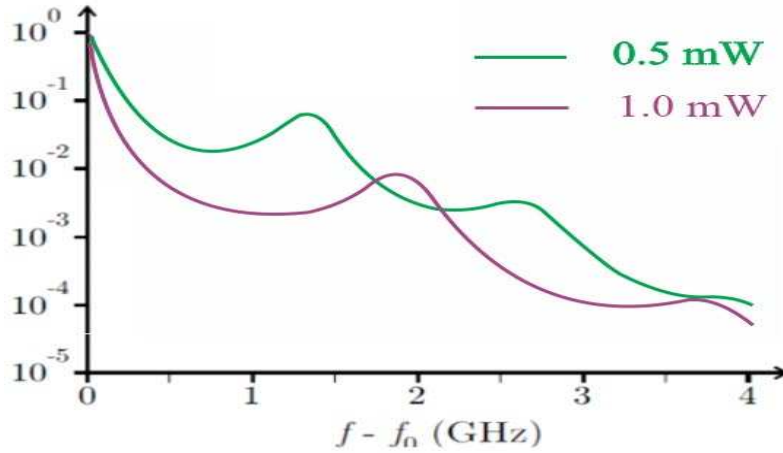


Figure 2-5 Numerical resolution of the optical carrier power spectrum emitted by a semiconductor laser for two output optical signal powers. The phenomenon of spectral broadening due to distortions in its phase is perceived (adapted from [21]).

To get approximation we use the spectral density of the frequency noise, which is given by [21].

$$S_{\dot{\phi}}(\omega) = \langle |\omega \delta \tilde{\phi}(\omega)|^2 \rangle \quad 2.56$$

Then an approximation for the power spectrum is obtained by inserting Eq. (2.56) to Eq. (2.53) and resulted in [21],

$$\langle (\Delta_{\tau} \phi)^2 \rangle = \frac{1}{\pi} \int_{-\infty}^{+\infty} S_{\dot{\phi}}(\omega) \frac{1 - \cos \omega \tau}{\omega^2} d\omega \quad 2.57$$

The frequency-noise spectral density  $S_{\dot{\phi}}(\omega)$  is given by equation. (2.46)

the power spectrum's side peaks are originated by the relaxation-oscillation-induced enhancement of  $S_{\dot{\phi}}(\omega)$  at  $\omega = \Omega_R$ . If we disregard this improvement and assume that  $S_{\dot{\phi}}(\omega)$  is steady and substitute it with its value at  $\omega = 0$  the integration is simplified. The outcome is [21].

$$\langle (\Delta_{\tau} \phi)^2 \rangle = \tau S_{\dot{\phi}}(\omega) \quad 2.58$$

The power spectrum can be modified into simple Lorentzian centered at  $\omega = \omega_0$  with a FWHM of  $\Delta\omega = S_{\dot{\phi}}(\omega)$  by using equations (2.49), (2.51), and (2.58). The line width  $\Delta f$  is given by using  $\Delta\omega = 2\pi\Delta f$  [21].

$$\Delta f = \frac{1}{2\pi} S_{\phi}(0) = \frac{R_{sp}(1 + \beta_c^2)}{4\pi P} = (1 + \beta_c^2)\Delta f_0 \quad 2.59$$

This formula known as the modified Schawlow-Townes formula, where composed from two terms which caused by instantons and delayed phase fluctuation resulting from each spontaneous emission. The  $\Delta f_0$ , is related to the linewidth that the laser presents due to the Langevin force,  $F_{\phi}(t)$  (see Eq. 2.26). The second term,  $\beta_c^2\Delta f_0$ , is random phase variations to the laser's emission due to the  $\delta N$  in equation (2.26); The origin of  $\delta N$  can be explained by the sequence of events.

Every spontaneously produced photon modifies the laser power, that further alters the gain,  $G$  (or alternatively, the carrier population), that also alters the refractive index,  $\eta$ , and consequently the optical phase,  $\phi$ . The delay phase fluctuation,  $\dot{\phi}$ , is affected by relaxation oscillations,  $\Gamma_p$ , and consequently, in the frequency of the emitted signal, resulting in appearance of relaxation peaks at frequencies spaced by  $\Omega_R$ . The formula 2.59, which concludes, demonstrates that a semiconductor laser's line width is increased by a criterion of  $1 + \beta_c^2$  and causes the broadening of the central peak as well.

There are two methods to reduce the linewidth, one of which is, using a multi quantum-well (MQW) design for the distributed feedback laser (DFB). In this case the linewidth reduction results from reduced value for the variable,  $\beta_c$ . The second approach to reducing line width is to increase cavity length  $L$  [21] and/or a high facet reflectivity [39], which results in a decrease in spontaneous emission,  $R_{sp}$ , and an increase in the number of released photons (or the photon lifetime),  $P$ , at a given output power. When the length dependence of  $R_{sp}$  and  $P$  is considered,  $\Delta f$  can be demonstrated to vary as  $L^{-2}$  [21].

Figure 2-6 provides a generalized view of linewidth variation as a function of laser output power by presenting experimental results for three lasers with different cavity sizes and designs. As expected from the equations shown above, there is a strong tendency to decrease the linewidth as the laser output optical power increases. However, after such a drop, the line width reaches a point of apparent saturation, it increases again, whilst the optical output power increases. Several explanations proposed to account for such behavior; Side-mode interplay,  $1/f$  noise, nonlinear gain, spatial-hole burning, and source current noise are a few examples. [21].

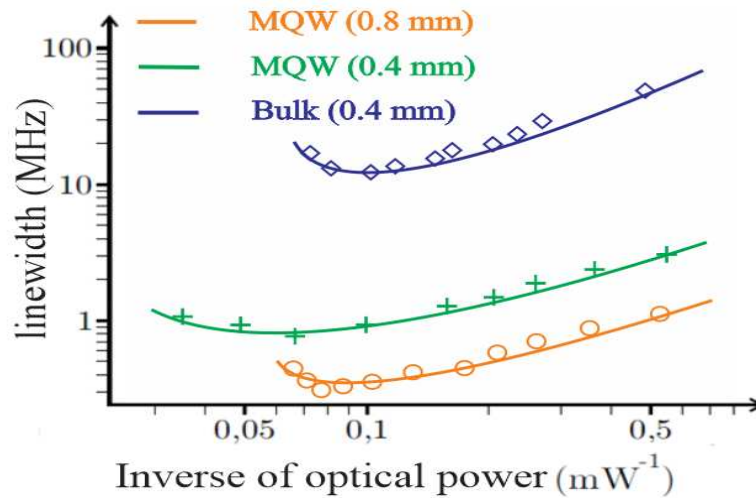


Figure 2-6 Line width as a function of the experimentally characterized optical output power for three lasers with different heterojunction architectures. Two designed with multiple quantum wells (with  $400 \mu\text{m}$  and  $800 \mu\text{m}$  cavities) and one bulk (with  $400 \mu\text{m}$  cavity) (adapted from [21]).

## 2.5 Linewidth Function

Many factors influence the shape and spectral linewidth of a laser, resulting in natural linewidth broadening. The goal of this section is to recognize the various widening categories and to provide an analytic expression for the linewidth function where possible  $g(\nu)$ . The light spectrum generated by the laser is influenced by the linewidth of the atomic transitions' emission, the optical amplification process, the active material, and the resonant cavity's oscillation modes [40]. After that, for the design and evaluation of coherent optical links, a precise assessment of the optical carrier's phase and frequency distortions is essential; the following sections present the theoretical basis of the nature of phase noise, as well as its relationship with the linewidth in semiconductor lasers [28, 39].

All atomic transitions have a limited width due to a theory of uncertainty, and there are two main types of processes that influence a spectral line's width:

1. Homogeneous broadening: All atoms are affected by a mechanism.
2. Inhomogeneous broadening: It results from an obvious distinction between atom group compositions.

In practice, a combination of both types is present. However, in some cases, due to the complexity of the mathematical analysis, we proceed by selecting the dominant one [41].

By transmitting energy to the atoms of a medium, electrons of a certain energy level can be excited to a higher level. After some time, when electrons release the extra energy, they decay to a lower level emitting spontaneous electromagnetic radiation, this phenomenon known as fluorescence. The radiation emitted by the spontaneous atomic transition between two levels is not monochromatic, but occupies a finite frequency bandwidth that can be characterized by the linewidth function  $g(\nu)$ , which establishes a link between the normalized energy density distribution and the emitted frequency, given by [42]:

$$\int_{-\infty}^{\infty} g(\nu) d\nu = 1 \quad 2.60$$

The probability of spontaneous emission of a photon from excited to lower level, whose photon frequency is between  $\nu$  and  $\nu + d\nu$ , is defined by the integrand of equation (2.60). One approach for defining the line width  $g(\nu)$  is to apply an electromagnetic field to the sample to create electronic transitions from the lower to the upper level, and then measure the absorbed energy as a function of frequency or wavelength. From basic quantum mechanical considerations, the emission and absorption are characterized by the same linewidth function, the emission spectrum can be viewed the same as observed in the absorption spectrum [42]. Another approach measures the fluorescent curve effectively as a response to the frequency using an optical monochromator. [27].

### 2.5.1 Natural Linewidth with homogeneous broadening

The spectrum distribution of emitted radiation from a two-level atomic system around the angular frequency  $\omega_0$  is defined by the normalized line shape function which is a damped oscillating dipole Fourier spectrum [42]:

$$f(\omega) = \frac{\gamma}{[(\omega_0 - \omega)^2 + (\gamma/2)^2]} \quad 2.61$$

By using (2.61) and (2.60), The atomic transition's lineshape function is written [42]:

$$g(\nu) = \frac{1}{2\pi} \frac{\gamma/2\pi}{(\nu - \nu_0)^2 + (\gamma/4\pi)^2} \quad 2.62$$

Where  $\gamma$  is the damping factor and  $\nu_0 = \omega_0/2\pi$ . The linewidth is defined as the  $\Delta\nu$ , which is the distance between the two frequencies at which the Lorentzian lineshape function is reduced to half of its maximum value, and it is provided by [42]:

$$\Delta\nu = \gamma/2\pi \quad 2.63$$

Then we can rewrite the equation (2.62) in terms of the linewidth  $\Delta\nu$ . The Fourier transform of the field emitted by the oscillator has the normalized linewidth function in the shape of a Lorentzian, centered on the transition frequency  $\nu_0$  [42]:

$$g(\nu) = \frac{\Delta\nu}{2\pi[(\nu - \nu_0)^2 + (\Delta\nu/2)^2]} \quad 2.64$$

The finite lifetime  $\tau$  of the emitting state is one of the proposed explanations for the frequency expansion of spontaneous emission. Given to classical physics and the electron motion equation, it is possible to show that the damping factor is proportional to the inverse of spontaneous lifespan [42].

$$\gamma = 1/\tau \quad 2.65$$

Then the linewidth can be calculated using Equation (2.63) [42].

$$\Delta\nu = \frac{1}{2\pi\tau} \quad 2.66$$

The spontaneous lifespan  $\tau$ , which causes the linewidth broadening, is comprised of three other components: first is the finite lifetime of the upper state  $\tau_u$ , second is the finite lifetime of the lower state  $\tau_l$  which is also observed in many laser systems, and the third one is the collision time  $\tau_{co}$ . Due to elastic collisions with other atoms, the radiating field from an atom may experience an abrupt phase shift during the process of coherent radiation. Therefore, the overall linewidth broadening is the sum of these three components. Then, we can generalize equation (2.66) [42].

$$\Delta\nu = \frac{1}{2\pi} (\tau_u^{-1} + \tau_l^{-1} + \tau_{co}^{-1}) \quad 2.67$$

The above-described sort of broadening is known as homogeneous broadening. In this type of broadening, each individual atom has the same frequency spectral distribution function  $g(\nu)$ ,

equation (2.64), and it explains the response of each atom, which are indistinguishable. As a result of which, the applied electromagnetic field has the same effect on every atom in the collection and they equally and homogeneously broadened.

As previously stated, the three most typical mechanisms that induce the finite interaction lifetime of the emitting or absorbing atoms and, as a result, the homogeneous broadening, are as follows [42].

1. The spontaneous emission of electromagnetic radiation. The spontaneous emission line is extended due to finite time decay of the excited state,  $\tau$ . The radiation emission, due to the transition from an excited state with the energy level  $E_j$  to the lower energy level  $E_i$ , can be considered as a damped oscillator with time constant.
2. A phonon collides with an atom embedded in a crystal. In this process, acoustic energy can be emitted or absorbed. The lifetime of the atom in its absorbing or emitting state is not extinguished by such a collision. It does, however, cause a broadening of the radiation by altering the relative phase between the atomic oscillation and the field oscillation.
3. One other significant homogeneous broadening is pressure broadening in a gas. Through this process, the lifetime termination and phase interruption dominate the broadening process as in the preceding mechanism, when atomic concentrations are high enough to induce enough frequent collisions between atoms [42].

### 2.5.2 Natural Linewidth with inhomogeneous broadening

In several situations, distinct atoms in a group of similar atoms may have slightly differing transition resonant frequencies  $\omega_{a_i}$ , resulting in a random distribution of these transition resonant frequencies,  $\omega_{a_i}$ , for different atoms around a central frequency,  $\omega_{a_0}$ . For each atom in the collection, the resonance frequencies,  $\omega_{a_i}$ , are randomly shifted by small amounts. An electromagnetic wave travelling through such atoms observes a total response to all atoms, and it is not possible to identify those atoms at specific frequency shifts and individual responses. As a result, the collective responding of all atoms will be widened by the aggregate of all the individual atoms' randomly shifting responses. As a result, the overall response (lineshape) will be significantly increased. However, the amplitude of the response,

near the line center, will be greatly reduced. Inhomogeneous broadening is the term for this pattern of actions., as shown in Figure 2-7 [27].

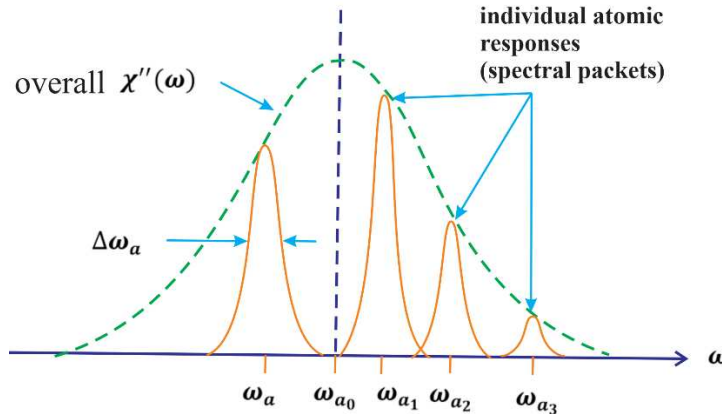


Figure 2-7 An inhomogeneously broadened atomic transition, with individual atomic responses, or "spectral packet". Adapted from [27].

### 2.5.3 Definition of spectral packets, strongly inhomogeneous and strongly homogeneous

One spectroscopic packet is described as a sub-group of atoms for whom frequency response  $\omega_{a_i}$  all drop within a scope of roughly one homogeneous linewidth around a specific property of  $\Delta\omega_{a_i}$ . A single spectral packet of atoms has a generally uniform (homogeneous) reaction to an applicable electromagnetic wave. The overall answer of an inhomogeneously broadened line can be calculated by adding the individual results of all the spectral packets with a specific resonance frequency,  $\omega_{a_i}$ . We can divide the widening into two categories based on the characteristics of the spectral packets [27]:

1. Strongly inhomogeneous: if the independent packets' frequency shifts considerably around  $\omega_{a_0}$  by a significant amount in comparison to their individual homogeneous widths [27].
2. Strongly homogeneous: The line will remain largely homogeneous if the inhomogeneous displacement is minimal in comparison to the homogeneous packet sizes, and the tiny proportion of inhomogeneous broadening that exists will be of negligible significance [27].

### 2.5.4 Causes of inhomogeneous broadening

Besides the homogeneous procedures for a particular transition, more than one mechanism is frequently at work. However, the following are the two most important mechanisms for inhomogeneous broadening [27]:

1. Because of defects, dislocations, or lattice impurities, depending on their location within the lattice, laser atoms may see widely differing local environments or distinctive local structural properties. As a result, the actual energy levels of the atoms have slightly distinct values, causing minor variations in transition frequency. So that each atom's crystallite neighbors are comparable, but because they oscillate quickly and arbitrarily over time, a vibrant homogeneous phonon expansion result. On the other hand, when the neighbors vary from point to point but are static over time, they create an inhomogeneous network expansion or strain expansion, consequently, the transition frequencies are spread out [27].
2. The other main mechanism is Doppler-shifted. In gases, the kinetic energy speeds at which various atoms move through space vary. The imposed signal's frequency as seen by the atom changes due to this kinetic motion, or the atom's perceptible vibrations changes due to this movement,  $\omega_{a_i}$ , as observed by the applied signal. The doppler broadening of transformation at optical frequencies in atomic and molecular gases is a major and pervasive source of inhomogeneous broadening [27].

In gases when a travelling atom at  $V_z$  interacts with an electromagnetic wave of signal frequency  $\omega$  at velocity  $c$  along the  $z$  direction (Figure 2-8), the wave frequency observed by the atom changes with Doppler broadening effect to a new value  $\omega'$ , provided by [27],

$$\omega' = (1 - v_z/c)\omega \quad 2.68$$

However, from the other point of view, the observant from the laboratory will see the frequency of the atom's vibration changed by Doppler broadening to a new value [27],

$$\omega_a = (1 + v_z/c)\omega_{a0} \quad 2.69$$

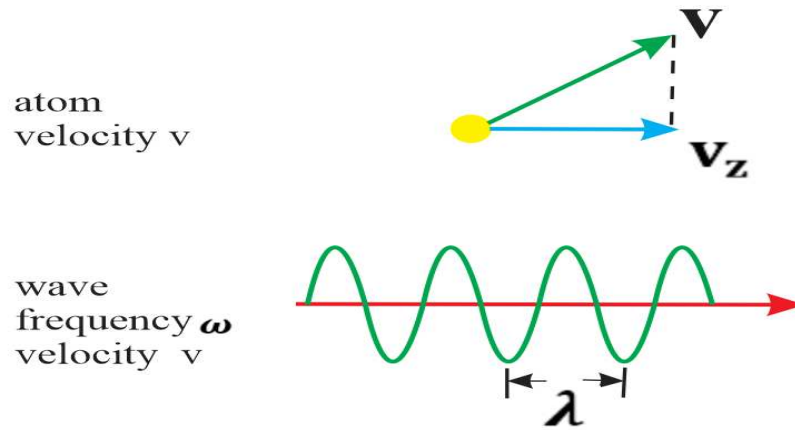


Figure 2-8 An atom traveling across an electromagnetic wave experiences a Doppler shift. Adapted from [27].

The average doppler shift for a travelling gas atom is given by [27], (for typical atomic and masses and temperatures )

$$\frac{\omega_a - \omega_{a0}}{\omega_{a0}} \approx \sqrt{\frac{kT}{Mc^2}} \approx 10^{-6} \quad 2.70$$

Where  $M$  is an atom or molecule of mass,  $T$  is the gas temperature, and  $\omega_{a0}$  is the center frequency. Therefore, a real gas's volume of doppler broadening is determined by the gas's kinetic temperature  $T$  as well as the atom's or molecule's molecular weight.

In the Doppler broadening of the atomic transition,  $g(\omega_a)$ , the inhomogeneous distribution function of frequency shift has a Gaussian form, and is given by [27],

$$g(\omega_a) = \left( \frac{4 \ln 2}{\pi \Delta \omega_d^2} \right)^{1/2} \exp \left[ - (4 \ln 2) \left( \frac{\omega_a - \omega_{a0}}{\Delta \omega_d} \right)^2 \right] \quad 2.71$$

The inhomogeneous linewidth  $\Delta \omega_d$  measured at the half power level (FWHM - Full width at half maximum) has the Gaussian distribution, The function  $g(\omega_a)$  is clustered very narrowly around the central frequency  $\omega_{a0}$  and given as follows [27],

$$\Delta\omega_d = \sqrt{\frac{(8\ln 2)kT}{Mc^2}} \omega_{a0} \quad 2.72$$

Figure 2-9 demonstrates the Lorentzian and Gaussian outcomes from strongly homogeneous and strongly inhomogeneous adjustments to the identical FWHM linewidth and region. Although the apex of the Gaussian absorption graph is nearly 50% greater than that of the Lorentzian, it falls off much more quickly in the wings. Due to the 50 percent higher peaks at the center balancing the lower area in the wings of the Gaussian profile, thus every graph has the same incorporated area. The homogeneous packet linewidth  $\Delta\omega_a$  does not appear whatsoever in the strongly inhomogeneous case, it is worth noting. The homogeneous linewidth  $\Delta\omega_a$  of the packets buried within the line can be measured when measuring the response of a strongly inhomogeneous line, but not to 1st sequence. [27].

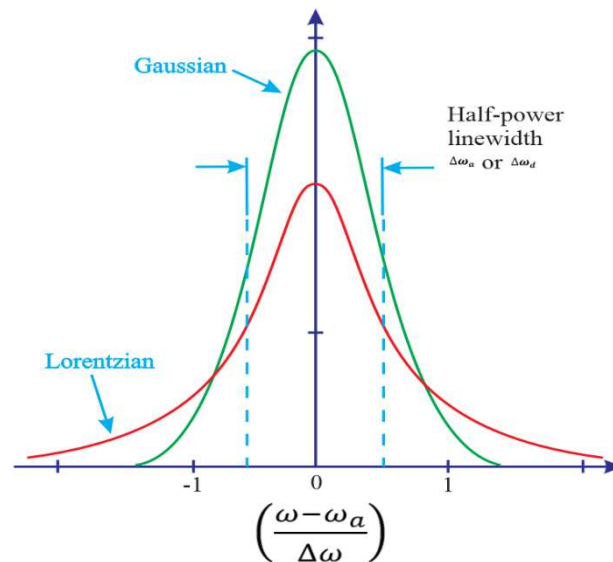


Figure 2-9 Lineshapes with the same half-power linewidth and total area are compared between gaussian and Lorentzian. Adapted from [27].

The ratios of inhomogeneous broadening  $\Delta\omega_d$  to homogeneous broadening  $\Delta\omega_a$  can help us to evaluate the approximation of inhomogeneous distribution  $g(\omega_a)$ , and classify this into three categories [27].

1. Strongly Homogeneous Limit: if  $\Delta\omega_d \ll \Delta\omega_a$ , In this case, the impacts of inhomogeneous broadening are minor. In other words, individual packet resonance frequencies are only

slightly shifted compared to the homogeneous linewidth  $\Delta\omega_a$ . In the case of strongly Homogeneous Limit, it shows the Lorentzian lineshape [27].

2. Strongly Inhomogeneous Limit: if  $\Delta\omega_d \gg \Delta\omega_a$ , In compared to their homogeneous linewidth  $\Delta\omega_a$ , the inhomogeneous linewidth  $\Delta\omega_d$  is large enough to alter the frequency of the spectral packets significantly, resulting in a large number of packets inside the overall linewidth. In the case of strongly Inhomogeneous Limit, it shows the Gaussian lineshape [27].
3. Intermediate Region (Voigt Profiles): if  $\Delta\omega_a \approx \Delta\omega_d$ , The area's line patterns are unmistakably halfway between gaussian and Lorentzian. The proportion of the homogeneous and inhomogeneous linewidths, or more precisely, both of them, determines the precise form of the Voigt profile.

Figure 2-10 demonstrates the carbon monoxide absorption profile in comparison to the Gaussian and Voigt functions. In fact, the Voigt profile is result from convolving the Gaussian and the Lorentzian spectrum and Deconvolution of the Lorentzian and Gaussian contributions can also be achieved by mathematically adapting the evaluated graph to a calculated Voigt characteristics with the proper ratio of  $\Delta\omega_a/\Delta\omega_d$  [27].

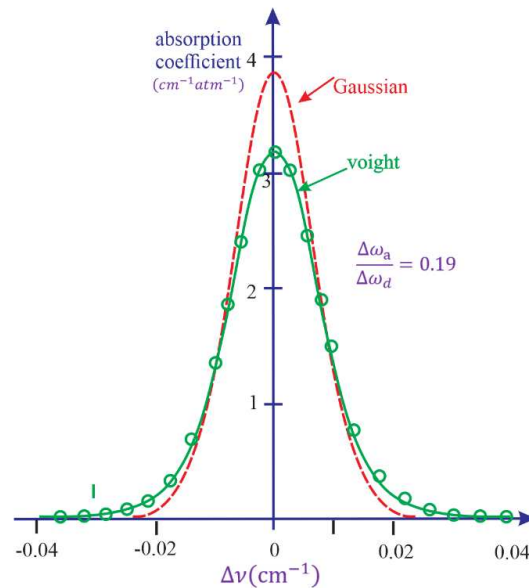


Figure 2-10 Gaussian and Voigt features with the same half-power values were compared to the carbon monoxide absorption profile (circles) through measurement. Adapted from [27]

## 3 Self-Homodyne Detection for Laser Noise Characterization

Indirect frequency domain measurements can be used to investigate the phase noise of lightwave signals. The self-homodyne beating of this signal with a portion of the same carrier for example, can be used to determine the optical carrier linewidth. To break the wave coherence, one portion of the optical carrier must be delayed in time by propagating in a spool of optical fiber with sufficient length. This chapter gives a study of the self-homodyne method for measuring the laser's spectral linewidth using an unbalanced Mach-Zehnder optical fiber interferometer. Due to the phase fluctuations in the non-coherent laser regimes, some models for the experimental spectra are investigated.

### 3.1 Power spectrum measurement

The most popular instance of a power spectrum is when a prism converts white light into a seamless range of rainbow colors. The distribution of light power on the frequency or wavelength position can be determined through this test. The electrical spectrum analyzer is, similarly, a tool with adjustable filters that can be used to measure the power distribution in the frequency range, in a sweep mode with finite bandwidth  $B$  around a center frequency  $f$ . To put it simply,  $S_x(f)$  can be considered as the average power of  $x(t)$  centered at frequency  $f$ , but measured at an appropriate narrow frequency slot, a 1 Hz bandwidth, to exclude the effects of slope; a typical power spectral density plot is shown in Figure 3-1 [31].

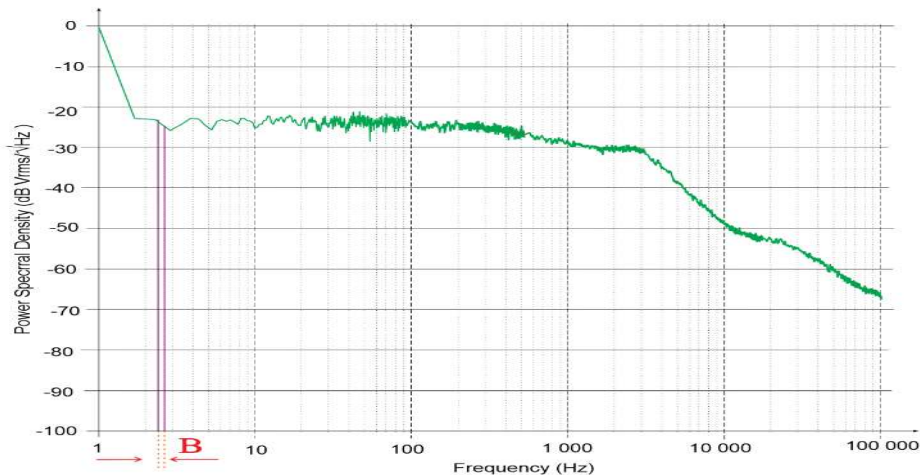


Figure 3-1 A typical power spectral density

All the functions for characterizing a random process, such as average, autocorrelation, etc., are deal with in the time domain; therefore, to understand the properties of a random process in the frequency domain, its spectral components are obtained by the Fourier transform of the time data. For a deterministic signal  $X(t)$  its spectral components are given by its Fourier transform  $X(w)$  [43],

$$S(w) = \int_{-\infty}^{\infty} X(t) e^{-j\omega t} dt \quad 3.1$$

In contrast, given the  $SX(w)$ , using the inverse Fourier transform, we can retrieve  $X(t)$  [43]:

$$X(t) = \frac{1}{2\pi} \int_{-\infty}^{\infty} S(w) e^{j\omega t} d\omega \quad 3.2$$

The power spectral density,  $S_{XX}(w)$ , of a random process is the Fourier transform of the autocorrelation function  $R_{XX}(\tau)$  for a stationary process. Hence [31, 43]:

$$S_{XX}(w) = \int_{-\infty}^{\infty} R_{XX}(\tau) e^{-j\omega \tau} d\tau \quad 3.3$$

$R_{XX}(\tau)$  can be recovered using the inverse Fourier transform as follows [43]:

$$R_{XX}(\tau) = \frac{1}{2\pi} \int_{-\infty}^{\infty} S_{XX}(w) e^{j\omega \tau} d\omega \quad 3.4$$

As a physical quantity, the one-sided power spectral density  $S_x(f)$  relating to a stochastic function  $x(t)$  can be operationally defined as a distribution with the following attributes:

1. The signal power ( $P_{ab}$ ) in the interval of  $(a, b)$  is the integral over that interval [31]:

$$P_{ab} = \int_a^b S(f) df \quad 3.5$$

This formula serves as the basis for the monochromator and enables us to separate a semi light source from a white light signal. Additionally, we can look at the lightwave, describe how different colors predominate, and identify the fingerprint of atoms, ions, and molecules. This is how spectroscopy works at its core.

2. The energy in two different frequency spaces  $(a, b)$ , and  $(c, d)$ , added together [31]:

$$P_{ab} + P_{cd} = \int_a^b S(f)df + \int_c^d S(f)df \quad 3.6$$

This allowed the cell phone industry to greatly expand the number of calls that could be handled simultaneously and increased their reliability, as four separate frequencies provided multiple pathways for signal transmission.

3. The total energy of the signal is its integral through all frequencies. This is necessary for energy conservation [31].

$$P = \int_0^{\infty} S(f)df \quad 3.7$$

This energy conservation principle is central to modern communication systems and allows us to understand how signals are transferred from one point to another.

## 3.2 Coherence function

The statistical features of light influence many optical experiments. The coherence functions are well adequate for predicting some experimental results. Coherence is classified into two types: temporal coherence and spatial coherence. The ability of a light beam to interfere with a delayed (but not spatially shifted) version of itself is referred to as *temporal coherence*; whereas *spatial coherence* refers to a light beam's ability to interfere with a spatially shifted (but not delayed) version of itself. This form of light division is referred to as *wavefront splitting*.

By investigating the interference of lightwaves in an interferometer, which was initially proposed by Michelson, the idea of *temporal coherence* can be defined and characterized more clearly [44].

### 3.2.1 The Michelson interferometer

Michelson demonstrated that the intensity of the light incident on the detector is determined by the light interference from the two arms of the interferometer, shown in Figure 3-2. As the mirror moves, the striking light on the detector shifted from constructive to destructive interference and back again. The area between the fringes is illuminated by a  $\bar{\lambda}/2$

( $\bar{\lambda}$  is the pathlength difference between two arms). Figure 3-3 depicts a typical interference pattern, with intensity plotted against mirror displacement  $h$  from the position of equal pathlengths. An *interferogram* is a depiction of intensity vs. pathlength differential [44].

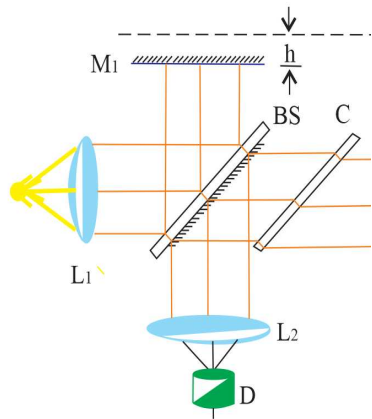


Figure 3-2 The Michelson interferometer, including the point source  $S$ , the lenses  $L_1$  and  $L_2$ , moveable mirrors  $M_1$ , fixed mirror  $M$ , beam splitter  $BS$ , compensator  $C$ , and detector  $D$ .  $h$  is the mirror displacement of  $M_1$ . Adapted from [44].

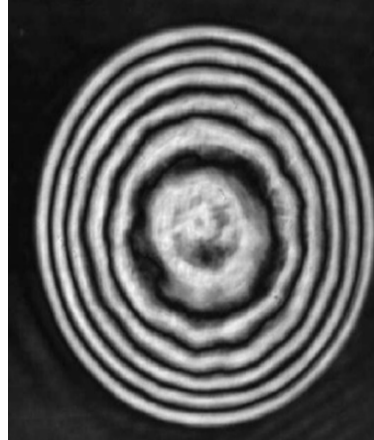


Figure 3-3 bright fringe in the coherent regime (interferogram pattern). Adapted from [44].

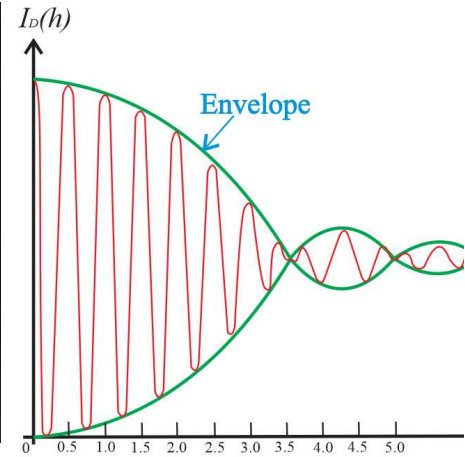


Figure 3-4 Intensity incident on the detector  $D$  versus normalized mirror displacement  $h/\bar{\lambda}$ , where  $\bar{\lambda}$  is the mean wavelength. The envelope of the fringe pattern is drawn dotted. Adapted from [44].

Linewidth and coherence time are the most important parameters in spectral measurements and that can be compared to evaluate the coherence regime the interferometer operates in. The parameters are inversely related, and the degree of temporal coherence of the signals in the interferometer is used to compute the relation between them.

The electric field functions  $E(t)$  and  $E(t + \tau)$  are entirely correlated or coherent if they have the same amplitude and initial phase after the time interval [44]. As a result, during this time interval, the two components of the field emitted by the laser at different times can stably interfere [24, 44]. The maximum time that the correlation can be maintained is known as the coherence time and provided by [22, 44],

$$\tau_c \propto 1/\Delta\nu \quad 3.8$$

The autocorrelation function of the light wave plays an important role in determining the composed intensity observed by the photodetector. The autocorrelation function of the light wave provides insight into the temporal properties of the wave, such as its coherence time,

pulse duration, and spectral bandwidth. These properties are incredibly important for understanding the wave's behavior, as they determine how the wave interacts with its environment. It is given by [44]:

$$I_E(\tau) = \varepsilon_0 c n \langle (E_1(t) + E_2(t + \tau))(E_1(t) + E_2(t + \tau))^* \rangle \quad 3.9$$

where  $I_E(\tau)$  is the intensity composition of the parallel electric field vectors.  $k_1, k_2$  are coupling factors in each path,  $E(t)$  is electric field function, and  $E_1(t) = \sqrt{k_1}E(t)$  and  $E_2(t) = \sqrt{k_2}E(t)$

The intensities with  $\tau = 0$ , given by the time averages are [44]:

$$I_1 = \varepsilon_0 c n \langle |E_1(t)|^2 \rangle \text{ and } I_2 = \varepsilon_0 c n \langle |E_2(t)|^2 \rangle \quad 3.10$$

The *mutual correlation* or *coherence function*, is defined [44] as

$$\Gamma_{12}(\tau) = \langle E_1(t)E_2^*(t + \tau) \rangle \quad 3.11$$

and the *self-correlation*:

$$\Gamma_{11}(\tau) = \langle E_1(t)E_1^*(t + \tau) \rangle \quad 3.12$$

In many cases, it is convenient to work with a normalized version of the *self-coherence* function, rather than the self-coherence function itself. Noting that  $I_0 = \Gamma_0$  for  $\tau = 0$ , the normalization is given by [44]:

$$\gamma(\tau) = \frac{\Gamma(\tau)}{\Gamma(0)} \quad 3.13$$

The normalization of the *mutual* and *self-coherence* function, denoted by the symbol, and they are known as the *complex degree of coherence* and the *degree of complex self-correlation* respectively. The complex degree of coherence [44] is,

$$\bar{\gamma}_{12}(\tau) = \frac{\Gamma_{12}(\tau)}{\sqrt{\Gamma_{11}(0)\Gamma_{22}(0)}} \quad 3.14$$

and the degree of *complex self-correlation*:

$$\bar{\gamma}_{11}(\tau) = \bar{\gamma}(\tau) = \frac{\Gamma_{11}(\tau)}{\Gamma_{11}(0)} \quad 3.15$$

The depth of the fringes observed at any path length difference  $h$  can be precisely specified by utilizing the concept of fringe visibility which was first introduced by Michelson. A sinusoidal fringe pattern's visibility is determined by [44]:

$$V(\tau) = \frac{2\sqrt{I_1 I_2} |\bar{\gamma}(\tau)|}{I_1 + I_2} \quad 3.16$$

for the condition of self-coherence,  $I_1 = I_2$ , visibility remains and

$$V(\tau) = |\bar{\gamma}(\tau)| \quad 3.17$$

The concept of temporal coherence is related to the ability of two light beams with relative delay to form interference fringes, as seen on Michelson's interferometer. For  $|\bar{\gamma}(\tau)| = 1$  coherence is complete,  $0 < |\bar{\gamma}(\tau)| < 1$  is for partial coherence, and  $|\bar{\gamma}(\tau)| = 0$  means complete incoherence.

The coherence time: is an average value of the time interval between the phase variations of the electric field and is defined as [44]:

$$\tau_c \equiv \int_{-\infty}^{\infty} |\bar{\gamma}(\tau)|^2 d\tau \quad 3.18$$

From this definition, the coherence time can be related to the linewidth of the power density spectrum. For the definition to make sense, the coherence time must have the same order of magnitude as the inverse of the linewidth, i.e.  $\tau_c \approx 1/\Delta\nu$  [44].

When measuring the linewidth using the interferometric method, the signals in the two arms of the interferometer must have no correlation, indicating that they are in the incoherent regime. To satisfy this condition, this relation  $|\tau_{DL}| \gg \tau_c$  must exist between the arms of the interferometer. In the case of  $|\tau_{DL}| \ll \tau_c$ , the intensity of light primary product an interference pattern, and the interferometer operates in a coherent regime. On other hand in the coherent regime between two quasi-monochromatic signals an *interferogram* is obtained by the intensity variation  $I_D(h)$  as a function of the difference in paths  $h/\bar{\lambda}$ , shown in Figure 3-2. The average delay time is  $\tau_{DL} = 2(h/\bar{\lambda}v)$ , with  $\bar{\lambda}$  average wavelength,  $c$  signal propagation speed,  $h$  difference between the paths traveled by the waves in the two branches of the interferometer and  $\nu$  the frequency of the signal [44].

From the definition (3.18),  $\tau_c = \sqrt{2 \ln 2 / \pi} (1 / \Delta \nu_d) \operatorname{erf} [\pi \Delta \nu_d \tau / \sqrt{\ln 2}]$  which, at the limits of integration, results in the relationship between coherence time and Gaussian linewidth [44]:

$$\tau_c = \sqrt{\frac{2 \ln 2}{\pi}} \frac{1}{\Delta \nu_d} = \frac{0.664}{\Delta \nu_d} \quad 3.19$$

The relationship between coherence time and Lorentzian linewidth is [44]:

$$\tau_c = \frac{1}{\pi \Delta \nu} = \frac{0.318}{\Delta \nu_d} \quad 3.20$$

For the rectangular line, the relationship is [44]:

$$\tau_c = \frac{1}{\Delta \nu} \quad 3.21$$

### 3.3 Self-Homodyne configuration

There are several techniques for measuring the laser linewidth, using the optical spectral analysis as well as converting the frequency fluctuation into intensity fluctuation [10]. Since the frequencies of the laser linewidth are too high to be measured by conventional electronics, some different techniques were developed to implement the linewidth measurement [35].

For single-frequency lasers, the self-homodyne technique uses the record of beating notes between the laser output and a delayed part of it. Thanks to newly designed laser devices with improved coherence properties, the linewidth in the sub-kilohertz range has emerged commercially. A new challenge is so presented by the sub-kilohertz or ultra-narrow linewidth lasers, due to the fact that the traditional self-homodyne or self-heterodyne techniques necessitate long lengths of delaying fiber and are therefore impractical due to the propagation losses [9, 10]. The narrower linewidth needs the longer length of delaying fiber for better Resolution measurement [6].

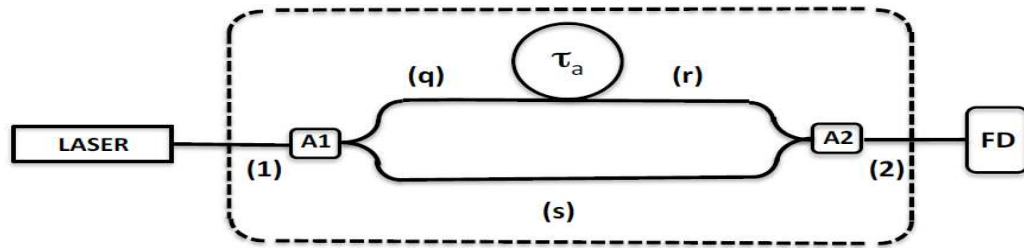


Figure 3-5 Schematic diagram of the interferometer: Laser (semiconductor); A1 and A2 directional couplers;  $\tau_a$  the delay linewidth fiber optic coil; FD photodetector.

The homodyne and heterodyne techniques are the most established ones for measuring the linewidth of a laser. In the to be recorded technique, by mixing the input optical signal with a local oscillator, in the so-called coherent detection, the original optical signal is down converted to the RF domain. The requirement of a local oscillator is eliminated by using the self-homodyne detection: the optical signal combines with a delayed version of itself. The self-homodyne detection set-up is shown at Figure 3-5, where a Mach-Zander configuration is formed by connecting two directional couplers, A1 and A2, by two delay lines [6, 19].

The self-homodyne technique is an interferometric method to measure the linewidth from the power spectrum density (PSD) of the electric field, which is obtained as a result of the beating between the optical signal and a delayed portion of it. The phase fluctuation,  $\phi(t)$ , of the obtained beating signal is retrieved as a variation in intensity of the photocurrent produced in the non-linear detector, and further transformed into power spectral density by a spectrum analyzer. In this interferometer, with one arm much longer than the other, the imbalance causes the relative delay  $\tau_{DL}$ , which is a necessary condition. In this condition, the coherence time,  $\tau_{DL} \gg \tau_c$  is required for the signals to be de-correlated. In this case, in which there is no correlation between the direct and delayed signals, the spectrum measured after the detection of the signals is due to the phase noise. The linewidth is calculated from the power spectral density at -6 dB from top which is obtained by the Fourier transform of the auto-correlation function.

### 3.3.1 Analysis of the Self-Homodyne technique

The process of converting phase noise to intensity noise in the interferometer allows the analysis of the laser spectrum by the current of the photodetector. In Figure 3-5, the scheme of the measurement system has the laser generator, which couples the light by optical fiber to the port (1) of the directional coupler A1. The signal is divided into two paths, according to the power coupling coefficient between the input and each output, proportional to  $k_1$  and  $(1 - k_1)$ . The electric field generated by the laser at the port (1) of directional coupler A1 at Figure 3-5, is:

$$E(t) = [A_0 + \delta(t)] \exp [j(\omega_m t + \phi(t))] \quad 3.22$$

where  $\phi(t)$  is the phase fluctuation and the amplitude fluctuations defined by  $\delta(t)$ ,  $\omega_m$  is the average angular frequency of the optical signal;  $E(t)$  is electric field generated by the laser, at the point (1) (Figure 3-5). The electrical field at the photodetector  $E_D(t)$  at port (2) is resulting from the scalar of the fields after propagating in each arm, considering that the optical polarization of the two arms are the same. The electrical field at port (2) is found after the directional coupler A2; the power coupling factors  $k_1$  and  $k_2$  are related to couplers A1 and A2 respectively. The electrical field at the photodetector is given by :

$$E_D(t) = E_{(r)} + E_{(s)} = \sqrt{k_1 k_2} E(t) + \sqrt{1 - k_1} \sqrt{1 - k_2} E(t) \quad 3.23$$

$E_D(t)$  is the electrical field at the photodetector. The electrical field,  $E_D(t)$ , is proportionate to the incident light power at the photodetector and, consequently, the current that flows through the photodetector. As a result, the current that flows through the photodetector is directly proportional to the incident light power at the photodetector.

In the upper arm, the signal has a temporal delay,  $\tau_d$ , due to travelling through the optical spool  $B$ :

$$\tau_{DL} = nL/c \quad 3.24$$

where  $L$  is the length of the optical spool,  $c$  is the light speed and  $n$  is the refractive index of fiber (for  $\text{SiO}_2 \approx 1.5$ ).

With the saturated oscillator, the amplitude fluctuation is  $\delta(t) \approx 0$  and from the Eq (3.22), the electric field after the spool is:

$$E_{(r)}(t) = A_0 \exp [j(\omega_m(t - \tau_{DL}) + \phi(t - \tau_{DL}))] \quad 3.25$$

The resulting field at port (2) on the FD photodetector is:

$$E_D(t) = A_0 \left\{ \sqrt{k_1 k_2} e^{j[(\omega_m(t-\tau_{DL})+\phi(t-\tau_{DL}))]} + \sqrt{(1-k_1)(1-k_2)} e^{j[(\omega_m(t)+\phi(t))]} \right\} \quad 3.26$$

The output current in the photodetector is proportional to the power density of the electric field, it has the continuous and variable components:

$$\tilde{i}_D = I_{CC} + i_D = (\rho^* A/2\eta) E_D E_D^* = (\rho^* A/2\eta) |E_D|^2 \quad 3.27$$

where  $\rho^*$  is the responsiveness,  $\eta$  the characteristic impedance of the medium and  $A$  the detector area.  $\tilde{i}_D$  is the output current in the photodetector,  $i_D$  is the variable current, and the direct current is equal to  $I_{CC} = K_{CC} A_0^2 (\rho^* A/2\eta)$ .

The detected field  $E_D \cdot E_D^*$ , calculated by:

$$|E_D|^2 = A_0^2 \left\{ K_{CC} + K_D [e^{-j[\omega_m \tau_{DL} + \phi(t) - \phi(t - \tau_{DL})]}]_{+} e^{j[\omega_m \tau_{DL} + \phi(t) - \phi(t - \tau_{DL})]} \right\} \quad 3.28$$

where  $K_{CC} = k_1 k_2 + (1 - k_1)(1 - k_2)$  and  $K_D = \sqrt{k_1 k_2 (1 - k_1)(1 - k_2)}$ .

By Replacing Eq (3.28) with Eq (3.27), due to the interfering term, we have,

$$i_D(t) = 2K_D (\rho^* A/2\eta) A_0^2 \text{Re} \left\{ e^{j[\omega_m \tau_{DL} + \phi(t) - \phi(t - \tau_{DL})]} \right\} \quad 3.29$$

$$i_D(t) = k_D A_0^2 \cos [\omega_m \tau_{DL} + \Delta\phi(t)] \quad 3.30$$

where  $k_D = 2K_D (\rho^* A/2\eta)$  with the unit of  $[k_D] = A \cdot m^2/V^2$ , and  $\Delta\phi(t) = \phi(t) - \phi(t - \tau_{DL})$

### 3.4 The effect of external factors when using the self-homodyne technique

Internal and external factors may cause intensity and phase noise in lasers, and the impact of these influences is heavily influenced by the internal dynamics [45]. As mentioned before (section 5.1.1) the electrical noise in the laser bias current impacts the operation, leading to further optical fluctuations. The noisier the bias current, the noisier the laser diode photon stream, and thus the frequency and amplitude noises rise up, causing the laser linewidth's enlargement [46, 47].

Acoustic noise, mechanical vibrations and thermal variations are other external impact factors, which are also known as technical noise. The sources of technical noise usually result in a Gaussian profile in the laser spectrum [40]. Technical noise affects the linewidth of a laser, as well as the measurements by which a signal travels through an optical fiber [9, 40].

### 3.4.1 Influence of exterior acoustic noise on linewidth laser measurements

In previous [9], it was shown that the apparent spectral linewidth is enlarged due to the mechanical noises, such as vibrations and acoustic waves, when the optical wave is detected after propagation in an optical fiber. In that work, a self-homodyne optical fiber Mach-Zehnder interferometer (UMZI) in a vacuum controlled chamber was used to measure the spectral linewidth of a HeNe laser [9]. Placing the UMZI inside a vacuum chamber can cancel the impact of acoustic waves over the long fiber arm. Changing the internal chamber air pressure changes the sound wave's intensity. As a result, the contribution of phase noise intensity over the UMZI long arm can also be controlled. With the change in air chamber pressure, the results revealed an apparent broadening of the highly coherent laser linewidth from a few hertz to the kilohertz range, confirming that acousto-optic effects on the interferometer optical fiber were influencing the results [9, 40]. In fact, technical noises, such as external acoustic waves can broaden the linewidth due to the interaction of light and phonons in silica, and as a result the propagating laser beam is subjected to additional phase noise over the fiber in the longer arm of the UMZI, as in Figure 3-6 [9].

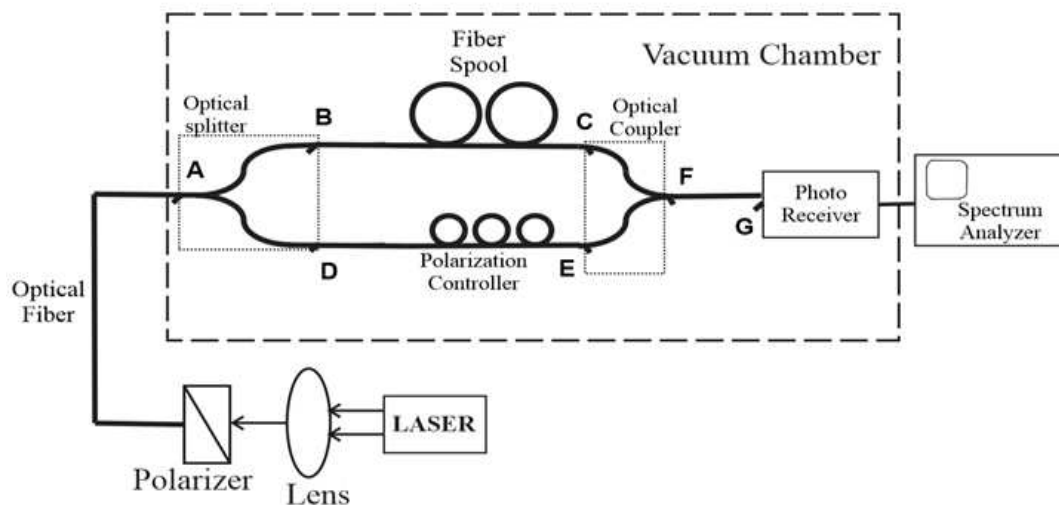


Figure 3-6 Experimental setup shows the interferometer in vacuum chamber. Adapted from [9].

Even though the lengthier arm in that experiment was not lengthy enough to establish the UMZI to the uncorrelated situation, the experimental linewidth broadening exhibits a good Lorentzian fitting. The initial linewidth is assumed to have been widened by the arbitrary light

phase modulation on the lengthier arm brought on by external acoustic waves, which brings the interferometer into a quasi-coherent regime. [9].

The estimated laser linewidth derived from the spectrum of the output signal from the UMZI photodetected can be artificially widened by the acoustic contribution, which can cause phase modulation during light transmission across the interferometer's long arm. The interferometer would initially enter the coherent regime due to the relationship between long arm time delay and laser bandwidth, however the spectrum measured in the study range (Hz to kilohertz) did not exhibit the anticipated flatness. Nevertheless, according to a non-coherent regime, the results from measured spectra showed good correlation with the Lorentzian linewidth approximation. In fact, the interferometer is set up to operate in a quasi-coherent regime thanks to the acoustic waves' chaotic effects on the lengthier arm of the light phase shift. In accordance with observations made while being subjected to external acoustic noise, the modeling results of a fiber UMZI considering acoustically induced fiber phase harmonic modulation have demonstrated that the UMZI output spectrum is widened by external modulating frequencies.

### 3.5 Measurement Method for Narrow-Linewidth Lasers

For linewidth measurement, two methods are commonly used: the first is to directly calculate the laser linewidth using the laser's power spectrum density (PSD), and the second is to determine the linewidth indirectly based on the relation between phase noise and linewidth. To obtain the PSD, optical beat notes are required. The combined output of two incoherent lasers, each with a Lorentzian line shape, retains that shape and the PSD of the beat notes can be represented as [20]:

$$s(\nu) = \frac{\Delta\nu}{2\pi[(\nu - \nu_b)^2 + (\Delta\nu/2)^2]} \quad 3.31$$

where  $\Delta\nu = \nu_t + \nu_r$ ,  $\nu_t$  is the linewidth of the tested laser,  $\nu_r$  is the linewidth of the reference laser and  $\nu_b$  is the difference in the output frequencies of the two previously described lasers it is also known as the center frequency of the beat notes. The beat signal's linewidth is the summation of the widths of the two lasers involved in the beating and being these two lasers with the same or comparable frequencies to interact and generate a lower frequency, beat signal. As illustrated in Figure 3-7, there are often two cases of beat notes that are appropriate for linewidth measurement. In case 1, the tested linewidth and the reference linewidth are

equal,  $v_t = v_r$ , in this case the linewidth of the beat notes is twice that of the tested laser,  $\Delta v = 2v_t$ . However, in the case 2, the linewidth of the reference laser is quite narrow, and it can be ignored when compared to the tested laser ( $v_t \gg v_r$ ), As a result, the linewidth of the beat signal is approximately equivalent to the linewidth of the tested laser,  $\Delta v \approx v_t$ . In this section, the focus is on the delayed self-homodyne interferometric structure is shown in Figure 3-6, and the measurement principle is based on case 1 [20]. Case 1 applies because the self-homodyne technique makes use of the beating note between the laser output and a delayed portion of it,  $\Delta v = v_t$ .

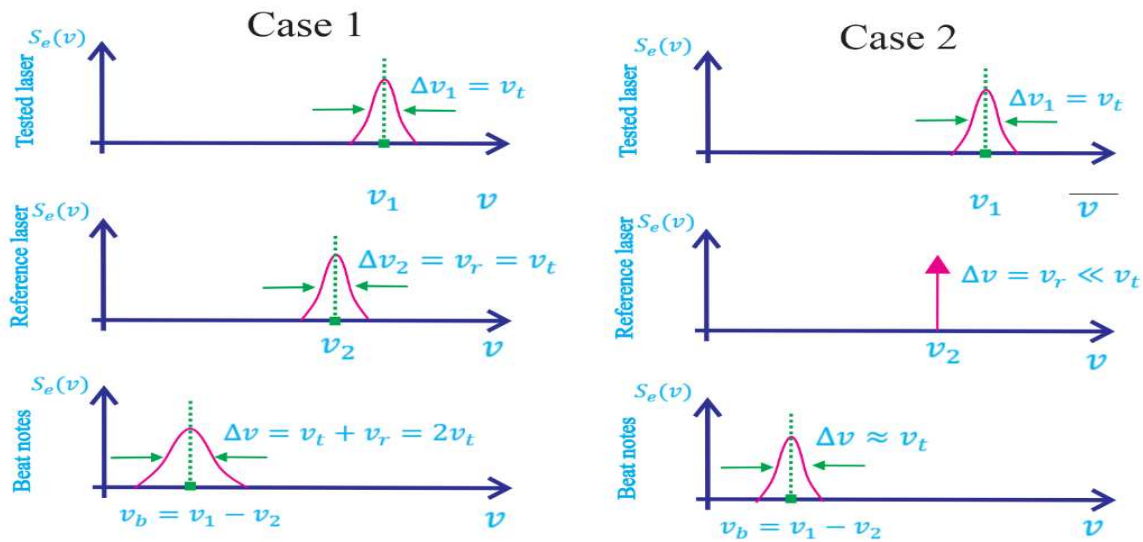


Figure 3-7 The optical beat note principle. Adapted from [20]

### 3.6 Experimental methodology for UMZI

The UMZI has the advantages of using a simple structure, of having a large measuring range and minimal optical transmission loss the beating note [20]. However, because the beating notes center frequency  $v_b$  is around 0 Hz with 100 Hz tolerance, any low-frequency noise in the environment may interfere in the measurement results. Given the sensing characteristics of the optical fiber, environmental noise, temperature, pressure, among other factors can have a significant impact over the test results [9, 20].

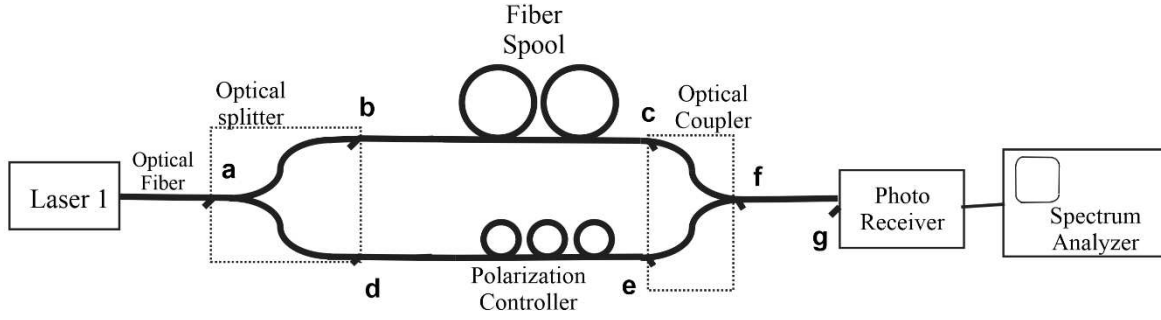


Figure 3-8 Typical experimental set-up for linewidth measurement using self-homodyne method.

Assuming that the Mach-Zehnder interferometer has a delay line (DL) with a propagation time  $\tau_{DL}$  and a laser with a coherence time  $\tau_c$ , then the MZI operation regime is defined by the relationship between the DL time and the laser coherence time [6]. In the case of  $\tau_{DL} \gg \tau_c$  the two MZI arms signals lose phase coherence, this is referred to as a non-coherent regime. In this condition, the laser power spectrum density (PSD) represented as [6, 38]:

$$S_\phi = \frac{k}{|\omega|} + S_0 \quad 3.32$$

where  $S_\phi$  is the photo detected PSD,  $\frac{k}{|\omega|}$  is the  $1/f$  noise (Gaussian lineshape) and  $S_0$  is the PSD white noise (Lorentzian lineshape).  $S_0$  and  $k$  are represented in units of  $(\text{rd/s})^2/\text{Hz}$  and  $(\text{rd/s})^3/\text{Hz}$ , respectively. The conversion factors for  $S_0$  and  $k$  to convert from measured values to the units used in the equations,  $(2\pi)^2/2$  and  $(2\pi)^3/2$  are applied, respectively [38].

According to Schawlow–Townes equation which represented in equation (3.33) for measuring the laser linewidth [6, 9, 48]

$$\Delta\nu_{laser} = \frac{4\pi h\nu(\Delta\nu_c)^2}{P_{out}} \quad 3.33$$

in which  $\Delta\nu_{laser}$  denotes the conceptual linewidth of the laser,  $P_{out}$  denotes the laser's output power,  $h\nu$  denotes the energy of the photons released,  $\nu$  denotes the laser's optical center of emission frequency (assumed to be quasi-monochromatic),  $h$  denotes the plank constant, and  $\Delta\nu_c$  denotes the resonator cavity bandwidth. Here, we only take into consideration monomode lasers with a Lorentzian spectrum [34, 35]. Consequently, the laser Lorentzian linewidth,  $\Delta\nu_L$  is given by:

$$\Delta\nu_L \approx \frac{1}{\tau_c} \quad 3.34$$

Equation (3.32) is rewritten as follows [6]:

$$S_\phi \approx S_F \cdot e^{-\ln 2 \cdot \left(\frac{\Delta f}{\Delta\nu_F}\right)^2} + S_L \cdot \frac{1}{1 + \left(\frac{\Delta f}{\Delta\nu_L}\right)^2} \quad 3.35$$

$$S_{LFN} = S_F \cdot e^{-\ln 2 \cdot \left(\frac{\Delta f}{\Delta\nu_F}\right)^2} + S_{FIAN} \quad 3.36$$

### 3.6.1 Experimental setup

In the configuration, shown in Figure 3-8, the optical carrier from the tested laser (a) is split into two paths by a 50:50 beam splitter: paths 'b-c' and 'd-e'. So, the optical carrier at point, 'c', is delayed by a time interval when compared with the other path end, 'e'. The longer arm has an optical standard fiber spool ('b-c', from 60 m up to 100 km length was used here) which is much longer than the other, short direct arm 'd-e' (~1 m); therefore, the time delay  $\tau_{DL}$  is from 0.2  $\mu\text{s}$  to 333  $\mu\text{s}$ . Thus, the optical signals in the two MZI arms might lose phase coherence if  $\tau_{DL}/\tau_c \gg 1$  condition is obtained: the so-called non-coherent regime. The short arm has an adjustable optical polarization control (PC) that provides polarization matching for the two wavefronts before combining at point 'f'. However, the state of polarization (SOP) may drift randomly due to the fiber birefringence effect and cannot be fully controlled by PC, resulting in some instability in the detected self-heterodyne spectrum and so in linewidth measurement errors. When the two optical paths combine by a second 50:50 coupler, and carriers mixed at point 'f', after the proper polarization optimization and further coupled to a photoreceiver. The photocurrent is measured by an Electrical Spectrum Analyzer (ESA, HP3561A) and the signal power spectrum density is obtained by the Fourier transform of the signal autocorrelation function. The electrical spectrum analyzer was connected to a computer by USB/GPIB interface (Agilent Technologies; 82357B) and the data was acquired by software (HP7470A plotter emulator).

Table 3-1 The lasers used in this experiment

Laser model	Cavity type	Linewidth	wavelength	Power range examined
Santec	External Cavity with filters	1 MHz	1560 nm	-10 dBm to +10 dBm

Photonetics	External Cavity with digital grating	200 kHz	1500 nm	-8 dBm to 2 dBm
RIO laser 1	Integrated External Cavity	5 kHz	1550 nm	-10 dBm to +10 dBm
RIO laser 2	Integrated External Cavity	5 kHz	1550 nm	-10 dBm to +10 dBm

The two types of spectrum analyzers for electrical signals are the conventional RF or microwave spectrum analyzer and the FFT analyzer (used in this experiment). As technology advances, more digital technology is incorporated into RF or microwave devices, and the difference between them narrows [31].

A super heterodyne recipient with a wide - ranging frequency and a power detector is used in RF or microwave devices. In order for the medium (IF) filter to react stationarily, the sweep signal needs to be slow enough. The absolute magnitude being evaluated by this device is the energy  $P$ , which is assessed in (W), and is the power diffused by the impedance  $R_0$  in the bandwidth  $B$  centering on the frequency,  $\nu$ . The IF filtration, which can be chosen via the front screen, determines the bandwidth  $B$ . [31].

For FFT analyzers the spectrum is calculated from a digitized time series of the input signal by using [31]:

$$S(f) = \frac{2}{T} |X_T(f)|^2, \quad f > 0 \quad 3.37$$

As a result, a fast Fourier transform (FTT) is used instead of the Fourier transform. For a given time  $T$  and number of samples in the time series, hard truncation of the input signal offers the maximum frequency resolution. Due to the Fourier transform of the rectangular pulses, the corresponding filter has high secondary lobes, which is an issue found in hard truncation. As a result, the signal (or noise) from other portions of the spectrum contaminates each frequency slot: "frequency leaking" is the term used for this phenomenon. Therefore, hard truncation is replaced by a weight function, which is referred to as a window, to reduce such "leakage". The most well-known of these features are the Parzen window, the Bartlett (rectangle shaped), and the Hanning (cosine) windows. A flat-top window results from the measurement period being sharply truncated. A exchange between precision and frequency leakages, which is dependent on the particular spectrum, leads to the selection of the best

window function. Even though the spectrum is shown on a log scale, the FFT is essentially linear in both frequency and amplitude. The FFT method's bandwidth  $B$  is determined by the frequency range and the quantity of coordinates used. [31].

Without losing accuracy in the conversion, the measured spectrum can be shown in two ways, as described below.

1. *Power spectral density*  $(f) = (2/T)|X_T(f)|^2 (V^2/Hz)$ . This option provides a clear depiction of the noise. A horizontal line with a value of  $N$  is used to represent white noise with a power spectral density of  $N (V^2/Hz)$ . In contrast, a sheer sinusoid with magnitude  $V_{rms}$  and frequency  $f_0$  manifests as a (slim) lorentzian-like distribution of width  $B$  with frequency  $f_0$  as its center. The peak is equal to  $V_{rms}^2/B$ , and the instrument's internal algorithm determines the distribution's true shape. [31].
2. *Power spectrum*  $(1/T)S(f) = (2/T^2)|X_T(f)|^2 (V^2)$ . The spectrum is shown similarly to how it would appear in an RF spectrum analyzer, with the small exception that power is given in  $V^2$  rather than  $W$ . Except where otherwise stated, the input impedance is taken to be  $50 \Omega$ . As a result, a sine wave signal with amplitude  $V$  rms is represented as a distribution with width  $B$  and altitude  $V_{rms}^2$ , and white noise with power spectral density  $N (V^2/Hz)$  is represented as a line graph at  $V_{rms}^2 = NB$ . [31].

### 3.6.2 Linewidth measurement

Figure 3-9 depicts an example of the acquired signal. The graphic on the left depicts a noisy signal that can be approximated by a Lorentzian using

$$PSD_{\frac{V}{\sqrt{Hz}}}(f) = \frac{\alpha}{\pi} \cdot \frac{\frac{\Delta v}{2}}{f^2 + \frac{\Delta v^2}{4}} \quad 3.38$$

where  $\Delta v$  is the Lorentzian linewidth at -6dB,  $f$  is the frequency, and  $\alpha$  is a constant that adjusts the amplitude, for simplicity  $\alpha/\pi = \gamma$ . The experimental data acquired by the spectrum is initially in single sideband format (SSB). The spectrum analyzer detects electrical signals and converts all to dBV (dB volts). This voltage is proportional to the electrical current ( $V = RI$ , where  $R$  is the 50-ohm impedance of the analyzer) and the electrical current is proportional to optical power.

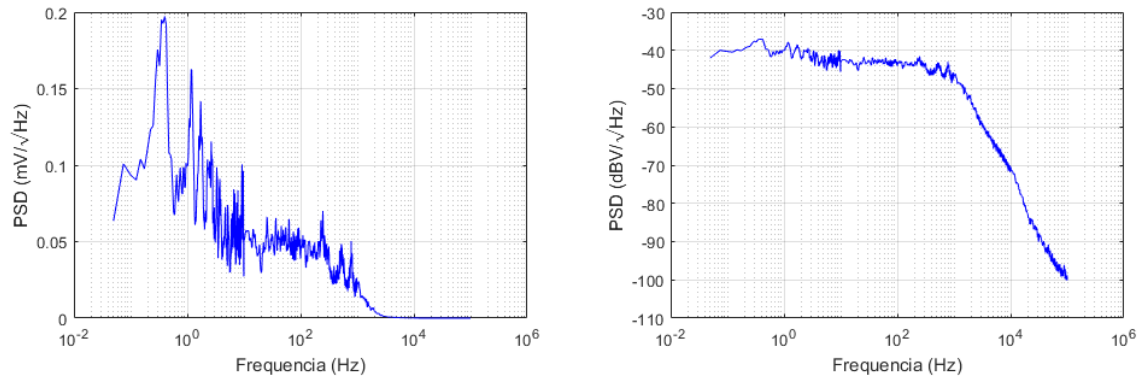


Figure 3-9 Experimental curves in  $\text{mV}/\sqrt{\text{Hz}}$  (left image) and  $\text{dBV}/\sqrt{\text{Hz}}$  (right image).

In this experiment, the results obtained by the Electrical Spectrum Analyzer (ESA, HP3561A) gives the noise Power Spectral Density (PSD) in  $\text{dBV}/\sqrt{\text{Hz}}$  versus frequency in Hz, this referred to as  $\text{PSD}_{\text{dBV}/\sqrt{\text{Hz}}}$  or PSD in volts which is shown in Figure 3-9. Because the optical power proportionally generates a current in the photodetector, the amplified photodetector will provide a voltage proportional to the optical power. An operational amplifier enhances this current, resulting in a signal that is proportional to the laser power when it reaches the Spectrum Analyzer.

To compute the PSD in  $\frac{W}{\text{Hz}}$  and subsequently in  $\frac{\text{dBW}}{\text{Hz}}$ , we need first determine the relationship between  $\frac{\text{dBV}}{\sqrt{\text{Hz}}}$  (experimental measurement unit) and  $\frac{V}{\sqrt{\text{Hz}}}$ , after which we can convert  $\frac{\text{dBV}}{\sqrt{\text{Hz}}}$  to  $\frac{\text{dBW}}{\text{Hz}}$ . Equation 3.39 illustrates this relationship.

$$\text{PSD}_{\frac{\text{dBV}}{\sqrt{\text{Hz}}}}(f) = 20 \cdot \log_{10} \left( \text{PSD}_{\frac{V}{\sqrt{\text{Hz}}}}(f) \right) \quad 3.39$$

The link between the units  $W/\text{Hz}$  and  $V^2/\text{Hz}$  can then be defined as:  $k$  is a constant.

$$\text{PSD}_{\frac{W}{\text{Hz}}}(f) = k \cdot \text{PSD}_{\frac{V^2}{\text{Hz}}}(f) \quad 3.40$$

To get the PSD in  $\frac{V^2}{\text{Hz}}$  we need to square  $\frac{V}{\sqrt{\text{Hz}}}$  to remove the square root, therefore we have

$$\text{PSD}_{\frac{V^2}{\text{Hz}}}(f) = \left( \text{PSD}_{\frac{V}{\sqrt{\text{Hz}}}}(f) \right)^2 \quad 3.41$$

Then from equation 3.39 we have

$$PSD_{\frac{V^2}{Hz}}(f) = \left( 10^{\frac{PSD_{dBV}(f)}{20 \cdot \sqrt{Hz}}} \right)^2 \quad 3.42$$

By substituting equation 3.42 in equation 3.40 we have the PSD in  $\frac{W}{Hz}$  as define in equation 3.43.

$$PSD_{\frac{W}{Hz}}(f) = k \cdot 10^{\frac{PSD_{dBV}(f)}{\sqrt{Hz}}} \quad 3.43$$

The PSD in  $\frac{dBW}{Hz}$  can thus be shown in equation 3.44.

$$\begin{aligned} PSD_{\frac{dBW}{Hz}}(f) &= 10 \cdot \log_{10} \left( k \cdot 10^{\frac{PSD_{dBV}(f)}{\sqrt{Hz}}} \right) \quad 3.44 \\ &= 10 \cdot \log_{10}(k) + 10 \cdot \log_{10} \left( 10^{\frac{PSD_{dBV}(f)}{\sqrt{Hz}}} \right) = k_m + PSD_{\frac{dBV}{\sqrt{Hz}}}(f) \end{aligned}$$

This equation can be used to convert the Power Spectral Density (PSD) in  $\frac{dBV}{\sqrt{Hz}}$  to the Power Spectral Density (PSD) in  $\frac{dBW}{Hz}$ . Where  $k_m$  is a constant. The value of  $k$  can be determined from equation 3.46. Given that the optical power  $P$  is known, the discrete integration of the function  $PSD_{\frac{dBW}{Hz}}(f)$  can be calculated by equation:

$$P = \sum_{i=1}^n \Delta f(i) \cdot \overline{PSD_{\frac{W}{Hz}}}(i) = \sum_{i=1}^n \Delta f(i) \cdot k \cdot 10^{\frac{\overline{PSD_{dBV}}(i)}{\sqrt{Hz}}} = k \cdot \sum_{i=1}^n \Delta f(i) \cdot 10^{\frac{\overline{PSD_{dBV}}(i)}{\sqrt{Hz}}} \quad 3.45$$

And then  $k$  can be obtained by equation:

$$k = \frac{P}{\sum_{i=1}^n \Delta f(i) \cdot 10^{\frac{\overline{PSD_{dBV}}(i)}{\sqrt{Hz}}}} \quad 3.46$$

where  $f(k)$  and  $f(k+1)$  are the two adjacent frequencies and  $\Delta f(i)$  is the  $i$ -th term of  $\Delta f$  vector, corresponding to the frequency spacing between these two points,  $PSD_{\frac{dBV}{\sqrt{Hz}}}(k)$  and

$PSD_{\frac{dBV}{\sqrt{Hz}}}(k+1)$  are the two neighboring points in power and  $\overline{PSD_{\frac{dBV}{\sqrt{Hz}}}}(i)$  is the  $i$ -th term of the

$\overline{PSD_{dBV}}(i)$  vector, corresponding to the average amplitude of these two subsequent points.

Figure 3-10 illustrates the integration process.

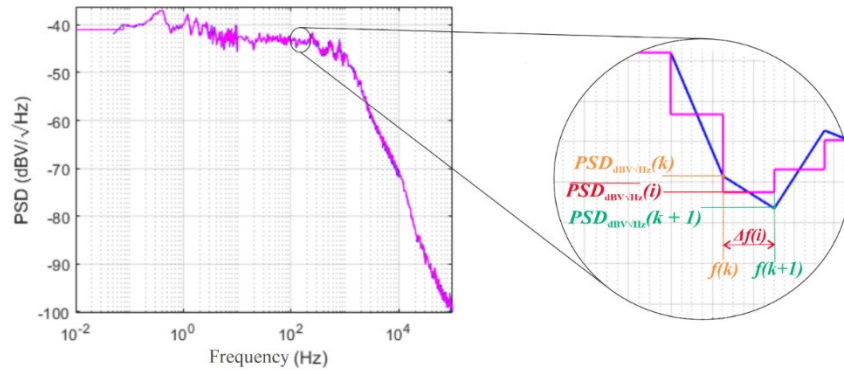


Figure 3-10 Details about the discrete integration process. And Experimental curves dBV/√Hz (right image)

## 4 Results and discussions

The optical power measured at each location in the experimental setup is shown in Figure 4-1. The short MZI arm has a power loss of 1.0 dB and the lengthy MZI arm (30 km) has a power losses of 7.5 dB (standard 0.25 dB/km fiber reel plus isolator 0.4 dB and connectors 0.6 dB) (isolator 0.4 dB, connectors 0.6 dB).

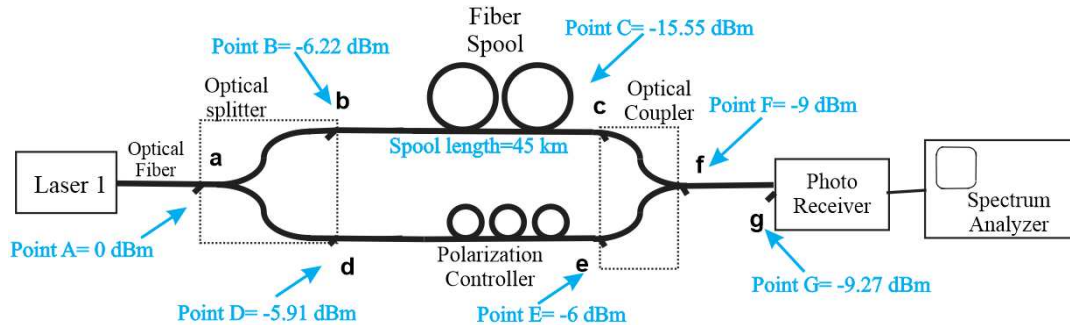


Figure 4-1 Self-Homodyne linewidth measurement setup, shows the optical power at each point.

### 4.1 The effects of polarization control adjustment, laser power and the optical fiber length on the PSD measurement

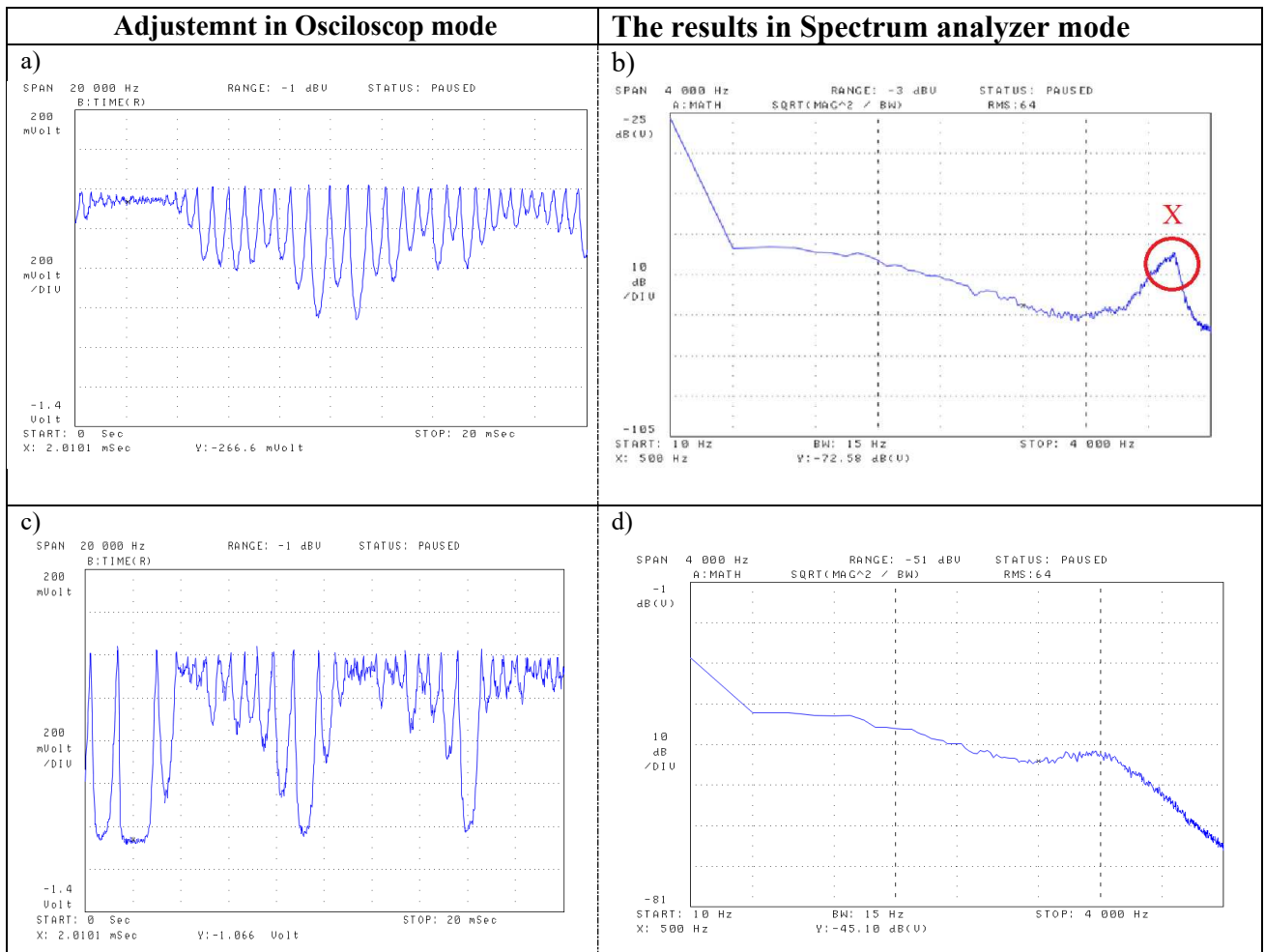
This section discusses and presents the impacts of polarization control adjustment, laser power and optical fiber length on the PSD. The section will use graphs to demonstrate the relationship between these three variable factors and the obtained PSD.

#### 4.1.1 The effect of Optical Polarization Control on PSD data

On practical situations, many beat frequency signals are observed due to fluctuations in the laser wavelength. To measure the low frequency range, one requires a long delay fiber, typically more than 10 km. However, the accuracy of the linewidth measurements are influenced by several aspects such as the noise due to the laser bias source, the polarization mismatch, the  $1/f$  frequency noise intensity, the Stimulated Brillouin scattering (SBS) effect and also environmental factors such as temperature and vibration [6].

To obtain the best possible mixed signal and ultimately the maximum power in the spectrum analyzer, the optical polarization controller must be carefully adjusted, using time-domain analysis (oscilloscope mode of ESA, in this case)

When the optical carriers in the two interferometer arms mix at the second coupler they interact constructively (add up) and destructively (cancel out) accordingly to their polarization (mis)match. If the polarization of the optical carrier coming from the short arm signal (e, Figure 4-1) is orthogonal to the one from the long arm signal (c, Figure 4-1), the interference will be zero and they will annihilate each other, resulting in the worst PSD. In this scenario, a large resonance peak (point X, Figure 4-2.b) is visible as a result of poor PC optimization. When the optical carriers mix at the same polarization, they add up constructively and we get the maximum power in PSD data, and the noise properly shows the Gaussian and Lorentzian profiles, as shown in (Figure 4-2.h). In this scenario, the X point has disappeared, indicating that the PC adjustment has been finely tuned and that the best measurement for laser linewidth may be obtained with this adjustment.



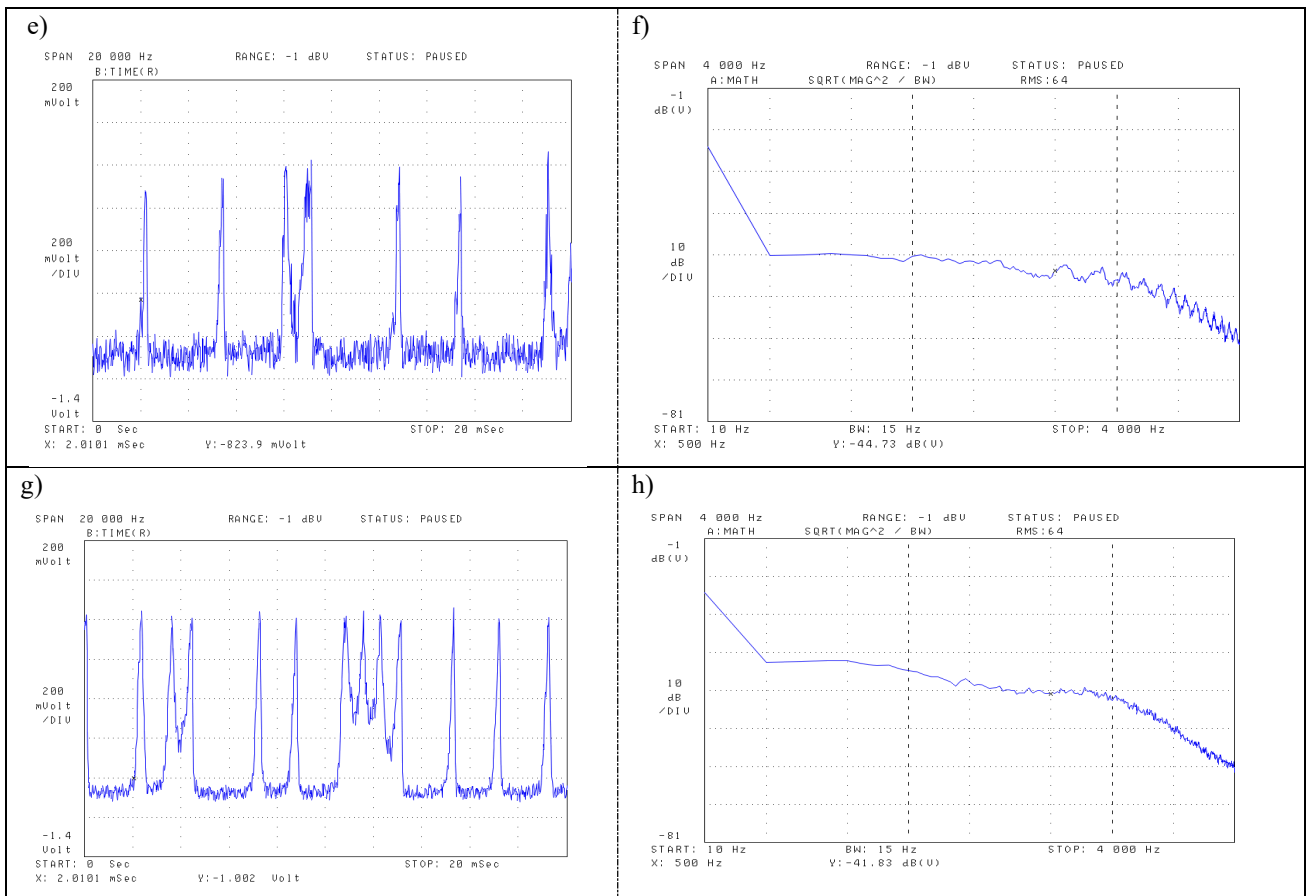


Figure 4-2 The different effects of polarization control adjustment on the PSD results in terms of the obtaining beat signals. **a)** The worst adjustment: The polarization of the signals in two arms are almost perpendicular to each other therefore they cancel out each other. **b)** The worst result: a minimum power is obtained in the PSD and there is a big surge (point G) in the curve. **c)** Bad adjustment: Beat frequency signals are poorly obtained since the polarization control is not adjusted properly. **d)** Bad result: Because the polarization control has not been appropriately tuned, the noise power spectrum density is poor and it does not contain the maximum power, however the X point decreases dramatically. **e)** Without adjustment: the beat signal is not Sharpley observable due to no PC adjustment. **f)** There are many oscillations in the spectrum. **g)** The best adjustment: the beating signal is sharply obtained since the PC is well adjusted. **h)** The best result: noise power spectrum density is obtained as a result of proper OPC adjustment.

Such resonance (point X, Figure 4-2.b) usually appears at the end of the Gaussian fitting and before the descent into the Lorentzian profile. This resonance was similarly observed in our group's previous study: in that experiment a HeNe laser with linewidth  $\sim 750$  Hz presented such resonance at 18 Hz (point G, Figure 4-3), similarly to what is shown now for semiconductor lasers. [6].

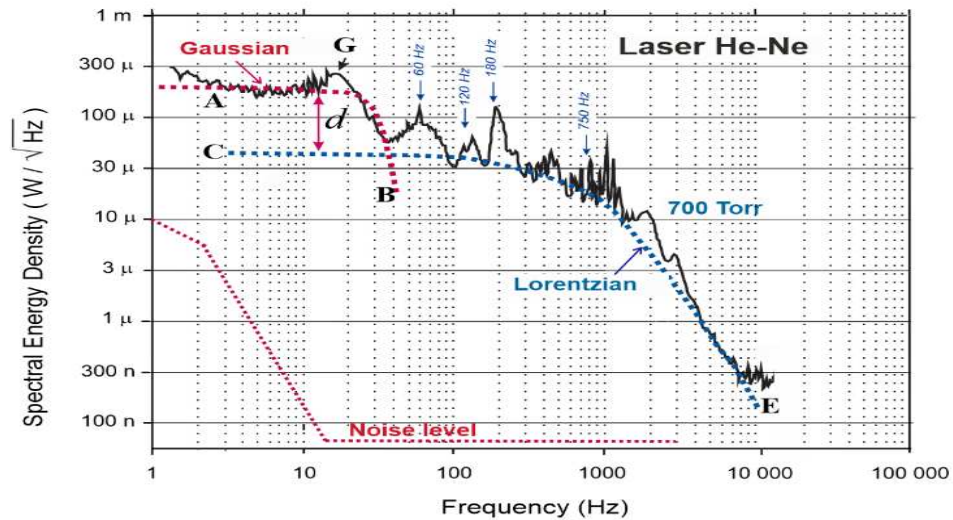


Figure 4-3 The PSD result from some other experiment that reveals the peak G. (Adapted from [6])

This resonance is highly dependent on the Polarization Control adjustment; however, other factors such as laser power and delay fiber length have an effect on the size of the resonance at X, as will be discussed further below.

#### 4.1.2 The effect of laser power on the laser PSD

Figure 4-4.a) presents the spectra with laser output powers ranging from +10 to -10 dBm. For -10 dBm (first curve, bottom of Figure 4-4.a), the spectrum first exhibits the Gaussian profile (AB fit) and subsequently the Lorentzian profile (CE fit). Figure 4-4.a) showed the laser running at higher power, and so more coherent (curves +8 dBm and +6 dBm), the Gaussian noise is smaller than lower power (-10 dBm curve). Another point to consider is the descent of the laser curve; by lowering the laser power, the spectral descent deviates significantly from the Lorentzian fit (Figure 4-4.b). It is worth noting that as the laser power is reduced, a resonance at point X grows larger. However, in high power lasers, this resonance increases (curve +10 dBm), which can be explained by increasing the instability in the laser spectra. This resonance has a constant frequency with power and a value close to 2 kHz. Figure 4-4.b) shows that excess noise at high frequencies tends to be greater at lower powers. For example, at -10 dBm power in the circled region becomes almost flat as a result of higher excess noise. This occurs for all delay fiber length and both lasers (RIO1 and RIO2). In Figure 4-4.a) it is possible to observe the larger the distance  $d$  (for lower laser power), the greater the

low-frequency noise contained in the Gaussian curve. As a result, the excess noise for low frequencies also grows as power decreases. As can be seen that the total noise increases proportionally with decreasing laser power.

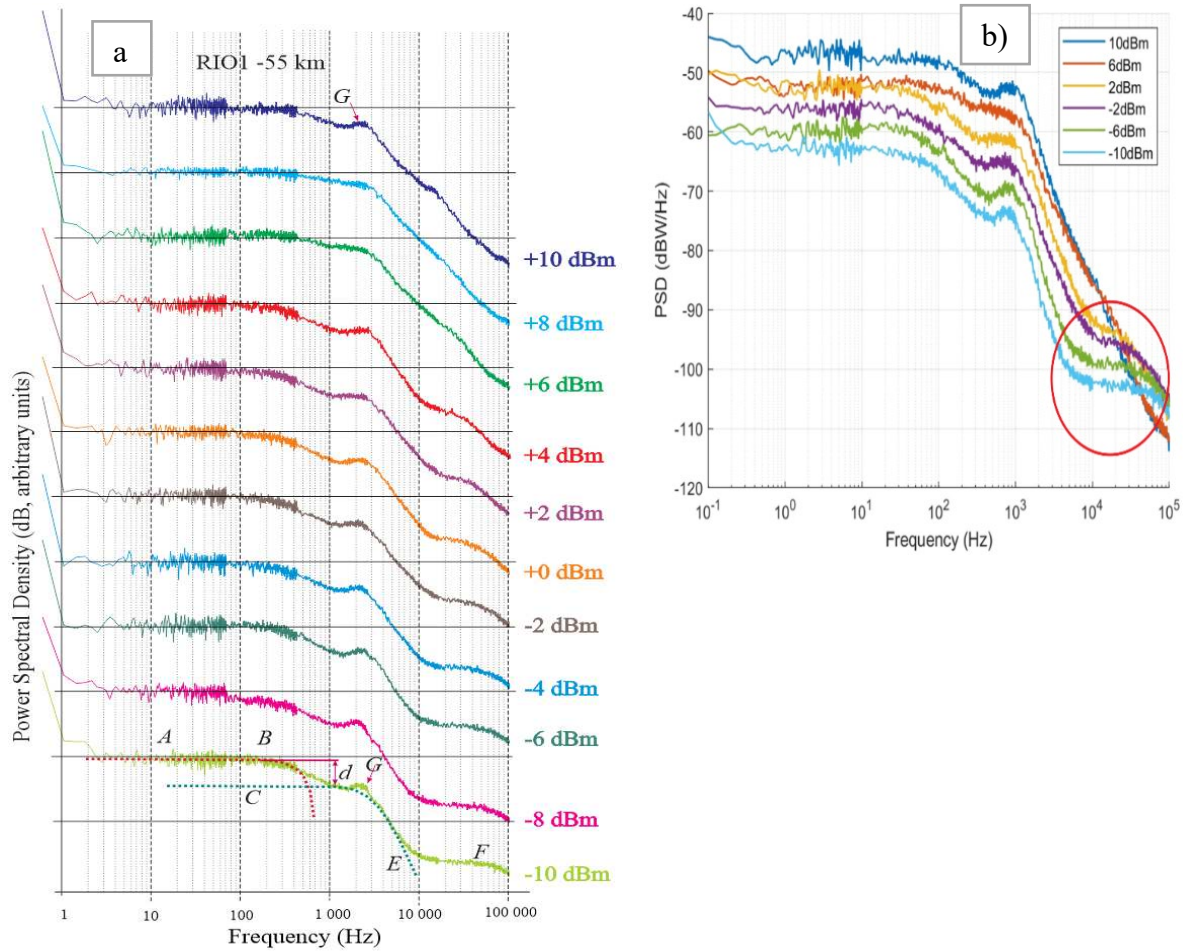


Figure 4-4 **a)** The PSD in relation to laser power for the RIO1 laser with a fiber length of 55 km. It demonstrates that the G point resonance increases as the laser power decreases and gives some details on excess noise at high frequencies for different emission powers. **b)** shows that excess noise at high frequencies tends to be greater at lower powers.

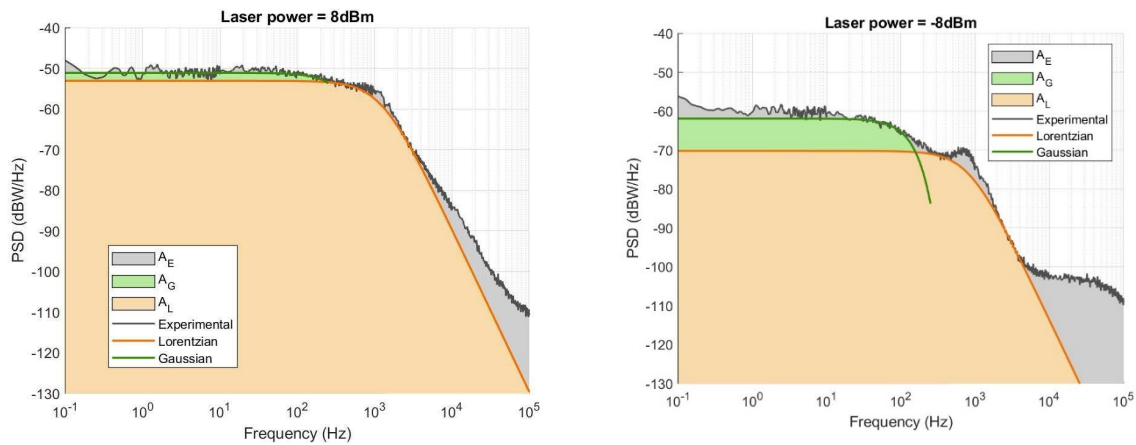


Figure 4-5 It compares laser powers of 8 dBm and -8 dBm (RIO 1) and illustrates that the lower the laser power, the bigger the Gaussian noise. It can be seen that X-point resonance increases as laser power decreases.

Three parts are shown in Figure 4-5, Low Frequency Phase Noise (LFPN),  $A_G$ , which has the Gaussian spectrum, Low Phase Noise (LPN),  $A_L$ , has the Lorentzian spectrum and High Frequency Excess Phase Noise (HFEPN),  $A_E$ , which can be calculated by  $A_E = A_T - A_L - A_G$ , and  $A_T$  is the total power. It is clear that the Gaussian spectrum is smaller at high laser power (+8 dBm) than at low laser power. Low Phase Noise (LPN) is, on the other hand, greater at low laser power than at high laser power.

#### 4.1.3 The effect of fiber length on the laser PSD

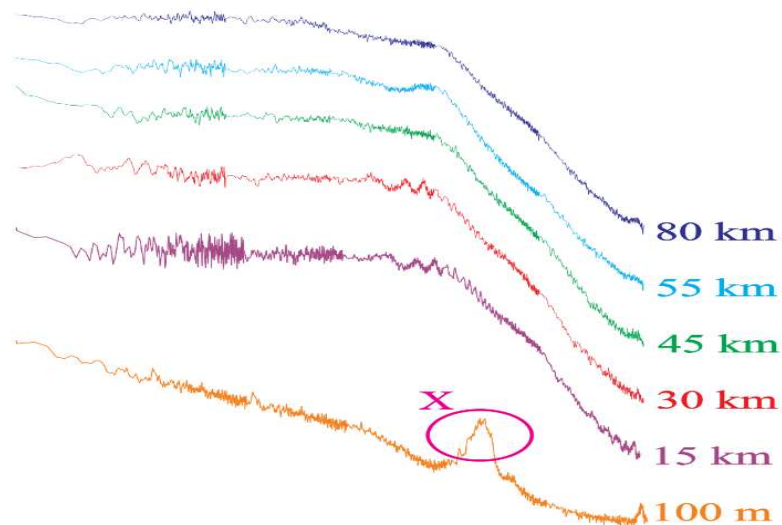


Figure 4-6 PSD comparison for various fiber lengths and 10 dBm laser power (RIO1 laser).

Figure 4-6 shows the laser PSD measurement with the 10 dBm laser power and the delay fiber length ranging from 100 m, 15 km, 30 km, 45 km, 55 km and 80 km. It can be seen that PSD measurement with longer fiber shows a better result since the Lorentzian and Gaussian curve have less noise and the resonance at point X is getting smaller with the longer fiber. The 80 km fiber length yields the best results, although the 55 km and 45 km fiber lengths provide acceptable results if the polarization control is carefully tuned. However, the 30 km and 15 km fiber lengths exhibit excessive oscillations in the PSD, causing some inaccuracy in the Gaussian and Lorentzian fits. When the fiber length is reduced to 100 m, the PSD curve becomes almost unacceptable because the delay time is reduced due to the short fiber length and the phase difference between two arms is decreasing. The PSD measurement is not possible in this case, and as can be seen, the X point resonance becomes very large with the 100 m delay line.

#### 4.2 Linewidth measurement by using Lorentzian and Gaussian curve fits

According to the equations Equation 3.38 and Equation 3.44, the spectrum at  $\frac{W}{Hz}$  is a Lorentzian. For adjusting the experimental curve, the equation Eq.(9) was used. For simplicity, only two parameters are considered here: the linewidth  $\Delta\nu$  and a constant  $\zeta$ , which representing the sum of the other constants,  $k_m$  and  $20 \cdot \log_{10}(\gamma)$ . The Lorentzian fitting is so presented as:

$$L(f) = 20 \cdot \log_{10} \left( \gamma \cdot \frac{\frac{\Delta\nu}{2}}{f^2 + \frac{\Delta\nu^2}{4}} \right) + k_m = 20 \cdot \log_{10} \left( \frac{\frac{\Delta\nu}{2}}{f^2 + \frac{\Delta\nu^2}{4}} \right) + \zeta \quad 4.1$$

The Gaussian noise adjustment was performed according to:

$$g(f) = 20 \cdot \log_{10} \left( \frac{\varepsilon}{\sigma\sqrt{2\pi}} \cdot e^{-\frac{f^2}{2\sigma^2}} \right) + k_g = 20 \cdot \log_{10} \left( e^{-\frac{f^2}{2\sigma^2}} \right) + y \quad 4.2$$

$$= -\eta \cdot f^2 + y$$

With  $y$  equal to the sum of the additive constants  $k_g$  and  $20 \cdot \log_{10} \left( \frac{\varepsilon}{\sigma\sqrt{2\pi}} \right)$  and  $\eta$  equal to the multiplicative constant  $\frac{20 \cdot \log_{10}(e)}{2\sigma^2}$ .

Finally, the equation for noise  $1/f$  was considered as:

$$e(f) = 20 \cdot \log_{10} \left( \frac{\beta}{f} + k_e \right) \quad 4.3$$

where  $\beta$  and  $k_e$  are constants.

The following figures, Figure 9, 10, 11 and 12, are examples of the adjustments made.

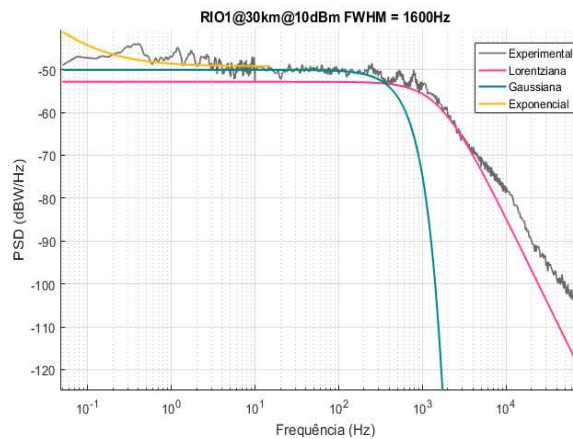


Figure 4-7 Example of curve adjustment, RIO1 setup with 30km of fiber and 10dBm power.

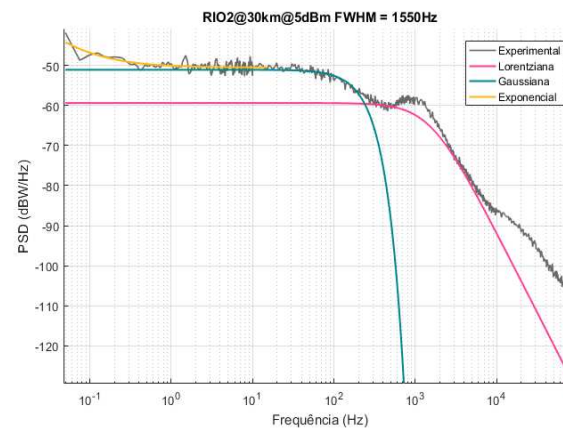


Figure 4-8 Example of curve adjustment, RIO2 setup with 30km of fiber and 5dBm

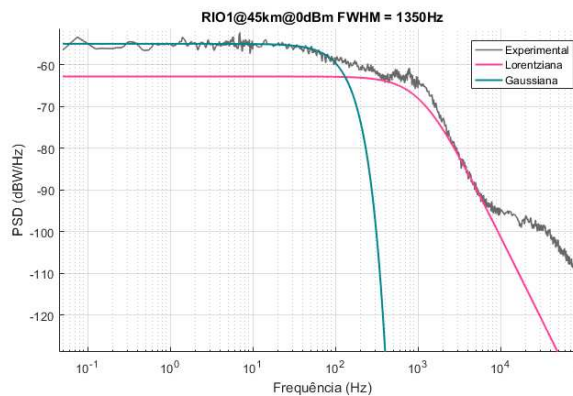


Figure 4-9 Example of curve adjustment, RIO1 setup with 45km of fiber and 0dBm power.

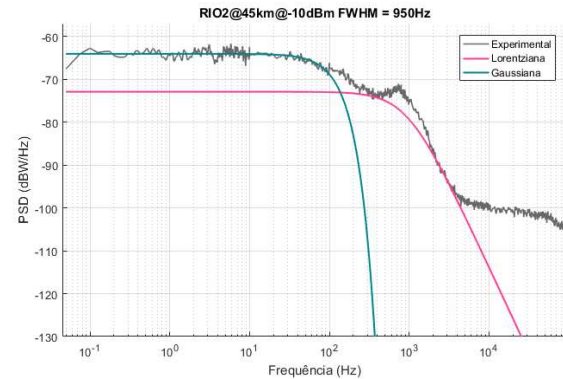


Figure 4-10 Example of curve fitting, RIO2 setup with 45km of fiber and -10dBm power.

Table 4-1 shows the evolution of the coefficients in each experiment. Apparently there is a tendency for the coefficient  $a$  to increase with decreasing power, remembering that  $a = 20 \cdot \log_{10}(e) / 2\sigma^2$ . Therefore, the Gaussian noise appears to have a decrease in standard deviation with decreasing power.

Regarding the linewidth, Table 4-1 shows the values obtained in the adjustment.

Table 4-1 laser linewidth and the coefficient in terms of power

RIO 1								
P(dBm)	80km				55km			
	$\Delta\nu/2$	x	a	b	$\Delta\nu/2$	x	a	b
10	1400	118.5	33	61.8	1225	121.5	7	64.5
8	1250	121	16	65.7	1225	119	4	59.2
6	1050	116.8	17	62.4	1250	118.2	6	59.2
4	1000	112.8	19	60.2	1050	112.5	30	59.5
2	1125	109.7	30	56.3	1250	109.3	45	55.5
0	1075	109.5	35	57.2	1250	107.3	45	55
-2	1175	105.4	30	53.2	1250	103.2	45	50
-4	1150	103.7	50	53.2	1075	100.2	45	48
-6	1025	99.7	55	48.7	1075	97.2	40	46.5
-8	1025	95.3	50	44.6	825	96.5	35	46.5
-10	1025	92.6	45	42	900	94.1	60	44.8
RIO 1								
P(dBm)	45km				30km			
	$\Delta\nu/2$	x	a	b	$\Delta\nu/2$	x	a	b
10	1350	119.5	5	59.5	1450	120	3	59.4
8	1100	123	4	65.2	1350	120.7	15	62
6	1150	116	10	59	1550	118	5	57
4	1050	116	15	60	1100	120	10	62.5
2	1050	114.5	18	60	1350	116.2	3.5	57.5
0	1450	108.5	12	53	1400	111	6	52
-2	1200	105.5	25	52.5	1100	112.2	17	57
-4	1000	101.5	35	50	1075	112.3	22	59.5
-6	1100	98.5	30	48	900	106.7	40	55.5
-8	900	96.5	30	46	1060	98.2	50	49.5
-10	950	92.2	40	42.5	600	95	50	47.5
RIO 2								
P(dBm)	80km				55km			
	$\Delta\nu/2$	x	a	b	$\Delta\nu/2$	x	a	b
10	1100	121.5	20	66.3	1250	119.4	25	59.7
8	1150	120.3	15	63.7	1250	117.9	8	60.2
6	1075	116	10	60.3	1100	118.1	15	62.7
4	1000	114.3	42	62	1175	113.3	20	59.8
2	1125	113	35	60.4	1350	112.3	10	56
0	1075	109.2	45	58.4	1350	111.5	23	57.9
-2	1125	106	45	54	1350	106.5	20	52.9
-4	1125	101.5	40	50	1100	101.8	57	51.4
-6	1050	98.5	60	48.5	1075	100.3	65	50.8
-8	1000	95.8	45	46.5	1125	97.3	40	46.5
-10	1175	91.5	45	41	850	93.5	35	43.3
RIO 2								

P(dBm)	45km				30km			
	$\Delta\nu/2$	x	a	b	$\Delta\nu/2$	x	a	b
10	1400	120	10	62	1400	119	7	61
8					1350	115.2	25	57.5
6					1575	114.2	11	57
4					1100	116.5	45	63
2					1125	112	15	57.3
0	1350	110.2	30	52.5	1400	108	8	50
-2					1275	106.2	37	52.5
-4					1200	102.8	45	50
-6					1000	99	57	49.5
-8					900	96.6	57	46
-10	950	92	48	41.3	950	94.5	48	44

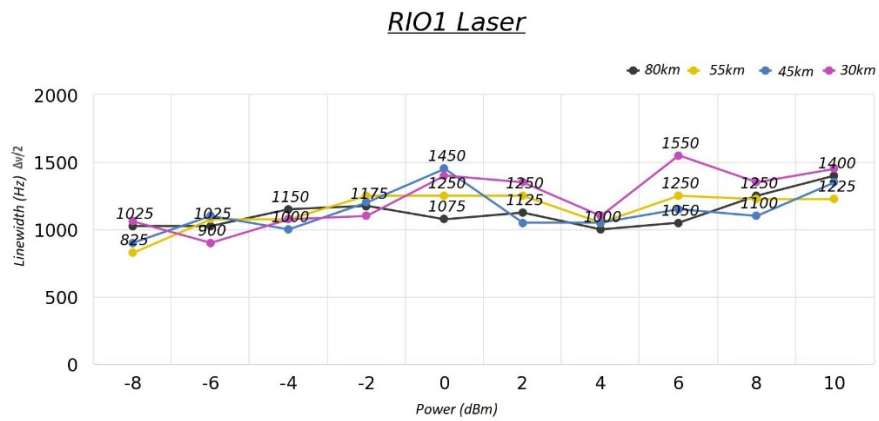


Figure 4-11 The Laser linewidth (Hz) according to optical power (dBm), for RIO 1

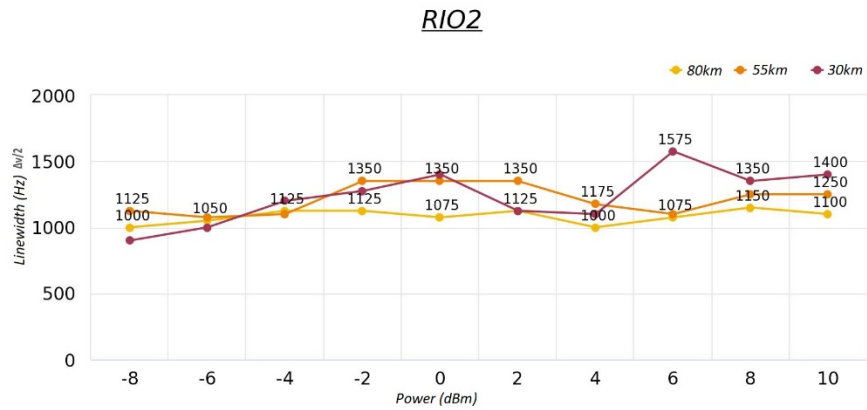


Figure 4-12 The Laser linewidth (Hz) according to optical power (dBm), for RIO 2

### 4.3 Conclusion

In summary

- An adequate fiber length, and a fine polarization control provide better results.
- The excess noise for low frequencies increases with decreasing optical power.
- The proposed setup shows a good estimation for the laser linewidth, however, because the center frequency of the beat notes is around 0 Hz, low-frequency noise in the environment interferes in the obtained results.
- The resonance at point X diminishes for longer fibers and better optical polarization adjustment; however, it gets larger for lower laser powers.
- By decreasing the laser power, the spectral descent profile deviates significantly from the Lorentzian fit.

In conclusion, the delayed self-homodyne optical fiber unbalanced Mach-Zehnder interferometer (MZI) was used to measure different lasers, and the performance was analyzed. The study described here shows that the linewidth and other laser features of can be determined by noise power spectral density (PSD). The low frequency noise was measured and the effect of low frequency noise on the laser linewidth was found.

In this work, various fiber reel lengths (from few meters to 80 km) were used. The low frequency excess noises are characterized for laser powers up to 10 dBm. Additionally, for lasers with linewidths less than 10 kHz (such as IECLs), the high frequency excess noise is examined using Lorentzian fitting.

It was shown that, after a certain delay, the spectra no longer change, indicating decorrelation between the signal on the MZI's long and short arms. Also, it was demonstrated that shorter optical fiber length was needed, as a result external noises (technical noise) such as acoustic and thermal noise. In addition, the Gaussian noise linewidth does not vary with power, but on the other hand the linewidth of the RIO lasers varied with power.

In conclusion, this study contributed to the understanding of laser linewidth measurement and the influence of various factors such as fiber length, polarization control, power levels, and external noise sources. The findings provide valuable insights for optimizing

laser performance, mitigating noise effects, and improving the design and operation of optical systems. Further research can continue to explore these aspects and refine the measurement techniques for a more accurate characterization of laser linewidth and performance.

## 5 kHz Linewidth Laser Characterization using Low Frequency and Excess Noise Measurements

The laser diode spectrum of the instantaneous frequency fluctuation, which is abbreviated as LD FM noise spectrum [49], includes the white noise and the flicker noise (or  $1/f$  noise) which is shown in Figure 5-1 [39]. The White noise is originated from intrinsic spontaneous emission and generates a Lorentzian lineshape (natural linewidth) which is usually predominant above 100 kHz in the spectra [50, 51]. But his assumption is only valid for large spectra devices, not applicable to narrow spectra LD. When the LD output power is increased, the spectral density of white noise decreases, therefore the white noise is a power dependent noise [39]. On the other hand, the  $1/f$  noise is often dominant for  $f < 100$  kHz and presents a Gaussian profile [52]. The  $1/f$  noise is a power-independent noise: it is unchanged by a increasing the output power; therefore, the  $1/f$  noise is responsible for the residual linewidth of laser diode [28]. The residual linewidth was observed first by Welford and Mooradian [39], in the high-power limit, using GaAlAs lasers. In addition, the ultimate receiver sensitivity limit in coherent optical communication systems is determined by such residual linewidth [53]. The FM-noise at the transmitter and at the local oscillator significantly degrades the bit-error rate performance of coherent optical communication systems [54].

This type of noise is called  $1/f$  because its spectral power density is inversely proportional to the frequency, as a result an increase in noise spectral density with decreasing frequency is approximately proportional to  $1/f$  [55]. The  $1/f$  noise is also called 'flicker' noise [39, 56], excess noise [57] or pink noise, and is a low frequency noise. It is a nonstationary stochastic process that is often noticed as a colored noise and observed in all kinds of electronic devices [52, 57, 58]. Low-frequency noise is particularly harmful since it is difficult to filter out with finite-band filters. Low frequency noise (LFN) is usually referred to as fluctuators [59]. Other LFNs such as cavity vibration noises can be observed. Furthermore, the fiber spool and other MZI components produce fiber-induced acoustic noise (FIAN) [6].

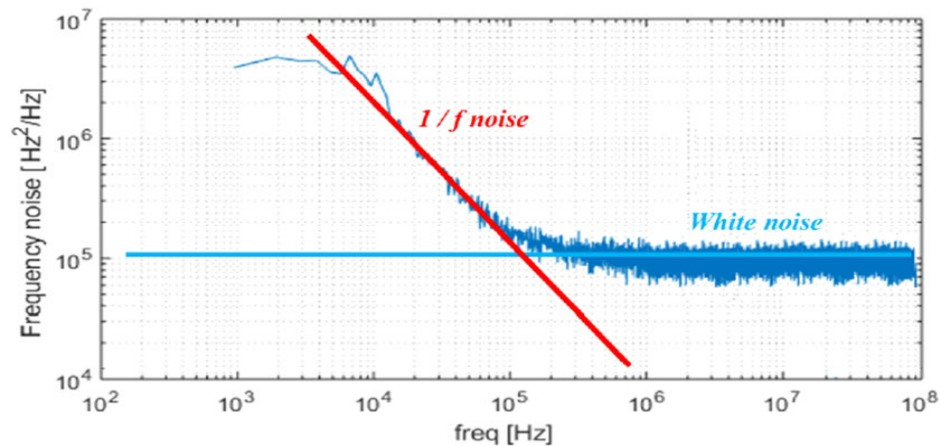


Figure 5-1 Frequency fluctuation includes White Noise and Flicker ( $1/f$ ) Noise. Adapted from [60]

Laser diodes can have significant  $1/f$  noise [61]. The  $1/f$  noise is usually examined above the LD threshold and its spectrum density is practically independent of the bias current changes [62, 63].

### 5.1.1 Origin of $1/f$ noise

Usually, the observed  $1/f$  noise of the electrical current is a quadratic function of the applied voltage in uniform ohmic conductors. It shows that the noise is caused by fluctuation in the sample resistance, which are independent of the average current. Therefore, the current just “reveals” the fluctuations [59]. It is assumed that the  $1/f$  noise is related to the parameters of density and motion of internal particles [55, 59]. One of the most well accepted model is based on the carrier density and/or the mobility fluctuation using the interface-trap-induced charge-carrier-fluctuation theory [64, 65]. McWhorter introduced the interface-trap-induced charge-carrier-fluctuation theory to explain noise in germanium devices. Different authors later confirmed this idea in experiments and successfully adapted it to explain  $1/f$  fluctuations in other semiconductor devices. This model suggests that, in a metal-oxide-semiconductor (MOS) system, charge carriers in the semiconductor interact with the trapping centers in the oxide and in the semiconductor-semiconductor oxide interface through a tunneling mechanism, causing  $1/f$  fluctuations in the channel conductance [64].

The LD BIAS current is a source of  $1/f$  noise due to the generation and recombination process of charged carriers (electrons and holes) [66]. In addition, the noisier the injected bias

current the noisier the laser diode photon stream [46]. There is a direct relationship between electrical noise and optical fluctuations. [46, 47]; and carrier mobility fluctuation causes oscillations in the voltage across the intrinsic LD region. Subsequently, it can lead to the  $1/f$  noise in homogeneous semiconductor lasers [67]. Biasing any semiconductor heterojunction intrinsically produces carrier density fluctuations, such as shot, thermal noise,  $1/f$  noise, etc. These fluctuations will therefore induce fluctuations in the refraction index  $n$  and absorption  $\alpha$ , increasing the frequency and amplitude noises. The  $1/f$  noise originated either in carrier density fluctuations and in absorption fluctuations [60].

Moreover, heterojunction interface degradations can cause the laser malfunctioning. The quality of the heterojunction interface affects the  $1/f$  noise [58, 68]. The  $1/f$  noise is originated from the surface recombination at the p-n junction perimeter or nonradiative recombination at the dislocation in the  $p - n$  junction. It is also possible to determine the  $1/f$  noise by a carrier mobility fluctuation parameter, similar to that for inner regions of p-n junction diodes. The injected carrier density in the active layer is modulated by the bias current noise caused by the  $1/f$ -fluctuation of the nonradiative recombination current, and subsequently the AM and FM noises increase. As the heterojunction interface's degradation continues, some kinds of defects increase at the heterojunction interface [69]. These defects cause an increase in interfacial recombination velocity and then nonradiative recombination current. These defects raise the non-radiative recombination current, which increases the lasing threshold [68, 70]. Therefore, there is a strong relation between  $1/f$  noise and the increase in nonradiative recombination. It can be concluded that the  $1/f$  noise is related to the device degradation and contributes to an increase in the spectral linewidth (FM noise) during the LD degradation [71]. During this degradation, an increase in the nonradiative recombination and  $1/f$  noise fluctuations at the heterojunction interface modulates the injected carrier density in the active layer, increasing the intensity (AM) noise and FM noise.

### 5.1.2 Model origin of $1/f$ noise in BH lasers

During device degradation, the nonradiative recombination current increases, causing  $1/f$  noise to increase and resulting in the rise of in the residual linewidth. Residual linewidth is an important concern in such lasers, determining the minimum linewidth at high output

power. A model that can describe the origin of  $1/f$  noise in buried heterostructure (BH) is shown in

Figure 5-2 [68, 69].

At low bias operation, the current-voltage characteristics are governed by the surface recombination current. In fact, the surface recombination current arises from carrier recombination at the  $p-n$  junction's perimeter. Under forward bias, a portion of the injected electrons and holes are confined to their quantized ground states as minority carriers within the surface's depletion region. Each minority carrier diffuses along the surface of the confining layer until recombination occurs. The surface recombination velocity, the cross-section area, and other factors influence the recombination rate. The recombination current per unit length under high bias at the  $BH$  interface,  $I_{BH}$ , defined by [68]:

$$I_{BH} = qs_0L_{BH}n_i \exp(qV/2kT) \quad 5.1$$

where  $k$  is the Boltzmann constant,  $T$  is the absolute temperature of the  $p-n$  junction,  $q$  is the magnitude of charge of an electron (the elementary charge),  $s_0$  is the intrinsic recombination velocity at the  $BH$  interface and  $L_{RH}$  is the diffusion length along the  $BH$  interface,  $n_i$  is the intrinsic carrier density and  $V$  is the voltage across the  $p-n$  junction. [68].

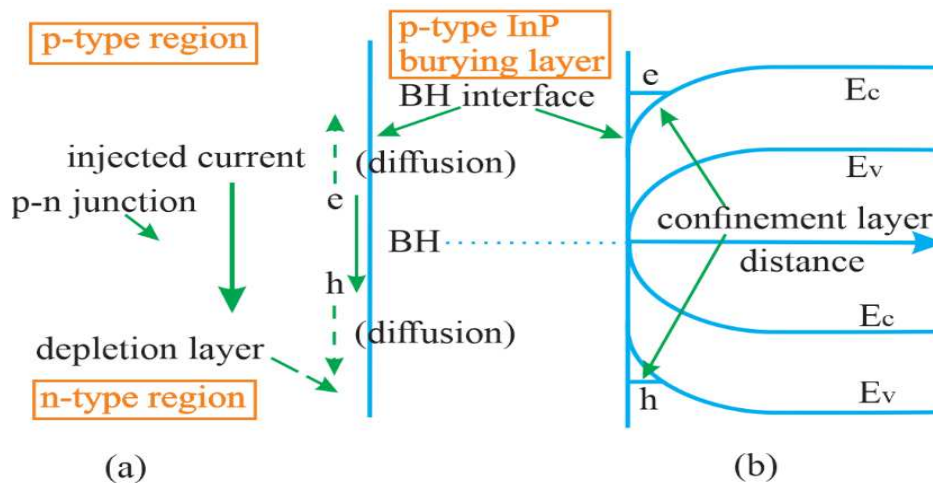


Figure 5-2 Schematic diagram of BH (a) and a band diagram (b). Adapted from [68].

Kleinpenning's approach for the inner bulk region, we can calculate the  $1/f$  noise at the p-n junction perimeter along the BH interface. As a result, the noise spectrum of the non-radiative recombination current under high bias,  $S_I(f)$ , is represented as [68].

$$S_I(f) = \alpha_H q I_{BH} S / 4wf \quad 5.2$$

where  $\alpha_H$  is Hooge's parameter,  $S$  is the interfacial recombination velocity equal to the product of  $s_0$  and the square root of the ratio of the majority carrier density to the minority carrier density outside the depletion layer, and  $w$  is the thickness of the carrier confinement layer. This equation implies that the laser diode has a  $1/f$  noise source at the p-n junction. Furthermore, equation (5.2) demonstrates that  $1/f$  noise caused by surface recombination at the p-n junction perimeter or nonradiative recombination at the p-n junction dislocation is determined by a carrier mobility fluctuation similar to that seen in p-n junction diode inner regions [68].

The injected carrier density in the active layer is modulated by the current noise induced by the  $1/f$  fluctuation of the non-radiative recombination current, and the FM noise rises as a result of the growth in AM noise through a spectral linewidth enhancement factor (or parameter). The following equation can be used to connect the laser frequency fluctuation,  $\delta v$ , with gain fluctuation,  $\delta g$  [68]:

$$\delta v = (\lambda/4\pi)\beta_c (v/\mu_g) \delta g = (c/4\pi\mu_g) \beta_c \delta g \quad 5.3$$

where  $\lambda$  is the free-space wavelength,  $\beta_c$  is the linewidth enhancement factor;  $v$  represents the laser frequency and  $\mu_g$  is the group refractive index. The velocity of light is denoted by  $c$ .

The white noise and the  $1/f$  noise influences the FM noise level of a semiconductor laser, and white noise is virtually constant. As a result of equations (5.1)-(5.3), the FM noise spectrum of a laser can be represented as

$$\begin{aligned} S_{FM}(f) &= C + S_v(f) \\ &= C + (c/4\pi\mu_g)^2 \beta_c^2 S_g(f) \\ &= C + K (c/4\pi\mu_g)^2 \beta_c^2 S_I(f) \end{aligned} \quad 5.4$$

where  $C$  is a term associated with white noise.  $S_v(f)$  is the noise spectrum for laser frequency fluctuation, and  $K$  is also a constant determined by the active volume, gain factor.

These equations demonstrate that the  $1/f$  noise is affected by the BH interface's quality both during the initial stage and throughout its aging degradation. The interfacial recombination velocity,  $S$ , steadily increases throughout degradation [68, 69].

This model can also describe effectively the noise behavior of lasers devices. Because the Fermi level is fixed after the lasing threshold, the  $1/f$  noise (ie. the residual linewidth) is constant in this model. This is due to a constant  $I_{\text{BH}}$  and a constant  $S_l(f)$  after lasing. Before degradation, a nonradiative recombination current exists at the BH interface or surface. Therefore, the initial noise behavior and residual linewidth of laser diodes are also governed by these nonradiative recombination currents [69].

### 5.1.3 Low Frequency Noise (LFN) analysis

Nowadays, semiconductor lasers are appealing because to their single-frequency output stability, high modulation rate capability and sustained working lifetimes of about  $10^8$  hours at room temperature. The noise characteristic investigations aid in the development of laser diodes with optimum characteristics as well as the acquisition of further knowledge on the physical processes that occur in laser diodes. Low thermal impedance, good mode shape control and particularly strong current confinement are all advantages of semiconductor laser diodes [46].

The LFN spectrum is one of the most important aspects of the sampling data used to evaluate LD reliability and stability [68]. As a result, the LFN is regarded as a significant feature of LDs that requires further research [47]. There is a correlation between LFN intensity fluctuations and frequency fluctuations in the optical emission [62]. The  $1/f$  noise is observed in the frequency noise spectra, which expands the linewidth of the laser light [47]. The  $1/f$  noise is converted into phase noise through the devices nonlinearities and degrades the LD PDS purity [72]. Optoelectronic devices are part of this process, such as any electronic device involved in the link [32].

It is possible to study the internal defect in LDs by analyzing some of its LFN characteristics[1]. Some factors like internal defects, surface damage and surface leakage current cause the carriers to be captured and released in a stochastic manner by the interface traps, resulting in tiny current fluctuations [64, 65]. The measured LFN can indicate internal

defects in the active region and can be used to assess the device performance and lifetime of the semiconductor lasers [1]. Therefore, the LFN measurement under the working currents of the laser diodes can be used as an effective, nondestructive testing method to assess the reliability [73, 74]. Electric aging tests, as the traditional destructive examination method, are commonly used to assess the reliability of diode lasers [75]. Long-term testing under high current, particularly for high-power semiconductor laser diodes, can damage the active region's material and severely harm the system internal structure due to the high injected current. So, it is important to look for non-destructive testing process [1]. It is experimentally demonstrated that the residual spectral linewidth's increase during LD degradation is due to increase in the  $1/f$  noise. Also, the spectral linewidth increase is closely related to interface degradation in the buried heterostructure (BH) [76]. As the LD degradation proceeds, the linewidth gradually increases and the residual linewidth increases. The residual linewidth is determined by the  $1/f$  noise. Thus, it can degrade data transmission rate and increase bit-error rate [69].

## 5.2 Methodology

One of the most well-known techniques for measuring the LFN noise is the delayed self-homodyne optical fiber unbalanced Mach-Zehnder interferometer (UMZI). The laser frequency noise PSD can be directly measured by an RF spectrum analyzer using the homodyne process [37]. This method extracts the PSD of laser frequency noise from the PSD of the self-homodyne beat signal. The LFN fluctuations can be measured on the laser, for both its frequency and amplitude [67]. This technique cannot be used in non-symmetrical PSD LD.

The setup is the same as the one of the previous chapter, experimental configuration (self-homodyne detection) which is shown in Figure 4-1. The self-homodyne interferometer is configured to investigate the spectral component of the intrinsic noises of an Integrated External Cavity laser (IECL) with variable fiber delay length,  $L$ , and laser power,  $P$ .

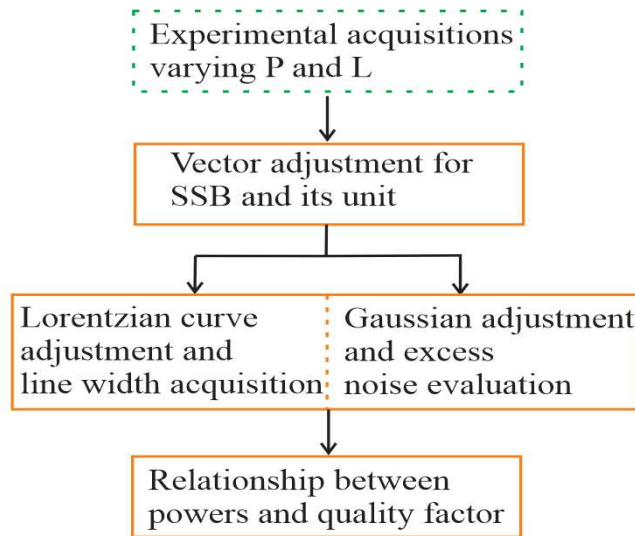


Figure 5-3 The key functions of the created algorithm.

Figure 5-3 displays a block diagram of the results analysis and the algorithm developed using the MATLAB program to obtain the data in order to process the results. In the first block the experimental results with different laser powers and optical fiber lengths were acquired from the Spectrum Analyzer to the computer by the software (7470.EXE emulator). In the following block, some mathematical calculations were performed in order to convert the noise PSD unite from  $\frac{dBV}{\sqrt{Hz}}$  to  $\frac{dBW}{Hz}$  and also to alter the vector of the shape graph so that it could be analyzed by the MATLAB program. In the third block the theoretical approximations are made for modeling the experimental curve, so that a Lorentzian was adjusted to approximate the  $S(f)$  form. The bandwidth in the half-spectrum (FWHM - Full Width at Half Maximum) of the laser under test is derived as a result of this adjustment. A Gaussian adjustment was also considered for modeling the noise at low frequencies. Equations 5.5 and 5.6 were used to fit Lorentzian and Gaussian curves, respectively:

$$L(f) = c \cdot \frac{\frac{\Delta_v}{2}}{f^2 + \left(\frac{\Delta_v}{2}\right)^2} \quad 5.5$$

$$G(f) = \frac{a}{\sigma\sqrt{2\pi}} \cdot \exp\left(\frac{-f^2}{2\sigma^2}\right) \quad 5.6$$

where  $a$  and  $c$  are constants,  $\sigma$  is the standard deviation of Gaussian noise, and  $\Delta_v$  is the FWHM linewidth.

Finally, the theoretical fitting curves are used to calculate the percentage of power contained in each of the three major regions of the PSD spectrum, as illustrated in Figure 5-5. These three parts are Low Frequency Phase Noise (LFPN),  $P_G$ , which has the Gaussian spectrum, Low Phase Noise (LPN),  $P_L$ , has the Lorentzian spectrum and High Frequency Excess Phase Noise (HFEPN),  $P_E$ . The total power is,  $P_T$ . As a result, the discrete integrals 5.7, 5.8 and 5.9 are developed.

$$P_G = \sum_{f=0}^n G(f) \cdot \Delta f(f) \quad 5.7$$

$$P_L = \sum_{f=0}^n L(f) \cdot \Delta f(f) \quad 5.8$$

$$P_T = \sum_{f=0}^n PSD(f) \cdot \Delta f(f) \quad 5.9$$

The term  $\Delta f(f)$  in 5.7 to 5.9 describes the width of the rectangle in the integration, or, in the physical sense, the frequency spacing between two subsequent points.  $PSD(f)$  in equation 5.9 represents the experimental spectral points acquired at each frequency  $f$ . It is worth noting that  $P_E = P_T - P_L - P_G$ .

Based on the PSD power analyzes presented here, the Relative Excess Noise (REN) is proposed to evaluate both low frequency and high frequency noises. So, the REN is defined as the ratio between the overall laser noises power outside the Lorentzian spectrum and the power inside the Lorentzian fitting of the PSD, as shown in equation 5.10.

$$REN = \frac{P_E + P_G}{P_L} \quad 5.10$$

### 5.3 Results and discussion

Figure 5-4 depicts a typical curve of the results obtained using the proposed methodology, with points A, B, C, and D indicating relevant parts of the spectrum that will be used as a reference for the discussion presented in this section. Firstly, a peak is observed in the experimental measurement at point A in Figure 5-6.a), indicating the presence of noise that begins at 0 Hz and extends to around 190 Hz. Figure 5-6.c) shows the Gaussian distribution model revealed good correlation in this part, therefore this frequency range was theoretically approximated using equation 5.5, as illustrated in greater detail in Figure 5-5 (green line). However, the contribution of this noise is minor, accounting for less than 0.02% of total power.

It is estimated that environmental factors, such as mechanical vibrations and temperature variations, as well as factors arising from the device dynamics are related in this region. Furthermore, in Figure 5-6.d) the existence of type 1/f noise was observed that extends to approximately 7 Hz (red trace) which can be seen in Figure 5-5.

At point B in Figure 5-4, there is noise caused, among other things, by the non-optimization of the polarization adjustment process and the laser's emission power. It occurs very slightly in the situation described here. However, even if it is minor, its presence causes a difference in the experimental outcome from what is theoretically expected.

Following that, the experimental and theoretical curves have the best correlation in the region of point C, which can be observed in Figure 5-4 and Figure 5-5 (orange line). The fitting was made using a Lorentzian approximation and discarding the Gaussian noise which is represented by point A, and the apparent noise at frequencies above 5 kHz. The laser's FWHM line width is determined by Lorentzian fitting. Figure 5-5 shows the adjustment (orange trace), leading in  $\Delta_{v(-6dB)} = 1350$  Hz and  $\Delta_{v(-20dB)} = 4025$  Hz. The observed result is consistent with the value  $\Delta_{v(-20dB)} = 2200$  Hz which is provided by RIO manufacturer for the laser type utilized here, RIO0184-3-01-4- C9, but with the device operating at maximum power of around 13 dBm.

Finally, in the region denoted by D in Figure 5-4, shows the beginning of the mismatch between the expected theoretical curve and experimental measurement. It indicates the presence of noise at frequencies larger than 5 kHz in this example. This noise may be caused by apparently, the spontaneous emission noise (ASE - Amplified Spontaneous Emission) of the device itself combined with its delayed replica, as shown in Figure 5-5. The Gaussian noise covers an almost insignificant portion of the power while the noise in frequencies above 5 kHz covers a significant part of the spectrum

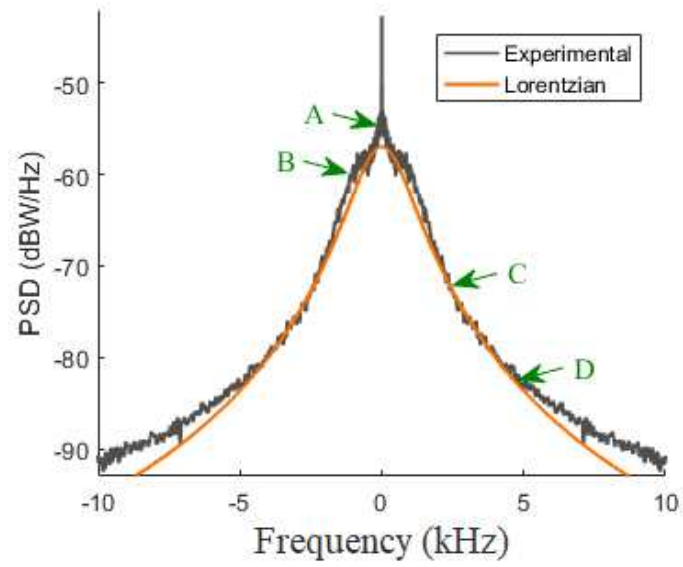


Figure 5-4 The experimental spectrum highlighting points of interest.

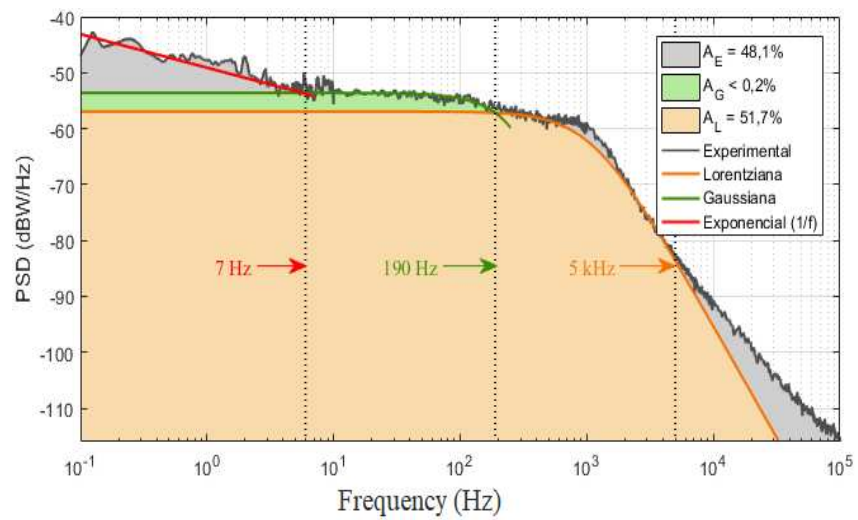


Figure 5-5 Experimental result evaluating the relationship between the parts of the spectrum.

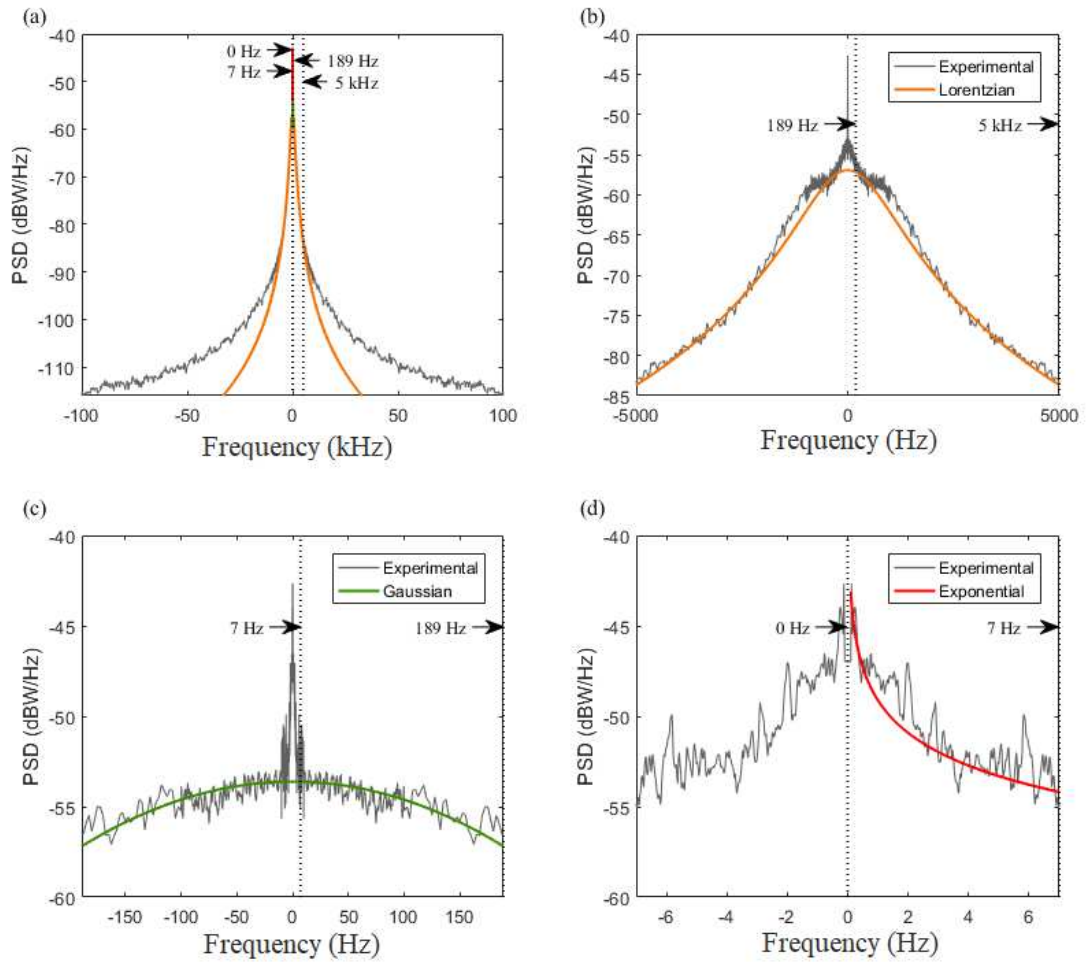


Figure 5-6 Using the fitting curve for each part of the spectrum.

Table 5-1 The three main parts of PSD and the quality Q of laser.

<b>RIO 1</b>										
P(dBm)	80km					55km				
	PT	PL	PG	PE	REN	PT	PL	PG	PE	REN
10	9.866	6.621	1.441	1.805	0.490	9.818	5.448	2.327	2.042	0.802
8	6.208	3.440	1.692	1.076	0.805	6.204	4.646	0.717	0.841	0.335
6	3.925	2.049	0.948	0.928	0.916	3.911	2.775	0.583	0.553	0.410
4	2.475	1.110	0.782	0.583	1.230	2.465	1.129	0.578	0.758	1.184
2	1.553	0.920	0.468	0.165	0.688	1.557	0.814	0.334	0.410	0.914
0	0.987	0.491	0.294	0.201	1.009	0.983	0.440	0.284	0.259	1.234
-2	0.620	0.276	0.214	0.130	1.246	0.620	0.307	0.152	0.160	1.017
-4	0.392	0.161	0.143	0.088	1.434	0.392	0.177	0.093	0.122	1.215
-6	0.247	0.103	0.062	0.082	1.403	0.247	0.086	0.075	0.087	1.888
-8	0.156	0.058	0.041	0.056	1.672	0.156	0.060	0.047	0.049	1.586

-10	0.097	0.037	0.029	0.032	1.659	0.098	0.037	0.029	0.032	1.624
<b>RIO 1</b>										
P(dBm)	45km					30km				
	PT	PL	PG	PE	REN	PT	PL	PG	PE	REN
10	9.82	7.72	1.40	0.70	0.27	9.84	6.71	1.54	1.58	0.47
8	6.20	4.19	1.33	0.68	0.48	6.21	4.48	0.77	0.96	0.39
6	3.92	2.88	0.86	0.18	0.36	3.73	1.86	0.33	1.55	1.01
4	2.48	1.67	0.46	0.34	0.48	2.45	1.73	0.37	0.36	0.42
2	1.56	0.91	0.39	0.26	0.71	1.55	0.73	0.30	0.52	1.11
0	0.98	0.46	0.32	0.20	1.13	0.99	0.64	0.19	0.15	0.53
-2	0.62	0.30	0.21	0.11	1.07	0.62	0.36	0.14	0.12	0.73
-4	0.39	0.18	0.12	0.09	1.17	0.38	0.17	0.12	0.10	1.25
-6	0.25	0.09	0.11	0.05	1.63	0.25	0.10	0.06	0.09	1.40
-8	0.16	0.06	0.05	0.04	1.42	0.15	0.05	0.06	0.05	2.35
-10	0.10	0.04	0.04	0.02	1.56	0.10	0.05	0.04	0.01	1.05
<b>RIO 2</b>										
P(dBm)	80km					55km				
	PT	PL	PG	PE	REN	PT	PL	PG	PE	REN
10	9.85	5.66	1.97	2.22	0.74	9.82	7.21	0.30	2.32	0.36
8	6.21	4.05	1.10	1.06	0.54	6.21	4.13	1.31	0.76	0.50
6	3.92	2.29	0.97	0.66	0.71	3.91	2.31	0.90	0.70	0.69
4	2.47	1.29	0.61	0.57	0.91	2.45	0.98	0.66	0.80	1.49
2	1.56	0.76	0.45	0.35	1.05	1.56	0.83	0.44	0.29	0.88
0	0.98	0.41	0.33	0.24	1.38	0.98	0.43	0.32	0.24	1.31
-2	0.62	0.29	0.17	0.17	1.18	0.62	0.27	0.22	0.14	1.32
-4	0.39	0.17	0.13	0.09	1.25	0.39	0.14	0.11	0.14	1.78
-6	0.25	0.09	0.07	0.09	1.78	0.25	0.09	0.08	0.07	1.66
-8	0.16	0.05	0.06	0.05	1.97	0.16	0.06	0.06	0.04	1.57
-10	0.10	0.03	0.03	0.04	2.32	0.10	0.04	0.03	0.03	1.64
<b>RIO 2</b>										
P(dBm)	45km					30km				
	PT	PL	PG	PE	REN	PT	PL	PG	PE	REN
10	9.83	9.93	4.02	-4.11	-0.01	9.74	5.27	2.09	2.38	0.85
8						6.08	4.16	0.76	1.16	0.46
6						3.91	2.04	1.02	0.86	0.92
4						2.48	1.38	0.49	0.61	0.80
2						1.55	0.78	0.40	0.37	0.99
0	0.99	0.71	0.41	-0.14	0.38	0.99	0.59	0.22	0.18	0.67
-2						0.62	0.32	0.16	0.13	0.90
-4						0.39	0.19	0.10	0.10	1.07
-6						0.24	0.09	0.08	0.08	1.74
-8						0.16	0.07	0.04	0.05	1.25
-10	0.10	11.81	2.35	-14.06	-0.99	0.10	0.04	0.03	0.03	1.61

In Table 5-1 the three major regions of the PSD spectrum and laser quality are presented for two lasers (RIO 1, RIO 2) for different fiber lengths. It demonstrates that as the laser power is reduced, the quality decreases. The RIO1 laser offers superior performance and reliability than the RIO2 laser, and so has a higher Q value for each corresponding fiber length and power. Figure 5-7 and Figure 5-8 show other results for 55 km fiber length with 10 dBm and 2 dBm.

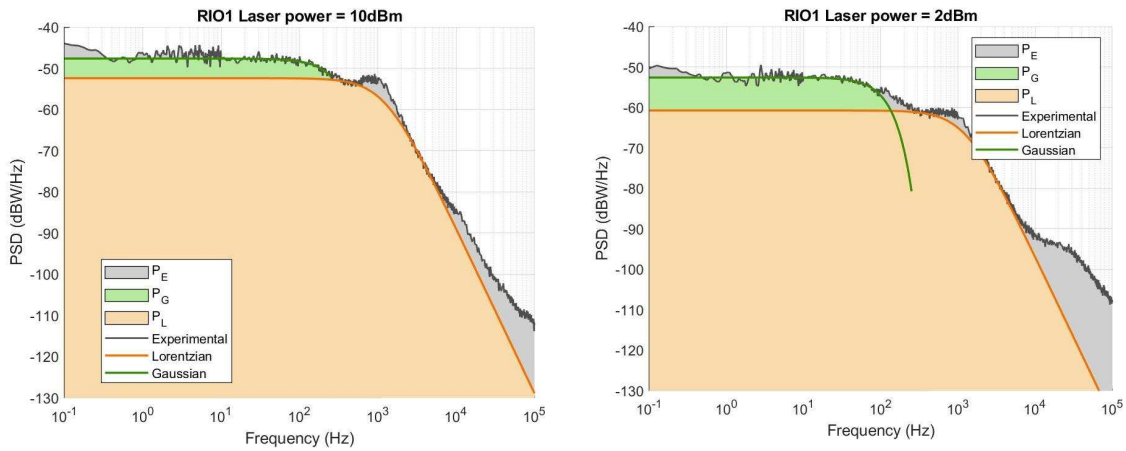


Figure 5-7 PSD with three different areas for 55 km fiber length and 10 dBm laser power.

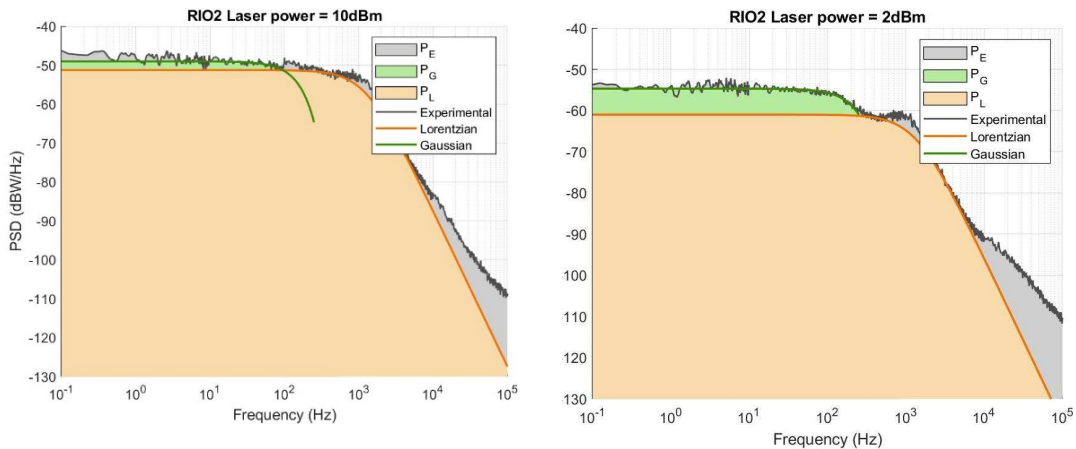


Figure 5-8 PSD with three different areas for 55 km fiber length and 10 dBm laser power.

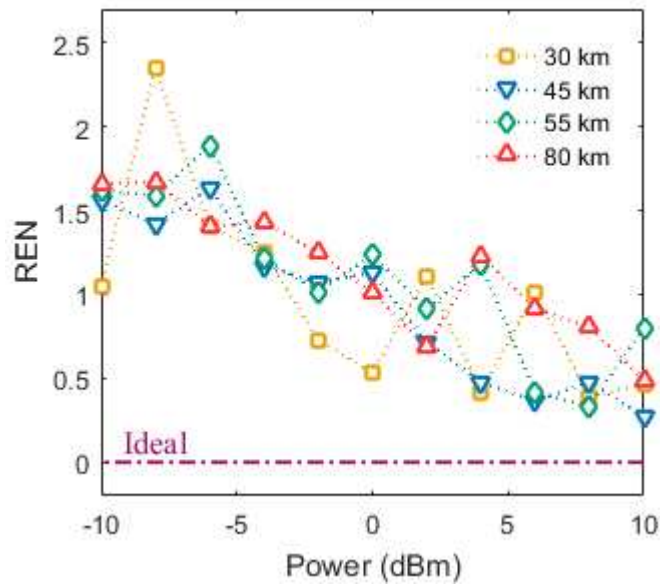


Figure 5-9 Laser relative excess noise (REN) in terms of power (RIO1).

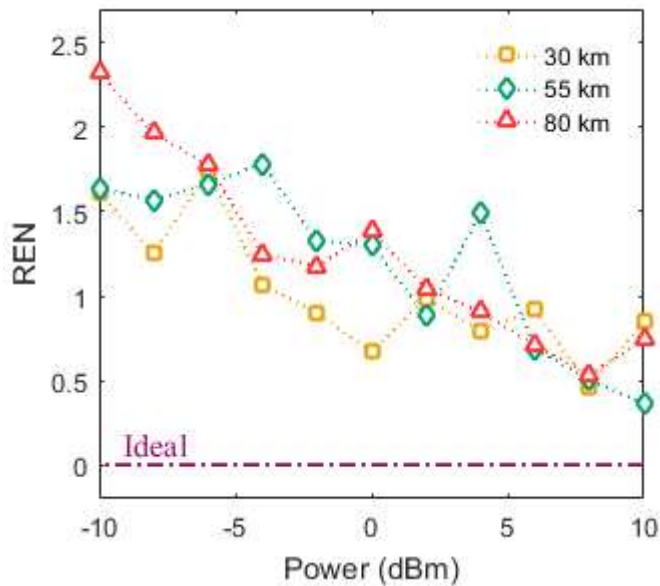


Figure 5-10 Laser relative excess noise (REN) in terms of power (RIO2).

## 5.4 Conclusion

The methodology proposed the investigation of phase fluctuations and excess noise in a coherent optical field. The three main components of LFN are theoretically and experimentally evaluated, and the non-destructive method is presented to determine the quality of laser for two lasers with different fiber length. The methodology proposed the investigation of phase

fluctuations and excess noise in a coherent optical field. By analyzing the phase fluctuation and excess noise of a coherent optical field, it is possible to measure the laser quality with higher accuracy. This non-destructive method can be used to measure laser quality with higher accuracy, while providing a much more thorough evaluation of the three components of LFN - phase fluctuations, excess noise, and fiber length.

The results obtained from the application of this methodology to two lasers with different fiber lengths have demonstrated its effectiveness in accurately measuring laser quality. By successfully characterizing and quantifying the phase fluctuations and excess noise, valuable information about the laser's stability, coherence, and noise characteristics can be obtained.

This non-destructive method has great potential for widespread application in various fields that rely on precise laser quality assessment, including optical communications, metrology, spectroscopy, and sensing. Its capability to provide a more thorough evaluation of laser performance can enhance the design and optimization of optical systems, leading to improved efficiency, higher data rates, and better measurement accuracy.

In conclusion, the proposed methodology for investigating phase fluctuations and excess noise in a coherent optical field, along with the non-destructive laser quality assessment, presents a significant advancement in laser characterization techniques. By offering a more comprehensive evaluation of LFN components and enabling accurate laser quality measurement, this methodology has the potential to drive advancements in various photonics applications and contribute to the development of high-performance optical systems.

## **5.5 Future works**

As mentioned in this chapter, the method described here was able to not only assess the linewidth of semiconductor lasers but also to give a more detailed understanding of the behavior of the optical carrier and the circumstances that can result in its coherence breakdown. A prospective future project is anticipated, an evolution of such a technology, which presents the opportunity for new scientific challenges relating to the characterization of non-linear phenomena, such as spectral broadening and temporal tremor (jitter) in photonic devices. Additionally, a deeper examination is required to fully understand the remarkable occurrences connected to the optical carrier's loss of coherence. It is suggested to do a thorough investigation into physical phenomena such thermal emissions, spectral hole burning, and

fluctuations in the semiconductor laser's refractive index. In order to confirm the impact of variables like polarization current, temperature, signal-to-noise ratio, and dark current on the appearance of these events, a comparative study based on the variation of several operational parameters of the experimental setup is also required.

Further research is required to establish the technique's viability as a non-destructive means of assessing laser quality. Conducting experiments with different lasers, varying parameters such as fiber length, environmental temperature, and noise conditions, will help validate the method's efficiency and robustness across a wider range of scenarios. This will ensure its applicability to different types of lasers and enable the identification of any potential limitations or constraints.

## 6 References

- [1] J. Guan, S. Guo, J. Wang, M. Tao, J. Cao, and F. Gao, "Analysis of origin of measured 1/f noise in high-power semiconductor laser diodes far below threshold current," *Microelectronics Reliability*, vol. 59, pp. 55-59, 2016/04/01/ 2016, doi: <https://doi.org/10.1016/j.microrel.2015.12.029>.
- [2] L. Riuttanen *et al.*, "Diffusion injected multi-quantum well light-emitting diode structure," *Applied Physics Letters*, vol. 104, no. 8, pp. 081102-0811024, 2014, doi: DOI:101063/14866343.
- [3] Y. Liu, S. Zhao, S. Yang, Y. Li, and R. Qiang, "Markov process based reliability model for laser diodes in space radiation environment," *Microelectronics Reliability*, vol. 54, no. 12, pp. 2735-2739, 2014/12/01/ 2014, doi: <https://doi.org/10.1016/j.microrel.2014.08.006>.
- [4] J. Yang *et al.*, "Numerical simulation of phase modulation method used as high sensitive self-mixing vibrometry in vertical-cavity surface-emitting laser," *Optik*, vol. 124, no. 23, pp. 6017-6019, 2013/12/01/ 2013, doi: <https://doi.org/10.1016/j.ijleo.2013.04.107>.
- [5] X. Zhang, S. Thapa, and N. Dutta, "All-optical XOR gates based on dual semiconductor optical amplifiers," *Cogent Physics*, vol. 6, no. 1, p. 1660495, 2019/01/01 2019, doi: 10.1080/23311940.2019.1660495.
- [6] E. Conforti, M. Rodigheri, T. Sutili, and F. J. Galdieri, "Acoustical and 1/f noises in narrow linewidth lasers," *Optics Communications*, vol. 476, p. 126286, 2020/12/01/ 2020, doi: <https://doi.org/10.1016/j.optcom.2020.126286>.
- [7] "rio-lasers.com." rio-lasers.com (accessed).
- [8] D. F. Welch, "A brief history of high-power semiconductor lasers," *IEEE Journal of Selected Topics in Quantum Electronics*, vol. 6, no. 6, pp. 1470-1477, 2000, doi: 10.1109/2944.902203.
- [9] F. J. Galdieri, T. Sutili, N. Melnikoff, A. C. Bordonalli, and E. Conforti, "Influence of exterior acoustic noise on narrow linewidth laser measurements using self-homodyne optical fiber interferometer," *Optik*, vol. 204, p. 164101, 2020/02/01/ 2020, doi: <https://doi.org/10.1016/j.ijleo.2019.164101>.
- [10] A. Hussein Ali and N. Abdul-Wahid, "Analysis of Self-Homodyne and Delayed Self-Heterodyne Detections for Tunable Laser Source Linewidth Measurements," vol. 2, pp. 1-06, 10/01 2012.
- [11] J. Zhang, J. Yu, and H.-C. Chien, "Advanced linear and nonlinear compensations for 16QAM SC-400G unrepeated transmission system," *Optics Communications*, vol. 409, pp. 34-38, 2018/02/15/ 2018, doi: <https://doi.org/10.1016/j.optcom.2017.07.017>.
- [12] Y. Fu, H. Liu, and J. Xie, "100-m standoff detection of a QCL-induced photo-vibrational signal on explosives using a laser vibrometer," *Optics and Lasers in Engineering*, vol. 107, pp. 241-246, 2018/08/01/ 2018, doi: <https://doi.org/10.1016/j.optlaseng.2018.04.003>.
- [13] L. Shi, T. Zhu, Y.-e. Fan, K. S. Chiang, and Y. Rao, "Torsion sensing with a fiber ring laser incorporating a pair of rotary long-period fiber gratings," *Optics Communications*, vol. 284, no. 22, pp. 5299-5302, 2011/10/15/ 2011, doi: <https://doi.org/10.1016/j.optcom.2011.07.049>.
- [14] C. S. Goldenstein, R. M. Spearrin, J. B. Jeffries, and R. K. Hanson, "Infrared laser-absorption sensing for combustion gases," *Progress in Energy and Combustion Science*, vol. 60, pp. 132-176, 2017/05/01/ 2017, doi: <https://doi.org/10.1016/j.pecs.2016.12.002>.

- [15] D. Xu *et al.*, "Laser phase and frequency noise measurement by Michelson interferometer composed of a 3 x 3 optical fiber coupler," *Opt. Express*, vol. 23, no. 17, pp. 22386-22393, 2015/08/24 2015, doi: 10.1364/OE.23.022386.
- [16] T. Okoshi, K. Kikuchi, and A. Nakayama, "Novel method for high resolution measurement of laser output spectrum," *electronics letters*, vol. 16, no. 16, pp. 630-631, 7/31/1980 1980, doi: 10.1049/EL:19800437.
- [17] H. Tsuchida, "Laser frequency modulation noise measurement by recirculating delayed self-heterodyne method," *Opt. Lett.*, vol. 36, no. 5, pp. 681-683, 2011/03/01 2011, doi: 10.1364/OL.36.000681.
- [18] J. Gao *et al.*, "A Polarization-Insensitive Recirculating Delayed Self-Heterodyne Method for Sub-Kilohertz Laser Linewidth Measurement," *Photonics*, vol. 8, no. 5, 2021, doi: 10.3390/photonics8050137.
- [19] H. Ludvigsen, M. Tossavainen, and M. Kaivola, "Laser linewidth measurements using self-homodyne detection with short delay," *Optics Communications*, vol. 155, no. 1, pp. 180-186, 1998/10/01/ 1998, doi: [https://doi.org/10.1016/S0030-4018\(98\)00355-1](https://doi.org/10.1016/S0030-4018(98)00355-1).
- [20] Z. Bai *et al.*, "Narrow-Linewidth Laser Linewidth Measurement Technology," *Frontiers in Physics*, vol. 9, 11/24 2021, doi: 10.3389/fphy.2021.768165.
- [21] G. Agrawal and N. Dutta, *Semiconductor Lasers*, Second ed. KLUWER ACADEMIC PUBLISHERS BOSTON/DORDRECHT/LONDON, 2013.
- [22] G. Agrawal, *Fiber-Optic Communication Systems: Fourth Edition*. 2012.
- [23] T. Suhara, *Semiconductor Laser Fundamentals*. Marcel Dekker, 2004.
- [24] C. Henry, "Phase noise in semiconductor lasers," *J. Lightwave Technol.*, vol. 4, no. 3, pp. 298-311, 1986, doi: 10.1109/JLT.1986.1074721.
- [25] C. H. Henry, "Theory of the phase noise and power spectrum of a single mode injection laser," *IEEE Journal of Quantum Electronics*, vol. 19, pp. 1391-1397, 1983.
- [26] R. Paschotta, "Noise in Laser Technology," *Optik & Photonik*, vol. 4, no. 2, pp. 48-50, 2009, doi: <https://doi.org/10.1002/opph.201190028>.
- [27] A. E. Siegman, *Lasers*. Mill Valley, Calif.: University Science Books (in English), 1986.
- [28] K. Kikuchi, T. Okoshi, M. Nagamatsu, and N. Henmi, "Degradation of bit-error rate in coherent optical communications due to spectral spread of the transmitter and the local oscillator," *J. Lightwave Technol.*, vol. 2, no. 6, pp. 1024-1033, 1984, doi: 10.1109/JLT.1984.1073700.
- [29] A. v. d. Ziel, "Noise in solid-state devices and lasers," *Proceedings of the IEEE*, vol. 58, no. 8, pp. 1178-1206, 1970, doi: 10.1109/PROC.1970.7896.
- [30] R. Ramaswami, R. R. K. N. Sivarajan, K. Sivarajan, and E. I. Inc, *Optical Networks: A Practical Perspective*. Elsevier Science, 2002.
- [31] "Phase noise and frequency stability," in *Phase Noise and Frequency Stability in Oscillators*, E. Rubiola Ed., (The Cambridge RF and Microwave Engineering Series. Cambridge: Cambridge University Press, 2008, pp. 1-34.
- [32] D. Elyahu, D. Seidel, and L. Maleki, "RF Amplitude and Phase-Noise Reduction of an Optical Link and an Opto-Electronic Oscillator," *IEEE Transactions on Microwave Theory and Techniques*, vol. 56, no. 2, pp. 449-456, 2008, doi: 10.1109/TMTT.2007.914640.
- [33] M. Rodigheri, F. J. Galdieri, T. Sutili, and E. Conforti, "Optical Fiber Spool Acoustic Wave Resonances Employing a Mach-Zehnder Interferometer in Vacuum Chamber," *Journal of Microwaves, Optoelectronics and Electromagnetic Applications*, vol. 19, pp. 485-494, 2020. [Online]. Available: [http://www.scielo.br/scielo.php?script=sci\\_arttext&pid=S2179-10742020000400485&nrm=iso](http://www.scielo.br/scielo.php?script=sci_arttext&pid=S2179-10742020000400485&nrm=iso).

- [34] Z. Zhao *et al.*, "Narrow laser-linewidth measurement using short delay self-heterodyne interferometry," *Opt. Express*, vol. 30, no. 17, pp. 30600-30610, 2022/08/15 2022, doi: 10.1364/OE.455028.
- [35] M. Giraldo, *Measurement of the linewidth of a laser diode by using the delayed self-heterodyne technique*. 2016.
- [36] T. Sutili, "Aquisição Experimental Fotoelétrica Ultrarrápida com Algoritmos de Processamento Digital para a Análise de Subsistemas em Comunicações Ópticas Coerentes de Altíssimas Taxas," (in Portuguese), 2018.
- [37] Y. Li *et al.*, "Laser frequency noise measurement using an envelope-ratio method based on a delayed self-heterodyne interferometer," *Optics Communications*, vol. 435, pp. 244-250, 2019/03/15/ 2019, doi: <https://doi.org/10.1016/j.optcom.2018.10.065>.
- [38] L. B. Mercer, "1/f frequency noise effects on self-heterodyne linewidth measurements," *J. Lightwave Technol.*, vol. 9, no. 4, pp. 485-493, 1991, doi: 10.1109/50.76663.
- [39] K. Kikuchi, "Effect of 1/f-type FM noise on semiconductor-laser linewidth residual in high-power limit," *IEEE Journal of Quantum Electronics*, vol. 25, no. 4, pp. 684-688, 1989, doi: 10.1109/3.17331.
- [40] F. J. GALDIERI, "He-Ne broadening effect under acoustic wave over fiber optic Mach-Zehnder interferometer," PhD, Optical communication, Unicamp, 2013.
- [41] J. T. Verdeyen, *Laser electronics*. Englewood Cliffs, N.J.: Prentice Hall (in English), 1995.
- [42] A. Yariv, *Photonics : optical electronics in modern communications*. 6th ed. New York : Oxford University Press, 2007., 2007.
- [43] "Copyright," in *Fundamentals of Applied Probability and Random Processes (Second Edition)*, O. C. Ibe Ed. Boston: Academic Press, 2014, p. iv.
- [44] J. W. Goodman, *Statistical Optics*. John Wiley & Sons (in English), 2000.
- [45] "Noise in Laser Technology Part 1 : Intensity and Phase Noise."
- [46] J. Matukas *et al.*, "Optical and electrical characteristics of InGaAsP MQW BH DFB laser diodes," *Materials Science Forum*, vol. 384, p. 91, 01/01 2002, doi: 10.4028/[www.scientific.net/MSF.384-385.91](http://www.scientific.net/MSF.384-385.91).
- [47] S. A. Mahdi, "The power spectral density of 1/f noise in a tunable diode laser at different temperatures," *Journal of Optics*, vol. 47, no. 1, pp. 61-64, 2018/03/01 2018, doi: 10.1007/s12596-017-0426-x.
- [48] A. L. Schawlow and C. H. Townes, "Infrared and Optical Masers," *Physical Review*, vol. 112, no. 6, pp. 1940-1949, 12/15/ 1958, doi: 10.1103/PhysRev.112.1940.
- [49] K. Kikuchi and T. Okoshi, "Dependence of semiconductor laser linewidth on measurement time: evidence of predominance of 1/f noise," *Electronics Letters*, vol. 21, pp. 1011-1012, 1985.
- [50] K. Kikuchi, "Origin of residual semiconductor-laser linewidth in high-power limit," *Electronics Letters*, vol. 24, p. 1001, January 01, 1988 1988, doi: 10.1049/el:19880681.
- [51] S. Huang, T. Zhu, M. Liu, and W. Huang, "Precise measurement of ultra-narrow laser linewidths using the strong coherent envelope," *Scientific Reports*, vol. 7, no. 1, p. 41988, 2017/02/09 2017, doi: 10.1038/srep41988.
- [52] Y. Lai, H. Li, D. K. Kim, B. T. Diroll, C. B. Murray, and C. R. Kagan, "Low-Frequency (1/f) Noise in Nanocrystal Field-Effect Transistors," *ACS Nano*, vol. 8, no. 9, pp. 9664-9672, 2014/09/23 2014, doi: 10.1021/nn504303b.
- [53] D. Welford and A. Mooradian, "Output power and temperature dependence of the linewidth of single- frequency cw (GaAl)As diode lasers," *Applied Physics Letters*, vol. 40, p. 865, May 01, 1982 1982, doi: 10.1063/1.92945.

- [54] L. G. Kazovsky, "Impact of Laser Phase Noise on Optical Heterodyne Communication Systems," *Journal of Optical Communications*, vol. 7, no. 2, pp. 66-78, 1986, doi: doi:10.1515/JOC.1986.7.2.66.
- [55] F. N. Hooge, "The relation between 1/f noise and number of electrons," *Physica B: Condensed Matter*, vol. 162, no. 3, pp. 344-352, 1990/07/01/ 1990, doi: [https://doi.org/10.1016/0921-4526\(90\)90030-X](https://doi.org/10.1016/0921-4526(90)90030-X).
- [56] E. Conforti, "Optical Coherent Communication and Networking Perspectives."
- [57] A. A. Balandin, "Low-frequency 1/f noise in graphene devices," *Nature Nanotechnology*, vol. 8, no. 8, pp. 549-555, 2013/08/01 2013, doi: 10.1038/nnano.2013.144.
- [58] F. N. Hooge, "1/f Noise Sources," *IEEE Transactions on Electron Devices*, Article vol. 41, no. 11, pp. 1926-1935, 1994, doi: 10.1109/16.333808.
- [59] E. Paladino, Y. M. Galperin, G. Falci, and B. L. Altshuler, "1/f noise. Implications for solid-state quantum information," *Reviews of Modern Physics*, vol. 86, no. 2, pp. 361-418, 04/03/ 2014, doi: 10.1103/RevModPhys.86.361.
- [60] R. J. Fronen and L. K. J. Vandamme, "Low-frequency intensity noise in semiconductor lasers," *IEEE Journal of Quantum Electronics*, vol. 24, no. 5, pp. 724-736, 1988, doi: 10.1109/3.188.
- [61] R. J. Fronen, "Correlation between 1/f fluctuations in the two output beams of a laser diode," *IEEE Journal of Quantum Electronics*, vol. 27, no. 4, pp. 931-936, 1991, doi: 10.1109/3.83312.
- [62] A. Dandridge and H. F. Taylor, "Correlation of Low-Frequency Intensity and Frequency Fluctuations in GaAlAs Lasers," *IEEE Transactions on Microwave Theory and Techniques*, vol. 30, no. 10, pp. 1726-1738, 1982, doi: 10.1109/TMTT.1982.1131314.
- [63] A. Dandridge, R. Miles, and H. Taylor, "Polarization-resolved low-frequency noise in GaAlAs lasers," *J. Lightwave Technol.*, vol. 4, no. 9, pp. 1311-1316, 1986, doi: 10.1109/JLT.1986.1074890.
- [64] Z. Celik-Butler and T. Y. Hsiang, "Determination of Si-SiO<sub>2</sub>/sub 2/ interface trap density by 1/f noise measurements," *IEEE Transactions on Electron Devices*, vol. 35, no. 10, pp. 1651-1655, 1988, doi: 10.1109/16.7368.
- [65] D. M. Fleetwood and J. H. Scofield, "Evidence that similar point defects cause 1/f noise and radiation-induced-hole trapping in metal-oxide-semiconductor transistors," *Physical Review Letters*, vol. 64, no. 5, pp. 579-582, 01/29/ 1990, doi: 10.1103/PhysRevLett.64.579.
- [66] F. GrÜneis, "1/f NOISE DUE TO ATOMIC DIFFUSION OF IMPURITY CENTERS IN SEMICONDUCTORS," *Fluctuation and Noise Letters*, vol. 01, no. 04, pp. L197-L220, 2001/12/01 2001, doi: 10.1142/S0219477501000433.
- [67] R. J. Fronen and F. N. Hooge, "1/f noise in a p-i-n diode and in a diode laser below threshold," *Solid-State Electronics*, vol. 34, no. 9, pp. 977-982, 1991/09/01/ 1991, doi: [https://doi.org/10.1016/0038-1101\(91\)90216-L](https://doi.org/10.1016/0038-1101(91)90216-L).
- [68] M. Fukuda, T. Hirono, T. Kurosaki, and F. Kano, "Correlation between 1/f noise and semiconductor laser degradation," *Quality and Reliability Engineering International*, <https://doi.org/10.1002/qre.4680100416> vol. 10, no. 4, pp. 351-353, 1994/01/01 1994, doi: <https://doi.org/10.1002/qre.4680100416>.
- [69] M. Fukuda, T. Hirono, T. Kurosaki, and F. Kano, "1/f noise behavior in semiconductor laser degradation," *IEEE Photonics Technology Letters*, vol. 5, no. 10, pp. 1165-1167, 1993, doi: 10.1109/68.248415.
- [70] M. Fukuda and G. Iwane, "Degradation of active region in InGaAsP/InP buried heterostructure lasers," *Journal of Applied Physics*, vol. 58, no. 8, pp. 2932-2936, 1985/10/15 1985, doi: 10.1063/1.336298.

- [71] M. Fukuda and G. Iwane, "Correlation between degradation and device characteristic changes in InGaAsP/InP buried heterostructure lasers," *Journal of Applied Physics*, vol. 59, no. 4, pp. 1031-1037, 1986/02/15 1986, doi: 10.1063/1.336537.
- [72] O. Llopis, S. Azaizia, K. Saleh, A. A. Slimane, and A. Fernandez, "Photodiode 1/f noise and other types of less known baseband noises in optical telecommunications devices," in *2013 22nd International Conference on Noise and Fluctuations (ICNF)*, 24-28 June 2013 2013, pp. 1-4, doi: 10.1109/ICNF.2013.6579014.
- [73] S. Pralgauskaitė *et al.*, "Reliability investigation of light-emitting diodes via low frequency noise characteristics," *Microelectronics Reliability*, vol. 55, no. 1, pp. 52-61, 2015/01/01/ 2015, doi: <https://doi.org/10.1016/j.microrel.2014.09.027>.
- [74] L. Z. Hasse, S. Babicz, L. Kaczmarek, J. M. Smulko, and V. Sedlakova, "Quality assessment of ZnO-based varistors by 1/f noise," *Microelectronics Reliability*, vol. 54, no. 1, pp. 192-199, 2014/01/01/ 2014, doi: <https://doi.org/10.1016/j.microrel.2013.09.007>.
- [75] H. Zhu, K. Liu, C. Xiong, S. Feng, and C. Guo, "The effect of external stress on the properties of AlGaAs/GaAs single quantum well laser diodes," *Microelectronics Reliability*, vol. 55, no. 1, pp. 62-65, 2015/01/01/ 2015, doi: <https://doi.org/10.1016/j.microrel.2014.09.012>.
- [76] M. Fukuda, F. Kano, T. Kurosaki, and J. Yoshida, "Reliability and degradation behavior of highly coherent 1.55  $\mu$ m long-cavity multiple quantum well (MQW) DFB lasers," *J. Lightwave Technol.*, vol. 10, no. 8, pp. 1097-1104, 1992, doi: 10.1109/50.156850.
- [77] J. Miles, "<http://www.ke5fx.com/>."

# 7 Appendix

Table 7-1 Specifications of Electrical Spectrum Analyzer HP3561A (ESA)

<b>Frequency:</b>		
<b>Range:</b> 0.000125 Hz to 100 kHz.	<b>Spans:</b> 0.01024 Hz to 100 kHz in a 1, 2, 2.5, 5, 10 sequence. Other spans are available.	<b>Accuracy:</b> ± 0.003% of display center frequency.
<b>Resolution:</b> 0.25% of frequency span.	<b>Real-time bandwidth:</b> (typical) single display, 3 kHz. Fast average display, 7.5 kHz.	
<b>Bandwidth</b> (3 dB Bandwidth (% of frequency span)): Flat: 0.90%, Hann: 0.36%, Uniform: 0.22%	<b>Window:</b> flat top, hann, uniform, and exponential	
<b>Amplitude</b>		
<b>Measurement range:</b> + 27 to -120 dBV noise floor (22.4 VRMS to 1µV noise floor). Input range selected in 1 -dB steps from +27 to -51 dBV. Optimum range determined automatically in autorange mode.		
<b>Accuracy at the passband center:</b> ±0.15 dB +27 to -40 dBV input ranges ±0.25 dB -41 to -51 dBV input ranges	<b>Flat top window:</b> +0, -0.01 dB <b>Hann window:</b> +0, -1.5 dB <b>Uniform window:</b> +10, -4.0 dB	
Note: overall accuracy is the sum of the accuracy at the passband center plus the selected window accuracy		
<b>Dynamic range:</b> 80 dB	<b>Resolution:</b> Log: 0.01 dB, Linear: 4 digits	
<b>Phase</b>		
<b>Accuracy:</b> ±2 degrees, dc-10 kHz; ± 10 degrees, 10- 100 kHz (signals no more than 40 dB below full range).	<b>Resolution:</b> 0.1 degree	
<b>Input</b>		
<b>Impedance:</b> $1 \times 10^6 \Omega \pm 5\%$ shunted by 95 pF maximum		
<b>Isolation:</b> input low may be connected to chassis ground or floated up to 30 volts rms (42 volts peak) above ground		
<b>Coupling:</b> signal may be ac or dc coupled. Low frequency 3-dB point < 1 Hz in ac mode.		
<b>A-weighting:</b> hardware A-weighting filter conforms to ANSI standard S 1.4-1971 (R 1 976)		
<b>ICP current:</b> nominal 4 mA current source provided, compatible with integrated circuit piezoelectric accelerometers		
<b>Output</b>		
<b>Source:</b> band-limited, band-translated, pseudo-random, random, or impulse, or TTL "synch" signals are available on rear panel. Level is selectable between 0.7 and 0.007 volts rms, nominal. Impedance $50 \Omega \pm 5 \Omega$		



Figure 7-1 Agilent HP 3561A Dynamic Signal Analyzer



Figure 7-2 RIO PLANEX™ Series 1550nm Low Phase Noise Narrow Linewidth External Cavity Laser

Table 7-2 key features and applications of RIO PLANEX™ Series

<b>Properties</b>		
Single longitudinal mode	Very low Relative intensity noise (RIN) [ $\text{Hz}^{-1}$ ] or [ $\text{dBc}/\text{Hz}$ ]	Small form factor, 14 pin butterfly
Center wavelength: 1530nm-1565nm	Excellent Minimum Side Mode Suppression Ratio (SMSR) [ $\text{dBm}$ ]	Low power dissipation
Narrow linewidth, long coherence length	Excellent wavelength stability over life and temperature	SMF and PM fiber pigtail options
Low phase noise	Low sensitivity to vibration and acoustic noise	Telecordia GR-468 qualified platform
Wavelength tunability	CW, modulated and pulsed operations	RoHS compliant
<b>Applications</b>		
Seeding of fiber and solid-state lasers	Optical Parametric Oscillators (OPOs)	Laser Spectroscopy
Second Harmonic Generation (SHG)	LIDAR	Metrology

Table 7-3 Optical and Electrical Specifications of RIO PLANEX™ Series

Parameter	Symbol	Conditions	Min	Typ	Max	Unit
TEC set Temperature	$T_{set}$	Specified for every laser	15		50	°C
Output Power <sup>1</sup>	$P_{out}$	CW	see ordering information page			mW
Threshold current	$I_{th}$	@ $T_{set}$		10	15	mA
Laser Bias Current	$I_b$	CW, $P_{out}$		120	200	mA
Laser Forward Voltage	$V_f$	CW, @ 100mA		1.6	2	V
Center Wavelength (ITU grid)	$\lambda$	$\pm 40$ pm standard <sup>2</sup>	1530		1565	nm
Side Mode Suppression Ratio	SMSR	CW, at specified $P_{out}$	40			dB
Wavelength vs. TEC Temperature	$d\lambda/dT$	$T_{set} \pm 2^\circ\text{C}$		12		pm/°C
Wavelength tunability	$\Delta\lambda_T$	via TEC temperature change	30 <sup>4</sup>			pm
Relative Intensity Noise	RIN	> 1kHz			-140	dB/Hz
		> 500 kHz	Shot noise limited			
Polarization Extinction Ratio	PER	For PM option, polarization and connector key aligned to slow axis	20			dB
Monitor bias voltage	$V_R$	Cathode positive to anode	4.75	5	5.25	V
Monitor diode current	$I_{mc}$	$P_{out}$	0.05		1	mA
Monitor diode dark current	$I_{md}$	$V_R = 5V$			5	nA
Modulation bandwidth			1			GHz
Input Impedance	$Z_0$			25		Ohm
Optical Isolation	ISO		40			dB

Table 7-4 Linewidth and Phase Noise Specifications of RIO PLANEX™ Series

Parameter	Symbol	Conditions	Grade 1	Grade 3	Grade 4	Unit
Spectral Linewidth, FWHM <sup>1</sup>	$\Delta\lambda_L$		<15	<5	<2	kHz
Phase Noise Typical Values <sup>2</sup>	PhN	@ 10 Hz	123	41	20	$\mu\text{rad}/\text{rt-Hz}$ 1 m OPD
		@ 200 Hz	22	8	4	

## 7.1 Software

The 7470.EXE [77] software is a Win32-based emulator. It acquires an HP-GL/2 plot and renders it in a window. The plot can then be printed, viewed as an overlay with other plots, or saved in several different graphics file formats as well as its original HP-GL/2 format. With the help of this software, it is possible to capture screenshots from GPIB-based test equipment such as digital oscilloscopes, spectrum analyzers, logic analyzers, and more. The 7470.EXE can even recognize certain instrument models and request plots from them without user access to their front-panel controls. The 7470.EXE emulator requires a two-way GPIB conversation

with the instrument. Therefore, it is necessary to configure the instrument for Talk/Listen mode (as opposed to Talk-Only or System Controller mode). This software has some advantages such as 1- Compatible with a wide range of instruments. 2- Easy to use. 3- Open-source code that makes it possible to change some functionality within the software. The software source code is able to be compile with *Microsoft Visual Studio Express package* 4- Adding a caption to the graph. 5- changing the resolution and the color of the plot.

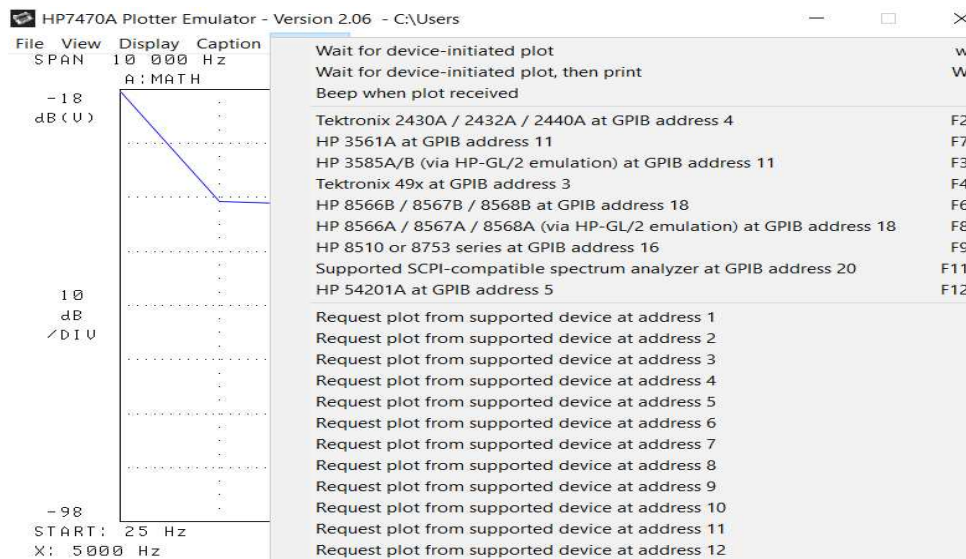


Figure 7-3 The 7470.EXE software

## 7.2 Designing the graphs with Corel Draw

As mentioned previously, the computer acquired the data (graphs) from the Electrical Spectrum Analyzer via the USB/GPIB interface (Agilent Technologies: 82357B) by using the software (HP7470A plotter emulator). To create each graph with its corresponding output power, five measurements with different spans (10 Hz, 100 Hz, 1 kHz, 10 kHz, 100kHz) were taken. Then apart from the beginning, just the latest span decade of each curve is used to draw the graphs, therefore every graph is the combination of the last part of each curve. For example, for the curve that goes up to 100 kHz, only 10 kHz to 100 kHz is used and for the curve that goes up to 10 kHz, the part from 1 kHz to 10 kHz, and so on. Until for the curve that goes up to 10 Hz, the whole curve is used. Then, using Corel Draw program, all pieces of the curves are combined to form a single graph, but it needs to adjust the amplitudes in order the final

curve does not have discontinuity. However, because of the instrument and the polarization adjustment difficulty, there are minor differences in power.

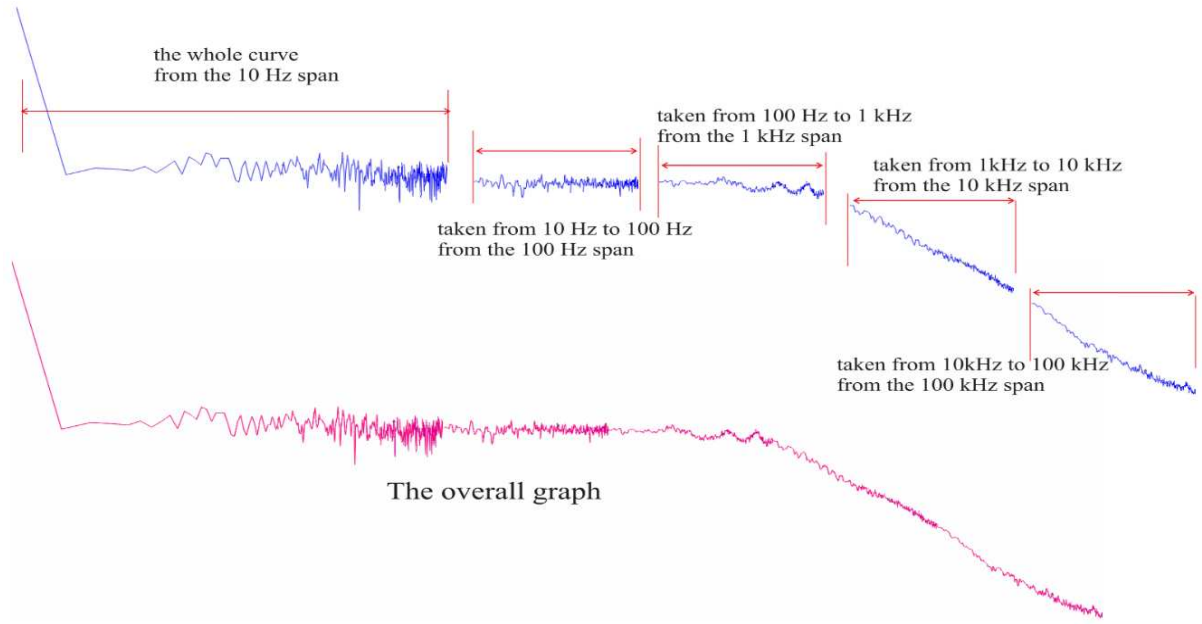


Figure 7-4 Five measurements with varying spans were used to construct each graph with its associated output power (10 Hz, 100 Hz, 1 kHz, 10 kHz, 100kHz), The graph below is the overall graph from the above